



Delft University of Technology

Modelling and Monitoring of Dynamic Wheel-Rail Interaction at Railway Crossing

Wei, Zilong

DOI

[10.4233/uuid:2da90b9e-794e-45ac-ae72-0b532e058983](https://doi.org/10.4233/uuid:2da90b9e-794e-45ac-ae72-0b532e058983)

Publication date

2018

Document Version

Final published version

Citation (APA)

Wei, Z. (2018). *Modelling and Monitoring of Dynamic Wheel-Rail Interaction at Railway Crossing*. [Dissertation (TU Delft), Delft University of Technology]. <https://doi.org/10.4233/uuid:2da90b9e-794e-45ac-ae72-0b532e058983>

Important note

To cite this publication, please use the final published version (if applicable).
Please check the document version above.

Copyright

Other than for strictly personal use, it is not permitted to download, forward or distribute the text or part of it, without the consent of the author(s) and/or copyright holder(s), unless the work is under an open content license such as Creative Commons.

Takedown policy

Please contact us and provide details if you believe this document breaches copyrights.
We will remove access to the work immediately and investigate your claim.



Modelling and Monitoring of Dynamic Wheel-Rail Interaction at Railway Crossing

Zilong Wei

Modelling and Monitoring of Dynamic Wheel-Rail Interaction at Railway Crossing

Zilong WEI

Modelling and Monitoring of Dynamic Wheel-Rail Interaction at Railway Crossing

Dissertation

for the purpose of obtaining the degree of doctor
at Delft University of Technology
by the authority of the Rector Magnificus prof.dr.ir. T.H.J.J. van der Hagen
chair of the Board for Doctorates
to be defended publicly on
Tuesday 22 May 2018 at 10:00 o'clock

by

Zilong WEI

Master of Engineering in Highway and Railway Engineering,
Tongji University, Shanghai, China
Born in Laiwu, Shandong, China

This dissertation has been approved by the promotores.

Composition of the doctoral committee:

Rector Magnificus,	Chairperson
Prof.dr.ir. R.P.B.J. Dollevoet	Delft University of Technology, promotor
Prof.dr.ir. Z. Li	Delft University of Technology, promotor

Independent members:

Prof.dr.ir. E. van der Heide	University of Twente
Prof.dr. A. Metrikine	Delft University of Technology
Prof.dr. J. Nielsen	Chalmers University of Technology, Sweden
Prof.dr.ir. J. Sietsma	Delft University of Technology
Ir. T. Sysling	ProRail

This dissertation was financially supported by:



ISBN: 978-94-6366-035-8

Printed by: Gildeprint – Enschede

Copyright © 2018 by Zilong Wei (weizilongchina@gmail.com)

An electronic copy of this dissertation is available at <http://repository.tudelft.nl/>

To my family
献给我的家人

SUMMARY

Crossings are track components that provide flexibility for railway operation. To facilitate the intersection of different tracks at the same level, an inherent geometric discontinuity is designed in crossings, inducing aggressive wheel-rail impact force during the passage of vehicles. Therefore, crossings degrade much faster than plain tracks and account for a large portion of the maintenance cost. The situation becomes worse with the increasing demands for higher speed, larger capacity and longer service time in recent years.

This dissertation aims to gain a better understanding of the dynamic wheel-rail interaction at crossings, including characterizing the wheel-rail contact behaviour, evaluating the performance of crossings under traffic loads and monitoring the health condition of the structure. The gained knowledge is expected to improve the design, maintenance and inspection strategies, and further to minimize the maintenance cost and guarantee the reliability of the track infrastructure.

The first part of this dissertation focuses on an in-depth analysis of wheel-rail contact behavior and related rail degradation. An explicit 3D finite element (FE) model is developed to simulate the passage of a wheelset across a nominal crossing. The simulated dynamic responses in terms of the major frequencies and energy distributions of axle box acceleration (ABA) are verified with in-situ ABA measurements. The evolution of wheel-rail contact parameters (i.e., contact force, contact position, contact patch, adhesion-slip state, pressure, shear traction and micro-slip) is elaborated during the passage of a wheelset. These contact parameters are then used to predict the rail degradation due to plastic deformation and wear. The analysis indicates that the variations of the normal and tangential contact forces are out-of-sync during the wheel-rail impact. The maxima of plastic deformation and wear of the crossing nose occur in the two-point contact stage rather than, as widely believed, at the moment with the maximum normal contact force. These findings could contribute to the investigation of non-proportional loading in the materials and lead to a deeper insight of the damage mechanisms. Eventually, these findings could improve the structure and material design of crossings.

The second part proposes a method to evaluate the performance of long-term serviced crossings. In the method, in-situ 3D profile and hardness measurements are conducted on a long-term serviced crossing and are used as the input for the FE modeling of dynamic wheel-rail interaction. The simulated wheel-rail contact parameters are then used to predict the distributions of plastic deformation and wear. By comparing the numerical results obtained on nominal and long-term serviced crossings, the performance of the long-term serviced crossing can be assessed. The capability of the method is demonstrated via a case study conducted on the Dutch railway. The case study indicates that the wheel-rail interaction on the long-term serviced crossing significantly depends on the train moving direction. In the direction with major traffic loads, the long-term serviced crossing experienced a run-in process, manifested as the widening of running band, an enlargement of contact patch size and a decrease of

contact stresses. Eventually, both plastic deformation and wear decrease at the crossing. In the direction with minor traffics, however, the wheel-rail interaction exacerbates, coming with a narrower running band, smaller contact patch size, higher contact stresses and thus larger magnitudes of plastic deformation and wear. This information can serve as a guidance on preventive maintenance and structure design.

The third part analyses the characteristic dynamic response of wheel-rail interaction at crossings. For this purpose, in-situ ABA measurements were conducted on a nominal crossing with various test parameters, including train speed, train moving direction and sensor position. Thereafter, a roving-accelerometer hammer test was carried out to extract the relationship between the signature tune of the ABA and the natural frequencies of the crossing. The experimental results indicate that the major frequency bands of the vertical ABA are related to the natural frequencies of the crossing; thus, these frequency bands are not greatly affected by variations in train speed, moving direction and sensor position. The vibration energy concentrated at the major frequency bands of the vertical ABA increases with higher train speeds, along facing moving direction and from the leading wheel. Vibrations of crossing rails at the major frequency bands of the vertical ABA are a combination of bending and torsion rather than solely bending, as the vibrations of wing rails are not synchronized. The gained information is useful for developing the ABA system for monitoring the health condition of crossings.

The fourth part investigates the feasibility of the ABA system for monitoring the health condition of crossings. At crossings, the implementation of the ABA system is more complicated than on plain tracks because of the complex structure and discontinued geometry. The measured ABA contains dynamic response caused by both the designed geometric discontinuity and the undesirable degradation, so that the ABA system must be able to distinguish between the different sources. To overcome the challenge, information from multiple sensors, namely, ABA signals, 3D rail profiles, GPS and tachometer recordings, was collected from both nominal and degraded crossings. By proper correlation of the gathered data, an algorithm was proposed to identify the characteristic ABA related to crossing degradation and then to evaluate the health condition of the structure. The algorithm was then demonstrated with a crossing with a degradation status unknown beforehand. The results indicate that the ABA system is capable of monitoring two types of degradation. The first type is the uneven deformation between wing rail and crossing nose; the second is a local irregularity in the longitudinal slope of crossing nose. The type and severity of the degradation can be evaluated by the spatial distribution and energy concentration of the characteristic frequency bands of the ABA.

The gained knowledge contributes to a better understanding of the dynamic wheel-rail interaction at crossings. Meanwhile, the proposed experimental and numerical approaches provide reliable tools for evaluating the performance and monitoring the health condition of crossings.

SAMENVATTING

In een spoornetwerk zorgen wissels voor flexibiliteit in de dienstregeling. Om de wielflens te laten passeren bij een gelijkvloerse spoorkruising, is er een onderbreking van de spoorstaaf nodig, zoals bij alle vaste kruis- en punt-stukken. Deze onderbreking zorgt voor hoge wiel-rail interactie krachten tijdens een trein passage, wat leidt tot snellere degradatie in vergelijking met gewoon spoor. Daarnaast neemt de intensiteit en snelheid van het treinverkeer toe, waardoor er meer tijd nodig is voor onderhoud, maar minder tijd beschikbaar.

Het doel van deze dissertatie is om meer inzicht te krijgen in de dynamische interactie tussen de trein en het wissel. Hiervoor wordt niet alleen gekeken naar het wiel-rail contact, maar ook naar prestaties van het wissel en het monitoren van de conditie. Deze kennis kan worden ingezet om de ontwerp, onderhoud en inspectie strategieën te optimaliseren. Hierdoor kunnen de kosten omlaag en gaat de betrouwbaarheid en beschikbaarheid van het spoornetwerk omhoog.

Het eerste deel van deze dissertatie zoomt in op het wiel-rail contact en de bijbehorende slijtage. Een driedimensionaal eindige elementen model is ontwikkeld om de passage van een wielstel door een wissel te simuleren. Van deze simulaties is de frequentie inhoud van de aspotversnellingen gevalideerd met veldmetingen. Het verloop van de contact parameters (zoals contact kracht, locatie, contact vlak, adhesie-slip, druk, tractie en micro-slip) zijn verder uitgewerkt. Op basis van deze parameters is een voorspelling gedaan voor de verwachte degeneratie als gevolg van plastische vervorming en slijtage. Op basis van deze analyse kan worden geconcludeerd dat het verloop van de normaal kracht en de tangentaal kracht niet synchroon is als het treinwiel op de naald van het puntstuk landt. De grootste plastische vervorming en slijtage van de naald treden op tijdens het twee-punts contact en niet, in tegenstelling tot wat werd aangenomen, tijdens het moment waarop de contact kracht het grootst is. Deze inzichten zijn cruciaal om de belasting van het materiaal beter te onderzoeken en om meer inzicht te krijgen in de faalmechanismen. Hierdoor is het mogelijk om het wissel ontwerp verder te optimaliseren.

In het tweede deel van deze dissertatie wordt een methode gepresenteerd om de prestaties van puntstukken over langere tijd te evalueren. Voor deze methode zijn het 3D profiel en de hardheid van het wissel met een lange staat van dienst gemeten en deze data is gecombineerd met het eindige elementen model. De resultaten van het gesimuleerde wiel-rail contact worden opnieuw gebruikt om de plastische vervorming en slijtage te voorspellen. Door de resultaten van de simulatie van een nieuw puntstuk te vergelijken met resultaten van een gebruikt puntstuk, kunnen de prestaties op langere termijn worden bepaald. De mogelijkheden van deze methode worden gedemonstreerd aan de hand van een casus in het Nederlandse spoornetwerk. Deze casus laat zien dat de wiel-rail interactie op de langere termijn sterk afhankelijk is van de meest voorkomende berijding. In deze richting wordt een inloop proces waargenomen, waarbij het loopvlak breder, het contactvlak groter en spanningen in het contactvlak afnemen. Dit leidt tot een afname van de plastische vervorming en slijtage. In de rijrichting met een lage

berijding wordt juist het tegenovergestelde waargenomen. Het loopvlak wordt smaller en het contactvlak kleiner, wat leidt tot hogere contact spanningen en dus meer plastische vervorming en slijtage. Deze kennis kan nuttig worden gebruikt bij het plannen van preventief onderhoud.

In het derde deel worden de karakteristieke dynamische eigenschappen van het wiel-rail contact in wissels geanalyseerd. Hiervoor zijn de aspotversnellingen gemeten van een treinpassage over een nieuw puntstuk, waarbij verschillende parameters zijn gevarieerd, zoals de rijrichting, treinsnelheid en sensor locatie. Ook is er een impact test gedaan met een geïnstrumenteerde meethamer. Op basis van beide metingen zijn de karakteristieke frequenties van de aspotversnellingen vergeleken met de eigenfrequenties van het puntstuk. Hieruit is geconcludeerd dat er een verband is tussen de karakteristieke frequenties van de aspotversnellingen in verticale richting en de eigenfrequenties van het puntstuk. Hiermee kan worden aangetoond dat de frequentie inhoud van de aspotversnellingen maar minimaal beïnvloed wordt door externe parameters, zoals de rijrichting en snelheid van de trein en de sensor locatie. De energie voor deze frequenties neemt wel toe als de snelheid van de trein toeneemt. Verder blijkt dat deze trillingen een combinatie is van buiging en rotatie, in plaats van puur buiging, omdat de trillingen van beide vleugelspoortstaven niet synchroon zijn. Deze conclusies zijn erg waardevol voor het door ontwikkelen van een conditie monitoring systeem voor puntstukken op basis van aspotversnellingen.

Een haalbaarheidsstudie voor het gebruik van aspotversnellingen als conditie monitoring in wissels is gedaan in het vierde deel van deze dissertatie. De implementatie van een dergelijk systeem is veel complexer dan voor vrije baan, vanwege de constructie en discontinuïteit in wissels. Het gemeten signaal bevat hierdoor zowel de trillingen die horen bij een normaal puntstuk, als trillingen die horen bij degeneratie. Om bruikbare resultaten te genereren, moet oorzaak van de trillingen bepaald kunnen worden. Hiervoor zijn verschillende metingen gedaan op zowel nieuwe als gebruikte puntstukken, waaronder aspotversnellingen, 3D dwarsdoorsneden en GPS en ODO meter voor de positionering. Door deze data te correleren is een algoritme ontworpen waarmee de degradatie op basis van aspotversnellingen kan worden bepaald. Dit algoritme is getoetst aan de hand van een puntstuk waarvan de degradatie op voorhand niet bekend was. Hieruit bleek dat dit algoritme in staat is om twee soorten slijtage te monitoren; ongelijke slijtage van de vleugel ten opzichte van de naald en kopdefecten in het naald. Het type en de ernst van het defect kan worden afgeleid uit locatie en de intensiteit van de karakteristieke frequenties in het meetsignaal.

Deze conclusies dragen bij aan een beter begrip van de wiel-rail interactie in wissels. Daarnaast bieden de voorgestelde numerieke en experimentele technieken een solide basis om de prestaties en conditie van puntstukken te evalueren.

CONTENTS

Summary	vii
Samenvatting	ix
1 Introduction	1
1.1 Overview of railway turnout.....	2
1.2 Crossing degradation and consequences.....	2
1.3 Dynamics of vehicle-track system	3
1.3.1 Vehicle dynamics.....	4
1.3.2 Track dynamics.....	5
1.3.3 Frictional wheel-rail contact.....	6
1.3.4 Wheel-rail interaction at crossing.....	7
1.4 Prediction of rail degradation.....	8
1.5 Detection of rail degradation	9
1.6 Problem statement	10
1.7 Outline of this dissertation.....	11
References.....	12
2 Modelling and verification of wheel-rail impact at crossing	21
2.1 Introduction.....	22
2.2 Modelling of wheel-rail interaction at crossing.....	23
2.2.1 Wheelset and crossing panel	24
2.2.2 Motion of wheelset	25
2.2.3 Simulation procedure.....	25
2.3 Verification of the simulated dynamic response.....	26
2.4 Evolution of frictional wheel-rail contact.....	28
2.4.1 Contact force	28
2.4.2 Contact position.....	29
2.4.3 Contact stresses	30
2.4.4 Micro-slip.....	33
2.5 Crossing degradation due to the impact	34
2.5.1 Plastic deformation	34

2.5.2 Frictional work.....	35
2.6 Discussion.....	36
2.7 Summary	37
References.....	37
3 Evaluating the performance of long-time serviced crossing rails	41
3.1 Introduction.....	42
3.2 Evaluation procedure	44
3.2.1 In-situ measurements	44
3.2.2 FE modelling of wheel-rail interaction.....	44
3.2.3 Prediction of rail degradation	46
3.3 Case study	47
3.3.1 STEP 1: Measuring the degradation status.....	47
3.3.2 STEP 2: Characterizing wheel/rail contact behavior	50
3.3.3 STEP 3: Performance evaluation.....	54
3.4 Discussion.....	57
3.4.1 Comparison of numerical results with measurements	57
3.4.2 Criteria for guiding preventive maintenance.....	57
3.4.3 Extending the capabiligy of the proposed method	59
3.5 Summary	59
References.....	59
4 Identifying the characteristics of ABA at crossing	63
4.1 Introduction.....	64
4.2 In-situ ABA measurements and hammer test.....	66
4.2.1 ABA measurement system	66
4.2.2 Setup of hammer test	68
4.3 ABA signals at various test conditions.....	70
4.3.1 Train speed	70
4.3.2 Train moving direction.....	72
4.3.3 Sensor position.....	74
4.3.4 Characteristics of longitudinal ABA	75
4.4 Relationship between ABA and crossing natural response.....	77
4.5 Summary	81
References.....	81
5 Evaluating crossing degradation using ABA measurement	85
5.1 Introduction.....	86

5.2 ABA and 3D profile measurements	88
5.2.1 ABA measurement.....	89
5.2.2 3D profile measurement.....	91
5.3 Characteristics of ABA related to measured crossing degradation	93
5.3.1 Repeatability of measured ABA.....	93
5.3.2 Comparion of ABA between nominal and degraded crossings.....	94
5.3.3 Detection algorithm for measured crossing degradation	95
5.4 Case study: Trial detection and verification.....	96
5.4.1 Track site	96
5.4.2 Trial evaluation.....	97
5.4.3 Verification.....	97
5.5 Discussion: Extending ABA system to other examples.....	98
5.6 Summary	99
References.....	100
6 Conclusions and recommendations	103
6.1 Conclusions	104
6.2 Recommendations	107
References.....	108
A Frictional Contact of Compression–Shift–Rolling Evolution	109
A.1 Introduction.....	110
A.2 Demonstration of the FE model	111
A.3 Validation of the FE model	118
A.3.1 Spence compression	118
A.3.2 Compression to Cattaneo shift.....	120
A.3.3 Cattaneo shift to stationary rolling	121
A.4 Discussion.....	123
A.5 Summary	123
References.....	124
Acknowledgement	127
Curriculum Vitae	129

1

INTRODUCTION

1.1 OVERVIEW OF RAILWAY TURNOUT

Turnouts are the fundamental components of the railway track. Figure 1.1 shows a schematic diagram of turnouts. Apart from the conventional functions of ordinary rails such as 1) sustaining the wheel loads, 2) transferring the loads to other track components and 3) guiding the moving direction of wheels, a turnout can provide flexibility for railway operation by intersecting different tracks at the same level [1]. Therefore, vehicles can run over the turnout along either the straight line (i.e., through direction) or the curve (i.e., divergent direction).

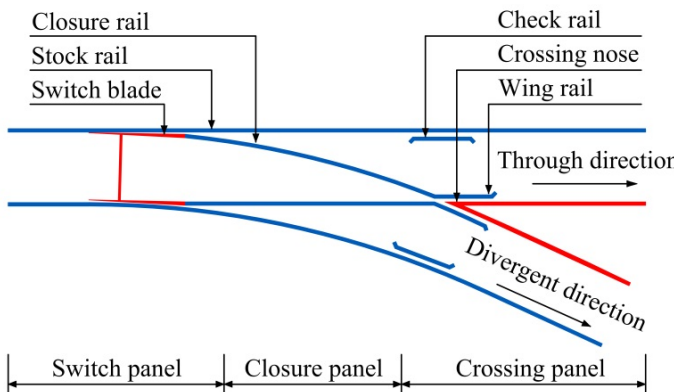


Figure 1.1: Schematic diagram of a turnout

A turnout composes of two major parts, i.e., a switch (Figure 1.2(a)) and a crossing (Figure 1.2(b)). These two parts are connected by closure rails. The functions of the switch and the crossing are as follows [1]:

- A switch consists of switch blades and stock rails. The switch blades can move with the aid of a point machine, so that the moving direction of vehicles can be determined;
- A crossing consists of check rails, wing rails and a crossing nose. Vehicles can pass from one track to another while remaining supported. A geometric discontinuity is made by design between the closure rail and crossing nose, so that the clearance of wheel flange is guaranteed.

1.2 CROSSING DEGRADATION AND CONSEQUENCES

During the passage of vehicles over crossings, the intrinsic geometric discontinuity between closure rail and crossing nose raises the dynamic wheel-rail contact forces, speeding up the degradation of crossing rails. As a consequence, crossings contribute to a large portion of the maintenance and renewal costs of the track infrastructure worldwide. For example, faults of switches and crossings in Sweden generate over 13% of the maintenance cost [2]. In the Netherlands, a total number of 826 crossings in the network were replaced between 2011 and 2015 [3]. Moreover, it is stipulated by the railway infrastructure managers that severely degraded crossings must be replaced urgently (e.g., within 24 hours in the Netherlands) after they are detected, inducing unpredictable traffic disruptions of the railway transport.

Figure 1.3 shows examples of defects at crossings. The crossing in Figure 1.3(a) was replaced urgently owing to two severe cracks, one lying along the top of the crossing nose while the other around the gauge corner. In Figures 1.3(b) and 1.3(c), squats took place on the crossing nose and the wing rail, and cracks propagated into the surface in Figure 1.3(c). The crossing nose in Figure 1.3(d) deteriorated due to shelling. Since the dynamic vehicle-track interaction exacerbates on degraded crossing rails, the contact forces and stresses may raise significantly compared to the nominal condition, which increases the risk of sudden failure of crossing rails and endangers the safety of train operation. Besides, due to the current incapability of train-borne grinding machine at crossings, maintenance actions (e.g., grinding and welding) are conducted manually on crossings, so that the repaired profiles may differ from one technician to another and case by case. Therefore, the maintenance works may not always be beneficial to extend the service life of degraded crossings.



(a) Switch



(b) Crossing

Figure 1.2: Major components of a turnout

As high dynamic loads transmit from crossing rails to other track components (such as fastening, sleeper, ballast and subgrade), the latter also suffer from fast degradation. In the fastening system, bolts become loose or missing (Figure 1.3(e)), and railpads become damaged or displaced. Under high dynamic wheel loads, ballast and subgrade experience uneven settlement, and sleepers move or deteriorate (Figure 1.3(f)). The degradation of these track components will in turn exacerbate the dynamic vehicle-track interaction.

The passage of vehicles over crossings also induces undesired vibration and noise, which have significant influence on both passengers inside the cabins and residents living nearby the railway tracks [4]. The severity of vibration and noise become worsened with the presence of crossing degradation.

1.3 DYNAMICS OF VEHICLE-TRACK SYSTEM

The dynamic behaviour of the vehicle-track system is determined by three constituents, i.e., the vehicle subsystem, the track subsystem and the interaction between them. Generally, it is a tough task to analyse the dynamics of such a complex system as a complete structure. For crossings, the task becomes more complicated than plain tracks because of the complex structure and discontinued geometry. Therefore, the dynamics of the preceding three constituents will be analysed separately.

1



(a) Cracks



(b) Squats on crossing nose



(c) Squats on wing rail



(d) Shelling



(e) Missing bolt



(f) Indentation of baseplate into sleeper

Figure 1.3: Defects at crossings

1.3.1 VEHICLE DYNAMICS

The vehicle subsystem composes of a carbody, bogies, wheelsets, suspensions and so on [5]. Carbody and bogie frame are connected by the second suspension, while bearings of wheelsets and bogie frames are connected by the primary suspension. The suspensions are essential for the stability and ride quality (i.e., the ability of vehicles to run along an ideal trajectory without generating disturbances that may affect the comfort of passengers) of vehicles.

Human is very sensitive to the vertical vibrations at 4-10 Hz [6-8]. To maintain the passenger comfort, the dominant natural frequencies of the carbody must not overlap with this sensitive frequency range [9, 10]. In the range of 10-50 Hz, the dynamic behaviour of the bogie frame becomes increasingly isolated from the wheelset [11, 12]. In the mid- and high-frequency ranges above 50 Hz, the flexibility of the bogie frame becomes less relevant to the dynamic response of the wheel-rail interaction. Therefore, the simplification of carbody and bogie frame as sprung mass is often adequate when the mid- and high- frequency response of the vehicle-track system is focused on [13].

To analyse the vehicle dynamics in the mid- or high- frequency range, the simplification of wheelset as lumped mass or rigid body becomes insufficient. Instead, the flexibility of the wheelset should be taken into account [14-16]. To represent the flexibility of wheelset, several methods were proposed, as reviewed in [17]. These methods can be classified as the following categories:

- Splitting the wheelset into a certain number of rigid or lumped bodies connected by springs and dampers [18-22]. The method is able to describe the bending and torsional motions of the wheelset with a limited degree of freedoms (DOFs).
- Modal superposition method [15, 16, 23-25]. The flexible vibration modes can be obtained using experimental (e.g., hammer test [26] and shaker [27]) and numerical approaches [28]. The accuracy of the flexibility representation depends on the number of modes employed.
- Finite element (FE) method. The geometry, mass and inertia of the wheelset can be realistically represented. Ideally, the FE method can achieve a nearly unbounded accuracy if sufficient number of DOFs and reliable material property are specified [12]. With the rapid development in computational power, the FE method attracts more attention when the mid- and high- frequency dynamics of the vehicle needs to be investigated [13, 29, 30].

1.3.2 TRACK DYNAMICS

For ballast track, the track subsystem composes of rails, fastenings, railpads, sleepers, ballast and subgrade. Generally speaking, the modelling of the track subsystem is more complicated compared to the vehicle subsystem, owing to the imperfect periodicity (e.g., inhomogeneous subgrade characteristics) and the non-linearity (e.g., complex constitutive equations of railpad and ballast materials) inside the track structure [12].

In the classical flexible track model, the rails are modelled as a Bernoulli-Euler or Timoshenko beam, and they are continuously supported on an elastic Winkler foundation [1]. With the model, the response of rails to moving load can be extracted analytically. To obtain better representation of other track components (e.g., railpads and sleepers), the model is extended from continuous support to discrete support [31, 32], and from one layer to multi-layer [33-37].

The track flexibility can also be represented using the moving track model [15, 19, 38, 39]. The moving track model requires low computational cost because of limited number of DOFs specified, so that it is suitable for simulating the long-distance vehicle-track interaction. The moving track model has been widely used by the commercial multi-body dynamics (MBD)

software such as GENSYS [40], VI-Rail [41] and SIMPACK [42], and can provide reliable solution up to 200 Hz [17].

1

1.3.3 FRICTIONAL WHEEL-RAIL CONTACT

The vehicle and track subsystems are integrated by means of wheel-rail contact into a whole vehicle-track system. In the literature, various wheel-rail contact algorithms were developed. In wheel-rail contact models, the normal and tangent contact problems are often solved separately. For the normal problem, the Hertz, semi-Hertz, multi-Hertz and non-Hertz theories have been developed [43-47]. For the tangent problem, the contact models can be classified into the following categories.

- **(Semi-) analytical method**

The 2D rolling contact problem was studied by Cater [48], where the rolling motion of a cylinder (wheel) on a plane (rail) was investigated analytically. Cater's solution is based on the half-space assumption, and can only account for the longitudinal creepage. Later, Johnson [49] extended Cater's method to the 3D cases, i.e., an elastic sphere rolling on an elastic half-space. Johnson is the pioneer to take the geometric spin into account, though the spin and creepage were analysed separately.

The rolling contact problems can also be solved using semi-analytical methods such as conjugate gradient method [50-53]. For more generalized scenarios involving complex contact geometry, nonlinear material, multiple contact patches and non-steady-state rolling, (semi-) analytical methods become inaccurate, costly or even inapplicable.

- **Kalker's numerical methods and derivatives**

Huge contributions to the solution of frictional wheel-rail contact were made by Kalker. He developed several numerical methods for different scenarios. The most well-known is the full variational method, which is established on the boundary element method (BEM) and implemented in his CONTACT [44]. Despite the assumptions of half-space and linear elasticity, the method is able to deal with arbitrary creepage and spin. However, Kalker's full method was considered not suitable for on-line simulations of vehicle dynamics due to the large computational cost. Alternatively, the FASTSIM algorithm, based on Kalker's simplified method [54, 55], was developed to achieve a balance between accuracy (around a 10% margin of error compared to the full method) and efficiency (around 1000 times faster than the full method) [56].

Kalker's methods were further developed for, for example, slip-dependency of friction coefficient [56, 57], influence of the rates of creepage and spin on the creep force [58] and conformal contact (which may occur between wheel flange root and rail gauge corner) [45].

- **FE method**

More complicated rolling contact problems have been successfully solved with the FE methods. The tire-road rolling contact problem was investigated in [59, 60], where the tire is modelled as deformable and the road as rigid. These FE models employ the arbitrary Lagrangian Eulerian formulation, which is suitable for the frictional rolling at steady state. In the model, an implicit integration scheme is used for the linear elastic material, and an explicit integration scheme is used for the viscoelastic material.

The tire-road contact belongs to finite deformation (or large deformation) problem. The wheel-rail contact, however, is an infinitesimal deformation (or small deformation) problem. To deal with the contact problem with infinitesimal deformation, the explicit integration scheme is appropriate, as numerical errors introduced by the regularization of the Coulomb's friction law in the implicit scheme [61] can be avoided and physical contact solutions can be obtained. An explicit FE model was developed to investigate the dynamic wheel-rail contact problem [62, 63] under various scenarios, such as complex contact geometry [64-66], nonlinear material [67], velocity-dependent friction [68], wave dynamics [69], noise generation [70] and thermo-mechanical behaviour [71].

1.3.4 WHEEL-RAIL INTERACTION AT CROSSING

In the literature, two types of numerical methods, i.e., MBD and FE methods, are widely used for the dynamic wheel-rail interaction at crossings.

In the MBD method, the moving track model [72, 73] (as discussed in Section 1.3.2) is suitable for simulating the wheel-rail interaction in the low-frequency range. Yet, the moving track model becomes less capable in the mid- and high- frequency range [35] because of the excessive simplifications on the geometry and flexibility of contact bodies. To overcome the challenges suffered by the moving track model, the FE method is introduced to represent the track dynamics [74-77]. Regarding the wheel-rail contact models, the normal contact is obtained using (semi- or multi-) Hertz theory, while Kalker's simplified method FASTSIM is employed if the tangential contact is concerned. Since these contact models are based on the half-space assumption, numerical errors may be introduced at crossings due to the presence of conformal contact and large variation in the contact angle [78, 79]. In addition, when accounting for the nonlinear material property of contact bodies, the normal and tangential contact become dependent on each other [67], which is disregarded in these contact models. To overcome the limitation of the MBD method in analysing the nonlinear material and complex contact geometry, an integrated approach was proposed by combining the MBD with the FE methods [80, 81]. In the approach, a MBD model was used to simulate the vehicle dynamics and provide the input (e.g., contact force and contact position) for the FE modelling of rail degradation.

The FE method provides an alternative way for the dynamic wheel-rail interaction at crossing when complex contact geometry and material plasticity are involved. In the FE method, the half-space assumption can be readily abandoned. An explicit FE model was developed in [82, 83] to simulate the dynamic wheel-crossing interaction. In the model, a wheel with a constant load on the axle moves over a short piece of crossing rails (with the length of 3 m) suspended on a Winkler foundation. The model was further improved through extending the dimension of the crossing model and including the missing components (e.g., railpad and sleeper) [84]. The FE method was also employed in [85, 86] to analyse the influence of train speed, train moving direction, axle load and rail material property on the degradation of crossings. Yet, these FE models focus on the normal contact behaviour, while the tangent contact (e.g., adhesion-slip state, shear traction and micro-slip) are incomplete, so that they cannot accommodate satisfactory accuracy when analysing rail degradation.

1.4 PREDICTION OF RAIL DEGRADATION

The service life of rails is limited by various types of degradation, including accumulated plastic deformation, wear and rolling contact fatigue (RCF). Plastic deformation comes from high contact stresses; it happens if the stresses in the material exceed a threshold value. Wear is the material loss at the wheel-rail interface; it occurs as long as the frictional contact exists. The mechanism of RCF is related to the initiation and propagation of cracks, corresponding to near-surface alternating stress field. RCF may result in the sudden failure of materials [87].

- **Plastic deformation**

Material plasticity can be evaluated using yield criteria. Von Mises yield criterion, also known as maximum distortion energy method, is commonly used to evaluate the plastic deformation of wheels and rails. Von Mises stress can be expressed as [88]

$$\sigma_v = \sqrt{\frac{1}{2} \left[(\sigma_{xx} - \sigma_{yy})^2 + (\sigma_{yy} - \sigma_{zz})^2 + (\sigma_{zz} - \sigma_{xx})^2 + 6(\sigma_{xy}^2 + \sigma_{yz}^2 + \sigma_{zx}^2) \right]} \quad (1.1)$$

where σ_{xx} , σ_{yy} and σ_{zz} are the normal stresses; and σ_{xy} , σ_{yz} and σ_{zx} are the shear traction.

Tresca yield criterion, also known as maximum shear traction method, is also commonly used for analysing the plastic deformation, which is expressed as [89]

$$\sigma_t = \frac{1}{2} \max(|\sigma_{xx} - \sigma_{yy}|, |\sigma_{yy} - \sigma_{zz}|, |\sigma_{zz} - \sigma_{xx}|) \quad (1.2)$$

- **Wear**

In the literature, the frictional work method and the sliding method are commonly used to predict the wear at the wheel/rail interface. In the frictional work method, wear corresponds to the energy dissipation, i.e., the work generated at the wheel/rail interface [45, 90-94]. At a node of the rail surface, the wear at the wheel/rail interface can be expressed as [95]

$$V_{wear} = k_s \int_0^T \tau s dt \quad (1.3)$$

where k_s is the wear coefficient, τ is the shear traction, s is the micro-slip, and T is the duration of wheel/rail contact at the node.

In the sliding method, wear is determined by parameters like the sliding distance, normal contact force and hardness of the material [96]. The method was initially proposed by Archard [97], the wear volume at the rail surface can be calculated using

$$V_{wear} = k_s \frac{F_n d}{H} \quad (1.4)$$

where F_n is the normal contact force, d is the sliding distance and H is the hardness of the material.

- **RCF**

There are several methods available for the prediction of RCF, such as the shakedown theory [98] and the energy dissipation method [99]. In the shakedown theory, the occurrence of RCF depends on the pressure and creep forces in the contact patch, i.e., surface cracking

will take place if the stresses exceed the shakedown limit [100]. In the energy dissipation model, the RCF damage is a function of the wear number [99]. The wear number is calculated as

$$T\gamma = T_x\gamma_x + T_y\gamma_y \quad (1.5)$$

where T_x and T_y are the longitudinal and lateral creep forces, γ_x and γ_y are the longitudinal and lateral creepage. The advantage of the energy dissipation model is that the competitive relation between wear and RCF can be taken into account [101].

1.5 DETECTION OF RAIL DEGRADATION

In the past, rail defects were detected via human visual inspection, i.e., the technicians visit the tracks or watch the videos of tracks recorded by inspection vehicles. The visual inspection is labor intensive, subjective and prone to human mistakes. Moreover, the visual method is almost infeasible for the early detection of rail defects. As a consequence, many of the rail defects are detected at a severe stage, when the safety of train operation is no longer guaranteed. The limitation of the human visual detection promotes the development of advanced inspection technologies [102], such as ultrasonic measurement, eddy current testing, magnetic induction, image recognition, thermography and acoustic emission system. These technologies can be classified into five categories based on the employed physical principles, i.e., visual-, wave-, electric-, magnetic-, vibration- and thermal- based methods.

- **Visual-based inspection**

Visual inspection method relies on the automatic recognition of images. In a visual inspection system, one or several optical cameras are instrumented on vehicles to capture the images of tracks, and a defect detection algorithm is developed to evaluate the type, location and severity of defects. Visual inspection systems can detect visible defects of rail surfaces [103] and other track components (e.g. moving sleeper and missing bolt [103]). The drawbacks of the systems are, on one hand, they are unable to provide any information regarding invisible defects (e.g. subsurface cracks and worn railpads); on the other hand, the hit rate of the system can be easily disturbed by illumination inequality, inconsistent reflection property and contamination [104].

- **Wave-based inspection**

Ultrasonic measurement and acoustic emission systems are the techniques that employ wave-based algorithms. Ultrasonic measurement has the best performance for detecting internal cracks at rail head and web [105]. The system can be realized via several types of platforms such as hand pushed trolley and inspection vehicles. Yet, the system is not suitable for surface defects without cracks, and its capability in detecting small (<4 mm) surface cracks is inadequate especially at high inspection speed [106]. Acoustic emission system is able to access the integrity of wheel and rail surfaces [107-109]. Yet, the on-board implementation of the acoustic emission system is disturbed by the noise generated by airflow, so that the system mainly focuses on indoor usage.

- **Electric- and magnetic-based inspection**

Eddy current testing and magnetic induction belong to the category of electric- and magnetic-based inspection. Eddy current testing can detect rail surface defects such as severe squats and corrugation [110, 111]. The detection mechanism employed by eddy current test is

to identify the changes in the magnetic field generated by eddy currents. Because the eddy current testing is very sensitive to the lift-off variation of the sensors, the probe needs to be positioned at a constant distance (less than 2 mm) from rail surface [112], which limits its application at the geometry discontinued crossings. The magnetic induction method can be used for near-surface or surface transverse defects [113]. The method also suffers from the restriction of a constant distance between sensors and rail surfaces.

- **Vibration-based inspection**

There exist several types of vibration-based inspection technologies, where the signals (e.g., acceleration, displacement and strain) at various vehicle components (e.g., axle box, bogie frame and wheel disc) are acquired. Each of them is suitable for certain irregularities and defects [114]. For example, ABA measurement can be used to detect short wavelength defects (<8 m), including both periodic defects (e.g., corrugation [115] and wheel flat [116, 117]) and isolated defects (e.g., squats [118], poor welds [119] and worn insulated joints [120]). Bogie acceleration measurement is able to evaluate long wavelength defects (>8 m), while primary suspension displacement measurement can be used to analyse the characteristics of wheel-rail contact.

- **Thermal-based inspection**

Thermography inspection belongs to the thermal-based method. In the method, a heater is positioned close to the surfaces of objects, while thermal images are captured with an infrared camera. The thermography can identify cracks [121] and evaluate the ballast conditions [122]. Yet, its on-board application can be disturbed by fluctuations of the weather conditions.

1.6 PROBLEM STATEMENT

The complex structure and discontinued geometry of railway crossings raise the dynamic loads during the passage of vehicles, making crossings one of the weakest points of the track infrastructure. In recent years, the situation becomes even worse as the railway system has to sustain the increasing demands of higher speed, greater capacity and longer service time. Therefore, it is necessary to have better modelling and monitoring of the dynamic wheel-crossing interaction, since they are important to guarantee the safety of train operation, extend the service life of crossing and minimize the maintenance cost. First, the numerical methods in the literature are to some extent insufficient to accurately reproduce the dynamic wheel-crossing interaction in the mid- and high- frequency range due to the simplifications. Second, precise analysis of rail defects relies on reliable wheel-rail contact parameters, whereas the works in the literature either suffer from challenges of complex contact geometry, nonlinear material and non-steady state, or overlook the tangent contact parameters. Finally, an efficient diagnosis system is required for the timely detection of crossing defects, so that preventive maintenance actions can be performed. Based on the preceding analysis, the objective of this dissertation is to answer the following questions:

- Q1** *How does the wheel-rail contact behaviour evolve during the passage of vehicles over crossings? How does the contact behaviour relate to the degradation of crossing rails?*
- Q2** *Whether and how does the wheel-rail contact behaviour differ between nominal and long-term serviced crossings? How to evaluate the performance of long-term serviced crossings under traffic loads?*

Q3 *What is the characteristic dynamic response during vehicle-track interaction at crossings? Whether and how does the ABA relate to the nature of the track structure?*

Q4 *Whether the ABA system can be used for the condition monitoring of crossings? If feasible, which kind of defects can be identified?*

1.7 OUTLINE OF THIS DISSERTATION

This dissertation aims to answer the above four research questions. The study will be carried out via a combination of numerical and experimental approaches. The organization of the dissertation is presented in Figure 1.4.

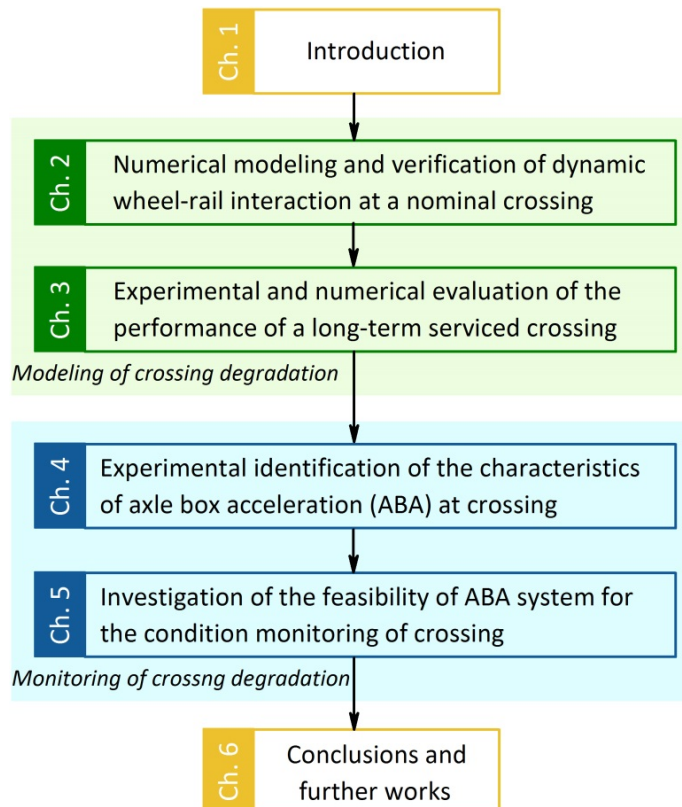


Figure 1.4: Outline of this dissertation

Chapter 2 proposes an explicit FE model capable of analysing the dynamic wheel-rail interaction at crossings. The simulated dynamic response in terms of the major frequencies and energy distribution of ABA is verified using in-situ ABA measurements. The evolution of wheel-rail contact parameters, i.e., contact force, contact position, contact patch, adhesion-slip state, pressure, shear traction and micro-slip, are elaborated during the passage of vehicles. These contact parameters are then used to predict the degradation of crossing rails due to plastic deformation and wear.

Chapter 3 investigates the characteristic wheel-rail contact behaviour of long-term serviced crossings. The 3D profile and hardness of a long-term serviced crossing are measured and serve as input to the FE modelling of the dynamic wheel-rail interaction. The simulated wheel-rail contact parameters are used to calculate the degradation of crossing rails due to plastic deformation and wear. By comparing the results between nominal and long-term serviced crossings, the characteristics of wheel-rail contact and rail degradation of long-term serviced crossing can then be extracted.

Chapter 4 analyses the characteristic dynamic response of wheel-rail interaction at crossings, which is essential for the development of an ABA system for condition monitoring of crossings. In-situ ABA measurements are conducted with various test parameters to analyse the influence of train speed, train moving direction and sensor positions on the characteristics of the ABA at crossing. Thereafter, a roving-accelerometer hammer test is carried out to address the relationship between the major frequencies of the ABA and the natural frequencies of crossings.

Chapter 5 investigates the feasibility of the ABA system for monitoring the degradation of crossings. In-situ ABA and 3D profile measurements were performed on reference crossings of the same type yet with different health conditions, so that the signature tune of ABA related to crossing degradation can be extracted. The capability of the ABA system is demonstrated via a trial detection conducted on a crossing with an degradation status unknown beforehand.

Chapter 6 draws the main conclusions and lists some possible further works.

REFERENCES

- [1] C. Esveld, *Modern railway track* (MRT-Productions, 2001).
- [2] B.A. Pålsson, J.C. Nielsen, *Wheel-rail interaction and damage in switches and crossings*, Vehicle System Dynamics **50**, 43-58 (2012).
- [3] ProRail, *Jaarverslag* (Utrecht, Netherland, 2015), pp. 127.
- [4] Z. Yang, Z. Li, R. Dollevoet, *An explicit integration finite element method for impact noise generation at a squat*, in *11th International Workshop on Railway Noise* (Uddevalla, Sweden, 2013), pp. 63-70.
- [5] S. Iwnicki, *Handbook of railway vehicle dynamics* (CRC press, 2006).
- [6] European Committee for Standardization, *Railway applications–Ride comfort for passengers–Measurement and evaluation* (2009), CSN EN 12299.
- [7] International Organization for Standardization, *Mechanical vibration and shock–Evaluation of human exposure to whole-body vibration–Part 1: General requirements* (1997), ISO 2631-1: 1997.
- [8] J.L. Escalona, H. Sugiyama, A.A. Shabana, *Modelling of structural flexibility in multibody railroad vehicle systems*, Vehicle System Dynamics **51**, 1027-1058 (2013).
- [9] A. Orvnäs, *Methods for reducing vertical carbody vibrations of a rail vehicle: a literature survey*, in *Report in Railway Technology* (Stockholm, Sweden, 2010).
- [10] J. Zhou, R. Goodall, L. Ren, H. Zhang, *Influences of car body vertical flexibility on ride quality of passenger railway vehicles*, Proceedings of the Institution of Mechanical Engineers, Part F: Journal of Rail and Rapid Transit **223**, 461-471 (2009).

[11] K. Knothe, S. Grassie, *Modelling of railway track and vehicle/track interaction at high frequencies*, Vehicle System Dynamics **22**, 209-262 (1993).

[12] K. Popp, H. Kruse, I. Kaiser, *Vehicle-track dynamics in the mid-frequency range*, Vehicle System Dynamics **31**, 423-464 (1999).

[13] M. Molodova, Z. Li, A. Núñez, R. Dollevoet, *Validation of a finite element model for axle box acceleration at squats in the high frequency range*, Computers & Structures **141**, 84-93 (2014).

[14] S. Bruni, I. Anastasopoulos, S. Alfi, A. Van Leuven, G. Gazetas, *Effects of train impacts on urban turnouts: Modelling and validation through measurements*, Journal of Sound and Vibration **324**, 666-689 (2009).

[15] N. Chaar, M. Berg, *Simulation of vehicle-track interaction with flexible wheelsets, moving track models and field tests*, Vehicle System Dynamics **44**, 921-931 (2006).

[16] P. Torstensson, J.C. Nielsen, L. Baeza, *Dynamic train-track interaction at high vehicle speeds—Modelling of wheelset dynamics and wheel rotation*, Journal of Sound and Vibration **330**, 5309-5321 (2011).

[17] N. Chaar, *Wheelset structural flexibility and track flexibility in vehicle-track dynamic interaction*, PhD dissertation, Royal Institute of Technology (2007).

[18] S. Zhong, J. Xiong, X. Xiao, Z. Wen, X. Jin, *Effect of the first two wheelset bending modes on wheel-rail contact behavior*, Journal of Zhejiang University-Science A **15**, 984-1001 (2014).

[19] E. Andersson, N. Nilsson, L. Ohlsson, *Lateral track forces at high speed curving comparisons of practical and theoretical results of swedish high speed train X2000*, Vehicle System Dynamics **25**, 37-52 (1996).

[20] E. Brommundt, *A simple mechanism for the polygonalization of railway wheels by wear*, Mechanics Research Communications **24**, 435-442 (1997).

[21] A. Matsumoto, Y. Sato, M. Tanimoto, K. Qi, *Study on the formation mechanism of rail corrugation on curved track*, Vehicle System Dynamics **25**, 450-465 (1996).

[22] B. Morys, *Enlargement of out-of-round wheel profiles on high speed trains*, Journal of Sound and Vibration **227**, 965-978 (1999).

[23] K. Popp, I. Kaiser, H. Kruse, *System dynamics of railway vehicles and track*, Archive of Applied Mechanics **72**, 949-961 (2003).

[24] K. Popp, K. Knothe, C. Pöpper, *System dynamics and long-term behaviour of railway vehicles, track and subgrade: report on the DFG Priority Programme in Germany and subsequent research*, Vehicle System Dynamics **43**, 485-521 (2005).

[25] C. Casanueva, A. Alonso, I. Eziolaza, J.G. Giménez, *Simple flexible wheelset model for low-frequency instability simulations*, Proceedings of the Institution of Mechanical Engineers, Part F: Journal of Rail and Rapid Transit **228**, 169-181 (2014).

[26] S. Cervello, G. Donzella, A. Pola, M. Scepi, *Analysis and design of a low-noise railway wheel*, Proceedings of the Institution of Mechanical Engineers, Part F: Journal of Rail and Rapid Transit **215**, 179-192 (2001).

[27] E. Tassilly, N. Vincent, *A linear model for the corrugation of rails*, Journal of Sound and Vibration **150**, 25-45 (1991).

[28] U. Fingberg, *A model of wheel-rail squealing noise*, Journal of Sound and Vibration **143**, 365-377 (1990).

[29] Z. Li, X. Zhao, R. Dollevoet, M. Molodova, *Differential wear and plastic deformation as causes of squat at track local stiffness change combined with other track short defects*, Vehicle System Dynamics **46**, 237-246 (2008).

[30] M. Molodova, Z. Li, A. Nunez, R. Dollevoet, *Parameter study of the axle box acceleration at squats*, Proceedings of the Institution of Mechanical Engineers, Part F: Journal of Rail and Rapid Transit **229**, 841-851 (2014).

[31] Y. Cheng, F. Au, Y. Cheung, *Vibration of railway bridges under a moving train by using bridge-track-vehicle element*, Engineering Structures **23**, 1597-1606 (2001).

[32] R. Dong, S. Sankar, R. Dukkipati, *A finite element model of railway track and its application to the wheel flat problem*, Proceedings of the Institution of Mechanical Engineers, Part F: Journal of Rail and Rapid Transit **208**, 61-72 (1994).

[33] G. Xie, S.D. Iwnicki, *Simulation of wear on a rough rail using a time-domain wheel-track interaction model*, Wear **265**, 1572-1583 (2008).

[34] M. Hiensch, J.C. Nielsen, E. Verheijen, *Rail corrugation in the Netherlands—measurements and simulations*, Wear **253**, 140-149 (2002).

[35] Z. Ren, S. Sun, W. Zhai, *Study on lateral dynamic characteristics of vehicle/turnout system*, Vehicle System Dynamics **43**, 285-303 (2005).

[36] V.L. Markine, M.J.M.M. Steenbergen, I.Y. Shevtsov, *Combatting RCF on switch points by tuning elastic track properties*, Wear **271**, 158-167 (2011).

[37] M. Hussein, H. Hunt, *A numerical model for calculating vibration due to a harmonic moving load on a floating-slab track with discontinuous slabs in an underground railway tunnel*, Journal of Sound and Vibration **321**, 363-374 (2009).

[38] I. Kaiser, K. Popp, *Interaction of elastic wheelsets and elastic rails: modelling and simulation*, Vehicle System Dynamics **44**, 932-939 (2006).

[39] Y. Bezin, S.D. Iwnicki, M. Cavalletti, E. De Vries, F. Shahzad, G. Evans, *An investigation of sleeper voids using a flexible track model integrated with railway multi-body dynamics*, Proceedings of the Institution of Mechanical Engineers, Part F: Journal of Rail and Rapid Transit **223**, 597-607 (2009).

[40] AB DEsolver, *GENSYS reference manual*, www.gensys.se.

[41] VI-grade GmbH, *VI-Rail 16.0 documentation*, www.vi-grade.com.

[42] W. Rulka, *SIMPACK—A computer program for simulation of large-motion multibody systems*, in *Multibody systems handbook* (Springer, 1990) pp. 265-284.

[43] H.R. Hertz, *Über die Berührung fester elastischer Körper und Über die Harte*, Verhandlung des Vereins zur Beförderung des Gewerbefleibes, Berlin 449 (1882).

[44] J.J. Kalker, *Three-dimensional elastic bodies in rolling contact* (Kluwer Academic Publishers, 1990).

[45] Z. Li, *Wheel-rail rolling contact and its application to wear simulation*, PhD dissertation, Delft University of Technology (2002).

[46] J. Pascal, G. Sauvage, *New method for reducing the multicontact wheel/rail problem to one equivalent contact patch*, Vehicle System Dynamics **20**, 475-489 (1992).

[47] W. Yan, F. Fischer, *Applicability of the Hertz contact theory to rail-wheel contact problems*, Archive of applied mechanics **70**, 255-268 (2000).

[48] F. Carter, *On the action of a locomotive driving wheel*, Proceedings of the Royal Society of London A: Mathematical, Physical and Engineering Sciences **112**, 151-157 (1926).

[49] K. Johnson, *The effect of a tangential contact force upon the rolling motion of an elastic sphere on a plane*, Journal of Applied Mechanics **25**, 339-346 (1958).

[50] V. Boucly, D. NĂŚlias, I. Green, *Modeling of the rolling and sliding contact between two asperities*, Journal of Tribology **129**, 235-245 (2007).

[51] T. Chaise, D. NĂŚlias, *Contact pressure and residual strain in 3D elasto-plastic rolling contact for a circular or elliptical point contact*, Journal of Tribology **133**, 041402 (2011).

[52] D. Nélias, G. Lormand, D. Girodin, *Development of a three-dimensional semi-analytical elastic-plastic contact code*, Journal of Tribology **124**, 653-667 (2002).

[53] G. Popescu, G.E. Morales-Espejel, B. Wemekamp, A. Gabelli, *An engineering model for three-dimensional elastic-plastic rolling contact analyses*, Tribology Transactions **49**, 387-399 (2006).

[54] J.J. Kalker, *A simplified theory for non-Hertzian contact*, Vehicle System Dynamics **12**, 43-45 (1983).

[55] J.J. Kalker, *A fast algorithm for the simplified theory of rolling contact*, Vehicle System Dynamics **11**, 1-13 (1982).

[56] J. Giménez, A. Alonso, E. Gómez, *Introduction of a friction coefficient dependent on the slip in the FastSim algorithm*, Vehicle System Dynamics **43**, 233-244 (2005).

[57] J. Piotrowski, *Kalker's algorithm Fastsim solves tangential contact problems with slip-dependent friction and friction anisotropy*, Vehicle System Dynamics **48**, 869-889 (2010).

[58] Z. Shen, J. Hedrick, J. Elkins, *A comparison of alternative creep force models for rail vehicle dynamic analysis*, Vehicle System Dynamics **12**, 79-83 (1983).

[59] U. Nackenhorst, *The ALE-formulation of bodies in rolling contact: Theoretical foundations and finite element approach*, Computer Methods in Applied Mechanics and Engineering **193**, 4299-4322 (2004).

[60] M. Ziefle, U. Nackenhorst, *Numerical techniques for rolling rubber wheels: treatment of inelastic material properties and frictional contact*, Computational Mechanics **42**, 337-356 (2008).

[61] P. Wriggers, *Computational contact mechanics* (Springer, 2006).

[62] X. Zhao, Z. Li, *The solution of frictional wheel-rail rolling contact with a 3D transient finite element model: Validation and error analysis*, Wear **271**, 444-452 (2011).

[63] Z. Wei, Z. Li, Z. Qian, R. Chen, R. Dollevoet, *3D FE modelling and validation of frictional contact with partial slip in compression-shift-rolling evolution*, International Journal of Rail Transportation **4**, 20-36 (2016).

[64] X. Deng, Z. Qian, R. Dollevoet, *Lagrangian explicit finite element modeling for spin-rolling contact*, Journal of Tribology **137**, 041401 (2015).

[65] Z. Li, X. Zhao, C. Esveld, R. Dollevoet, M. Molodova, *An investigation into the causes of squats—Correlation analysis and numerical modeling*, Wear **265**, 1349-1355 (2008).

1

- [66] Z. Li, X. Zhao, R. Dollevoet, *An approach to determine a critical size for rolling contact fatigue initiating from rail surface defects*, International Journal of Rail Transportation **5**, 16-37 (2017).
- [67] X. Zhao, Z. Li, *A three-dimensional finite element solution of frictional wheel-rail rolling contact in elasto-plasticity*, Proceedings of the Institution of Mechanical Engineers, Part J: Journal of Engineering Tribology **229**, 86-100 (2014).
- [68] X. Zhao, Z. Li, *A solution of transient rolling contact with velocity dependent friction by the explicit finite element method*, Engineering Computations **33**, 1033-1050 (2016).
- [69] Z. Yang, Z. Li, R. Dollevoet, *Modelling of non-steady-state transition from single-point to two-point rolling contact*, Tribology International **101**, 152-163 (2016).
- [70] Z. Yang, A. Boogaard, R. Chen, R. Dollevoet, Z. Li, *Numerical and experimental study of wheel-rail impact vibration and noise generated at an insulated rail joint*, International Journal of Impact Engineering **113**, 29-39 (2018).
- [71] M. Naeimi, S. Li, Z. Li, J. Wu, R.H. Petrov, J. Sietsma, R. Dollevoet, *Thermomechanical analysis of the wheel-rail contact using a coupled modelling procedure*, Tribology International **117**, 250-260 (2018).
- [72] C. Wan, V. Markine, I. Shevtsov, *Improvement of vehicle-turnout interaction by optimising the shape of crossing nose*, Vehicle System Dynamics **52**, 1517-1540 (2014).
- [73] B.A. Pålsson, J.C. Nielsen, *Dynamic vehicle-track interaction in switches and crossings and the influence of rail pad stiffness-field measurements and validation of a simulation model*, Vehicle System Dynamics **53**, 734-755 (2015).
- [74] E. Kassa, J.C. Nielsen, *Dynamic train-turnout interaction in an extended frequency range using a detailed model of track dynamics*, Journal of Sound and Vibration **320**, 893-914 (2009).
- [75] M. Wiest, E. Kassa, W. Daves, J.C. Nielsen, H. Ossberger, *Assessment of methods for calculating contact pressure in wheel-rail/switch contact*, Wear **265**, 1439-1445 (2008).
- [76] S. Alfi, S. Bruni, *Mathematical modelling of train-turnout interaction*, Vehicle System Dynamics **47**, 551-574 (2009).
- [77] C. Andersson, T. Dahlberg, *Wheel/rail impacts at a railway turnout crossing*, Proceedings of the Institution of Mechanical Engineers, Part F: Journal of Rail and Rapid Transit **212**, 123-134 (1998).
- [78] N. Burgelman, Z. Li, R. Dollevoet, *A new rolling contact method applied to conformal contact and the train-turnout interaction*, Wear **321**, 94-105 (2014).
- [79] J. Blanco-Lorenzo, J. Santamaría, E.G. Vadillo, N. Correa, *On the influence of conformity on wheel-rail rolling contact mechanics*, Tribology International **103**, 647-667 (2016).
- [80] D. Nicklisch, E. Kassa, J. Nielsen, M. Ekh, S. Iwnicki, *Geometry and stiffness optimization for switches and crossings, and simulation of material degradation*, Proceedings of the Institution of Mechanical Engineers, Part F: Journal of Rail and Rapid Transit **224**, 279-292 (2010).
- [81] A. Johansson, B. Pålsson, M. Ekh, J.C. Nielsen, M.K. Ander, J. Brouzoulis, E. Kassa, *Simulation of wheel-rail contact and damage in switches & crossings*, Wear **271**, 472-481 (2011).

[82] M. Pletz, W. Daves, H. Ossberger, *A wheel passing a crossing nose: Dynamic analysis under high axle loads using finite element modelling*, Proceedings of the Institution of Mechanical Engineers, Part F: Journal of Rail and Rapid Transit **226**, 603-611 (2012).

[83] M. Pletz, W. Daves, H. Ossberger, *A wheel set/crossing model regarding impact, sliding and deformation-Explicit finite element approach*, Wear **294**, 446-456 (2012).

[84] L. Xin, V. Markine, I. Shevtsov, *Numerical analysis of the dynamic interaction between wheel set and turnout crossing using the explicit finite element method*, Vehicle System Dynamics **54**, 301-327 (2016).

[85] M. Wiest, W. Daves, F. Fischer, H. Ossberger, *Deformation and damage of a crossing nose due to wheel passages*, Wear **265**, 1431-1438 (2008).

[86] J. Xiao, F. Zhang, L. Qian, *Numerical simulation of stress and deformation in a railway crossing*, Engineering Failure Analysis **18**, 2296-2304 (2011).

[87] A. Grabulov, *Fundamentals of rolling contact fatigue*, PhD dissertation, Delft University of Technology (2010).

[88] R.V. Mises, *Mechanik der festen Körper im plastisch-deformablen Zustand*, Nachrichten von der Gesellschaft der Wissenschaften zu Göttingen, Mathematisch-Physikalische Klasse **1913**, 582-592 (1913).

[89] H. Tresca, *Mémoires sur l'écoulement des corps solides*, Imprimerie impériale (1869).

[90] T. Pearce, N. Sherratt, *Prediction of wheel profile wear*, Wear **144**, 343-351 (1991).

[91] C. Rodkiewicz, Y. Wang, *A dry wear model based on energy considerations*, Tribology International **27**, 145-151 (1994).

[92] C. Andersson, A. Johansson, *Prediction of rail corrugation generated by three-dimensional wheel-rail interaction*, Wear **257**, 423-434 (2004).

[93] M. Ignesti, M. Malvezzi, L. Marini, E. Meli, A. Rindi, *Development of a wear model for the prediction of wheel and rail profile evolution in railway systems*, Wear **284**, 1-17 (2012).

[94] Z. Li, J.J. Kalker, *Simulation of severe wheel-rail wear*, in *6th International Conference on Computer Aided Design, Manufacture and Operation in the Railway and Other Mass Transit Systems* (Lisbon, Portugal, 1998) pp. 393-402.

[95] M. Hiensch, J.C.O. Nielsen, E. Verheijen, *Rail corrugation in The Netherlands—measurements and simulations*, Wear **253**, 140-149 (2002).

[96] C.R.Á. da Silva, G. Pintaude, *Uncertainty analysis on the wear coefficient of Archard model*, Tribology International **41**, 473-481 (2008).

[97] J. Archard, W. Hirst, *The wear of metals under unlubricated conditions*, Proceedings of the Royal Society of London A: Mathematical, Physical and Engineering Sciences, 397-410 (1956).

[98] A. Bower, K. Johnson, *Plastic flow and shakedown of the rail surface in repeated wheel-rail contact*, Wear **144**, 1-18 (1991).

[99] M. Burstow, *Whole life rail model application and development for RSSB—continued development of an RCF damage parameter*, Rail Standards and Safety Board, (London, UK, 2004).

[100] B. Dirks, R. Enblom, *Prediction model for wheel profile wear and rolling contact fatigue*, Wear **271**, 210-217 (2011).

[101] M. Hiensch, P. Wiersma, *Reducing switch panel degradation by improving the track friendliness of trains*, Wear **366**, 352-358 (2016).

[102] M.P. Papaelias, C. Roberts, C. Davis, *A review on non-destructive evaluation of rails: state-of-the-art and future development*, Proceedings of the Institution of Mechanical Engineers, Part F: Journal of Rail and rapid transit **222**, 367-384 (2008).

[103] Q. Li, S. Ren, *A real-time visual inspection system for discrete surface defects of rail heads*, IEEE Transactions on Instrumentation and Measurement **61**, 2189-2199 (2012).

[104] P.L. Mazzeo, M. Nitti, E. Stella, A. Distante, *Visual recognition of fastening bolts for railroad maintenance*, Pattern Recognition Letters **25**, 669-677 (2004).

[105] R.S. Edwards, S. Dixon, X. Jian, *Characterisation of defects in the railhead using ultrasonic surface waves*, NDT & E International **39**, 468-475 (2006).

[106] R. Clark, *Rail flaw detection: overview and needs for future developments*, NDT & E International **37**, 111-118 (2004).

[107] X. Zhang, N. Feng, Y. Wang, Y. Shen, *Acoustic emission detection of rail defect based on wavelet transform and Shannon entropy*, Journal of Sound and Vibration **339**, 419-432 (2015).

[108] N. Thakkar, J. Steel, R. Reuben, *Rail-wheel interaction monitoring using Acoustic Emission: A laboratory study of normal rolling signals with natural rail defects*, Mechanical Systems and Signal Processing **24**, 256-266 (2010).

[109] K. Bruzelius, D. Mba, *An initial investigation on the potential applicability of Acoustic Emission to rail track fault detection*, NDT & E International **37**, 507-516 (2004).

[110] R. Pohl, A. Erhard, H.-J. Montag, H.-M. Thomas, H. Wüstenberg, *NDT techniques for railroad wheel and gauge corner inspection*, NDT & E International **37**, 89-94 (2004).

[111] M. Papaelias, M. Lugg, *Detection and evaluation of rail surface defects using alternating current field measurement techniques*, Proceedings of the Institution of Mechanical Engineers, Part F: Journal of Rail and Rapid Transit **227**, 310-321 (2012).

[112] H.-M. Thomas, T. Heckel, G. Hanspach, *Advantage of a combined ultrasonic and eddy current examination for railway inspection trains*, Insight-Non-Destructive Testing and Condition Monitoring **49**, 341-344 (2007).

[113] K. Miya, *Recent advancement of electromagnetic nondestructive inspection technology in Japan*, IEEE Transactions on magnetics **38**, 321-326 (2002).

[114] C.P. Ward, P. Weston, E. Stewart, H. Li, R.M. Goodall, C. Roberts, T. Mei, G. Charles, R. Dixon, *Condition monitoring opportunities using vehicle-based sensors*, Proceedings of the Institution of Mechanical Engineers, Part F: Journal of Rail and Rapid Transit **225**, 202-218 (2011).

[115] A. Massel, *Power spectrum analysis—modern tool in the study of rail surface corrugations*, NDT & E International **32**, 429-436 (1999).

[116] S. Alfi, F. Braghin, S. Bruni, *Numerical and experimental evaluation of extreme wheel-rail loads for improved wheelset design*, Vehicle System Dynamics **46**, 431-444 (2008).

[117] M. Bocciolone, A. Caprioli, A. Cigada, A. Collina, *A measurement system for quick rail inspection and effective track maintenance strategy*, Mechanical Systems and Signal Processing **21**, 1242-1254 (2007).

[118] M. Molodova, Z. Li, A. Núñez, R. Dollevoet, *Automatic detection of squats in railway infrastructure*, IEEE Transactions on Intelligent Transportation Systems **15**, 1980-1990 (2014).

[119] M. Molodova, Z. Li, R. Dollevoet, *Axle box acceleration: Measurement and simulation for detection of short track defects*, Wear **271**, 349-356 (2011).

[120] M. Oregui, S. Li, A. Núñez, Z. Li, R. Carroll, R. Dollevoet, *Monitoring bolt tightness of rail joints using axle box acceleration measurements*, Structural Control and Health Monitoring **24**, (2017).

[121] J. Wilson, G. Tian, I. Mukriz, D. Almond, *PEC thermography for imaging multiple cracks from rolling contact fatigue*, NDT & E International **44**, 505-512 (2011).

[122] M. Clark, D. McCann, M. Forde, *Infrared thermographic investigation of railway track ballast*, NDT & E International **35**, 83-94 (2002).

2

MODELLING AND VERIFICATION OF WHEEL-RAIL IMPACT AT CROSSING

Irregularities in the geometry and flexibility of railway crossings cause large impact forces, leading to rapid degradation of crossings. Precise stress and strain analysis are essential for understanding the dynamic frictional contact and the related failures at crossings. In this chapter, the distributions of frictional work and plastic deformation due to wheel-rail impact at railway crossings were investigated using the FE method. The simulated dynamic response was verified through comparisons with in situ axle box acceleration measurements. Our focus was on the contact behaviour, accounting for not only the dynamic contact force, but also the adhesion-slip regions, shear traction and micro-slip. The contact behaviour was then used to calculate the plastic deformation and frictional work. The results suggest that the normal and tangential contact forces on the wing rail and crossing nose are out-of-sync during the impact, and that the maximum values of both the plastic deformation and frictional work at the crossing nose occur during two-point contact stage rather than, as widely believed, at the moment of maximum normal contact force. These findings could contribute to the analysis of non-proportional loading in the materials and lead to a deeper understanding of the damage mechanisms. The model provides a tool for both damage analysis and structure optimization of crossings.

This chapter is based on:

Wei Z, Shen C, Li Z, Dollevoet R. Wheel-rail impact at crossings: relating dynamic frictional contact to degradation. *Journal of Computational and Nonlinear Dynamics* 12 (2017): 041016.

2.1 INTRODUCTION

Switches and crossings (S&C, turnouts) intersecting different tracks at the same level, are fundamental components of track systems. An overview of a railway crossing is shown in Figure 2.1. Because of irregularities in the geometry and flexibility of S&C, such as the gap between the closure rail and the crossing nose as well as the variation in the sleeper spans, high dynamic forces can be exerted as vehicles pass. The resulting degradation of S&C happens much faster than that of plain tracks, increasing maintenance costs and disrupting the operation of railway networks. For example, 7195 crossings served the Dutch railway network in the year 2012 [1]; of these, about 400 crossings were replaced, and 100 of these replacements were urgently required [2].

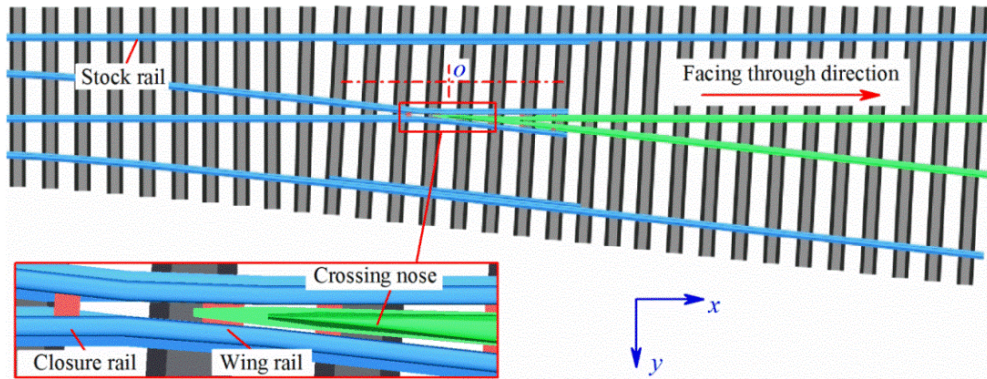


Figure 2.1: FE model of a right-hand crossing panel

Measures have been developed and applied to decrease the dynamic force and the resulted damage at S&C, e.g., movable point frog which is widely used on high-speed lines. However, rigid crossings are still common on conventional railway lines, and it is difficult to significantly decrease crossing damage using the current design, construction, and maintenance methods. A better understanding is therefore needed for the characteristics of wheel-rail frictional contact at crossings, especially that corresponding to impact.

The MBD method is often used for the analysis of dynamic wheel-rail interaction at crossing. In this method, the vehicle and crossing components are modelled as combinations of rigid or flexible bodies, springs and dampers. To account for the variations in geometry and flexibility of the crossing panel, Andersson *et al.* [3] developed a simplified numerical model in which the vehicle is modelled using the MBD method, and the rails and sleepers are treated as beams. Regarding the contact between wheels and rails, only the normal solution was taken into account using nonlinear Hertz spring, whereas the tangential solution was neglected. This approach was improved by Kassa *et al.* [4] by including the missing degrees of freedom of both vehicle and crossing panel, e.g., the lateral translation as well as the yaw and pitch rotation of a vehicle. This allowed the vehicle to move in a diverging route. The tangential solution of the wheel-rail interaction was considered using FASTSIM. Similar methods were also developed in other studies [5-10]. In these approaches, the solution of the wheel-rail contact is restricted by the linear elasticity and half-space assumptions, which make these methods incapable of treating nonlinear material behaviour such as plastic deformation and

strain rate dependency. In addition, because frictional contact and structural vibration are solved independently, the influence of the dynamic wheel-rail interaction on the evolution of frictional contact, for example by the inertia effect or wave propagation, may not be properly taken into account. To overcome the preceding challenges suffered by the MBD method, an integrated approach was proposed by combining the MBD and FE methods [11-12], in which the MBD model provided the input for the FE simulation of the degradation of crossing rails.

With the rapid development of computational power, the FE method attracts more attentions as an alternative approach to the study of dynamic wheel-rail interactions. Li *et al.* [13] successfully simulated wheel-rail impact using the FE method in a study of short wavelength defects on straight tracks. However, the interaction between the wheelset and the crossing is more complicated by the complex contact geometry and structure of the crossing panel. The dynamic behaviour of wheels passing through a crossing was studied by Wiest *et al.* [14] in which the plastic deformation of the crossing nose because of cyclic loading was investigated. In their model, the gap between the closure rail and crossing nose was neglected. Instead, the geometric irregularity was modelled by inclining the crossing nose with an angle. However, this simplification is unable to yield accurate dynamic responses and precise contact solutions. A more sophisticated FE model of a wheel passing through a crossing was presented by Pletz *et al.* [15]. Their model included a wheel with constant loading on the axle and a section of crossing panel suspended on a Winkler foundation. The focus of their work was on the normal contact, whereas the analysis on the tangential problem, which is essential for an insightful understanding of the frictional contact behaviour, such as tangential force and surface shear traction, is incomplete. Besides, further verification is required for the normal solution, because the simulated dynamic contact force produces different outcomes to both other numerical approaches and in situ measurements (see Figure 2.8 in [16]). Recently, in situ ABA measurements have been shown to be capable of detecting short wavelength irregularities in straight tracks [17-19] by identifying certain characteristic responses. The complex geometry of crossings can be regarded as a kind of irregularity, ABA measurement should be able to capture the characteristic dynamic responses of wheel-rail impact at crossings.

In this chapter, a contact model capable of simulating wheel-rail impact at crossing was developed using the FE method. Precise contact solutions during the impact were obtained and used for the analysis of crossing nose degradation. The structure of the chapter is as follows. The modelling of the wheelset and the crossing panel, and the calculating procedure, are described in Section 2.2. In Section 2.3, the simulated dynamic response is verified using in situ ABA measurements. In Section 2.4, the evolution of frictional contact during the impact is examined. Special attention is paid to the reliable contact solution, including not only dynamic contact force, but particularly the distribution of adhesion-slip regions, shear traction and micro-slip. In Section 2.5, the contact solution is then used to calculate the degradation of the crossing caused by plastic deformation and frictional work. The results are discussed in Section 2.6, and the main conclusions are drawn in Section 2.7.

2.2 MODELLING OF WHEEL-RAIL INTERACTION AT CROSSING

This section describes the FE model capable of simulating the wheel-rail interaction at crossing, including 1) modelling of wheelset and crossing panel, 2) modelling of wheelset motion and 3) simulation procedure.

2.2.1 WHEELSET AND CROSSING PANEL

The crossing used in this chapter is a right-hand constructed turnout of the 54E1-1:9 type with a nominal rail profile of UIC54 and a crossing angle of 1:9. The length of the crossing model was 17.8 m, which is equal to 30 sleeper spans and which has proved to be reasonable for the wheel-rail impact [20]. The rails and sleepers were modelled with solid elements, while the railpads and ballast were modelled as linear springs and viscous dampers. The modelling of the railpads and ballast is shown in Figure 2.2. A railpad consists of a uniform grid of 3×4 discretely distributed spring-damper pairs, divided into three rows (along the longitudinal direction x) and four columns (along the lateral direction y). The ballast under each sleeper consists of a uniform grid of 3×9 discretely distributed spring-damper pairs, divided into three rows and nine columns. The parameters of the railpad and ballast were obtained from in situ hammer test on the Dutch railway [21]. The stiffness and damping were 1560 MN/m and 67.5 kNs/m for a standard railpad, with the corresponding values for each spring-damper pair being 130 MN/m (1560/12) and 5.6 kNs/m (67.5/12). The stiffness and damping of the ballast were 90 MN/m and 64 kNs/m for a standard concrete sleeper, with the corresponding values for each spring-damper pair being 3.3 MN/m (90/27) and 2.4 kNs/m (64/27).

One wheelset of a Dutch ICR type locomotive was modelled using solid elements, whereas both the car body and the bogie were simplified as a lumped mass and supported on the wheelset axle by linear springs and viscous dampers. The wheel profile was UIC S1002, the axle load was 16 tons, and the stiffness and damping of the primary suspension were 1150 kN/m and 2500 Ns/m, respectively.

To account for the plastic deformation of the wheelset and the rail, a bilinear elasto-plastic material model was employed. The density, Young's modulus, yield strength, and Poisson's ratio of the wheel are 7800 kg/m^3 , 210 GPa, 835 MPa, and 0.29; while the corresponding values of the crossing rails are 7800 kg/m^3 , 190 GPa, 1000 MPa, and 0.3. The friction between the wheelset and the rail was defined using Coulomb's friction law, and the friction coefficient μ was set to 0.5 for dry and clean wheel-rail contact surfaces.

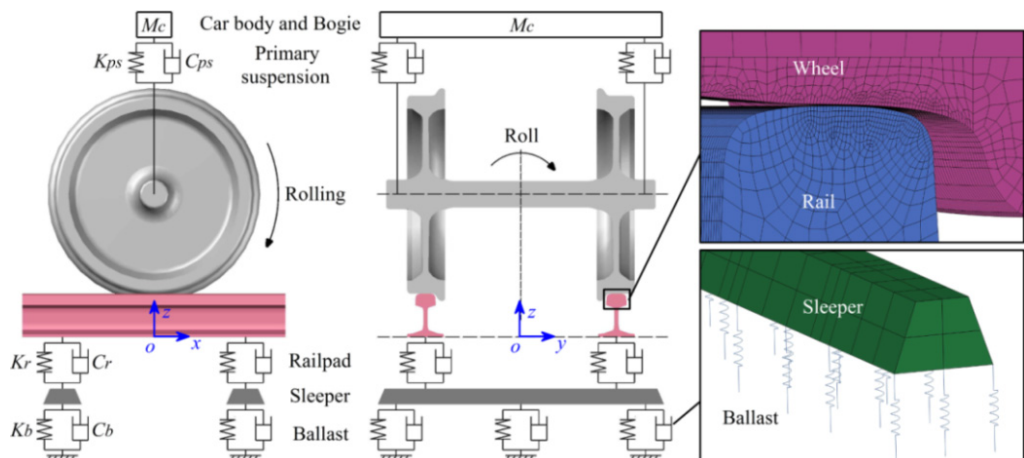


Figure 2.2: Schematic diagram of wheel-rail interaction with the close-ups of mesh

2.2.2 MOTION OF WHEELSET

A three-dimensional Cartesian coordinate was adopted, with the axes x , y , and z oriented in the longitudinal, lateral, and vertical directions. The origin o was at the intersection of the three planes: the xy plane across the rail foot, the xz plane across the centreline of the through track, and the yz plane across the tip of the crossing nose. In the FE model, the motion of the wheelset is defined as follows:

- Longitudinal translation and rolling rotation about the y axis: they are prescribed by specifying the driving torque and the initial angular velocity on the wheelset, and specifying the initial translational velocity on both the carbody and wheelset.
- Lateral translation and yaw rotation about the z axis: no constraints are imposed on them. The wheelset follows the through route guided by the wheel-rail contact, and the resulted lateral displacement and yaw angle can happen yet with small values (e.g. the lateral displacement is smaller than 1 mm in [22]).
- Vertical translation and roll rotation about the x axis: they are a part of the dynamic response of wheel-rail interaction, so that the values can neither be specified at the initial stage nor be fixed.

2.2.3 SIMULATION PROCEDURE

The commercial code AYSYS/LS-DYNA was used in this chapter. In the FE model, all continua, i.e., wheelset, rails, and sleepers, were meshed with 8-node solid elements, with a minimum element size of 0.6×0.6 mm in the contact patch, see the inset of Figure 2.2. The capacity of the proposed FE model in analysing the dynamic wheel-rail interaction is demonstrated in [23], where the contact solutions in terms of adhesion-slip state, contact stresses and micro-slip coincide well with the Hertz theory and Kalker's computer program CONTACT. For more generalized contact problems, the FE solutions are validated with Spence's semi-analytical method for frictional compression, Cattaneo's analytical method for frictional shift and Kalker's CONTACT for frictional rolling [24]. The FE model should be able to produce reliable contact solutions during wheel-rail interaction at crossings.

The dynamic response and contact solution of the FE model are obtained with a combination of a static analysis using an implicit integration method and a dynamic analysis using an explicit integration method. The static analysis is used to calculate the static equilibrium under gravity assuming that the wheelset stands still on the crossing. This step is necessary to avoid the unrealistic vibration that may be caused by in-equilibrium state of the system. The nodal displacements calculated from the static analysis define the initial state of the dynamic analysis when stress initialization is performed in the explicit integration method. Thereafter, initial translational and angular velocities as well as driving torque are applied on the wheelset and carbody to simulate the passage of the wheelset on the crossing.

The initial kinematic and dynamic solutions were obtained in a global three-dimensional Cartesian coordinate system. To determine the detailed contact solution in the contact patch, e.g., shear traction, micro-slip, and frictional work, a local coordinate system is required. A Fortran program was developed for deriving the coordinate transformation and for calculation of the adhesion-slip regions, micro-slip, and frictional work in the contact patches.

In the explicit analysis, the kinematic and dynamic results (e.g. nodal displacement and force) are calculated in the global coordinate system $oxyz$. These nodal results are then projected to local Cartesian coordinate $o'\alpha\beta\gamma$ using Equations (1) and (2) of [25]. In the local coordinate $o'\alpha\beta\gamma$, the origin o' invariably located at the contact patch centre and moving with it, with the axes α , β and γ oriented in the rolling, transversal and normal directions, as shown in Figure 2.3. Thereafter, the contact solutions can be obtained in each local coordinate system. A node is located in the contact patch if

2

$$|F_{n_N}| \geq \varepsilon_N \quad (2.1)$$

In addition, the node is located in the adhesion region if

$$\mu|F_{n_N}| - |F_{n_T}| \geq \varepsilon_T \quad (2.2)$$

where F_{n_N} is the normal nodal force along the normal direction γ , F_{n_T} is the tangential nodal force in the tangent plane $o'\alpha\beta$, ε_N and ε_T are tolerances. Here, ε_N is set to be 0.15% of the maximum normal nodal force on the rail surface, while ε_T is set to be 0.4% of the maximum tangential force on the rail surface.

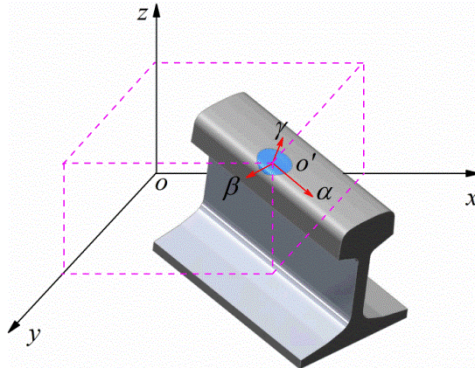


Figure 2.3: Coordinate transformation

The frictional work W_f at a node of the rail surface is calculated as [26]:

$$W_f = \int_0^t \tau s dt = \sum_{i=1}^n \tau_i s_i \Delta t \quad (2.3)$$

where τ and s are the surface shear traction and micro-slip, Δt is the output time step. Here, Δt is set to 4×10^{-5} s, at which the wheelset translates 0.84 mm along the longitudinal direction x with the speed of 21 m/s.

2.3 VERIFICATION OF THE SIMULATED DYNAMIC RESPONSE

In situ ABA measurement was employed to verify the simulated dynamic response of the wheel-rail interaction at the crossing panel. An accelerometer was mounted on the axle box in the vertical direction, and a GPS locator was used to record the location of the acceleration signal and the train speed. The ABA signal was recorded at a sampling frequency of 25.6 kHz

and was further low-pass filtered with the frequency of 1 kHz. The crossing was in good condition during the measurement. To confirm the replicability and reliability, the measurement was taken twice using the same train on the same crossing panel. In both measurements, the train passed through the crossing panel with approximately 21 m/s in the facing-through direction, i.e., from closure to crossing nose.

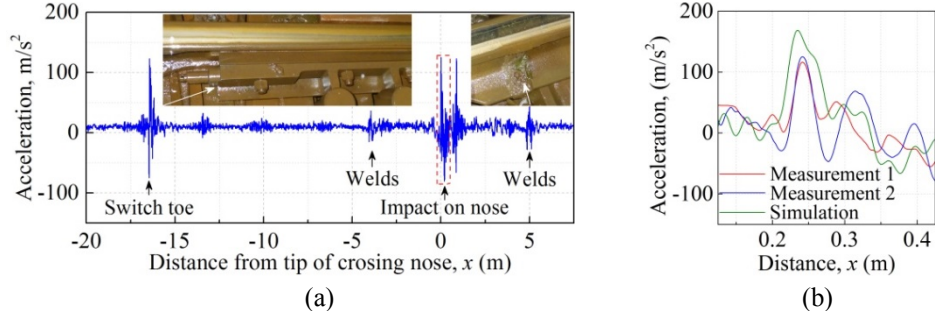


Figure 2.4: Time history of ABA. (a) Measured signal from a global view; (b) Comparison of ABA signals at the impact.

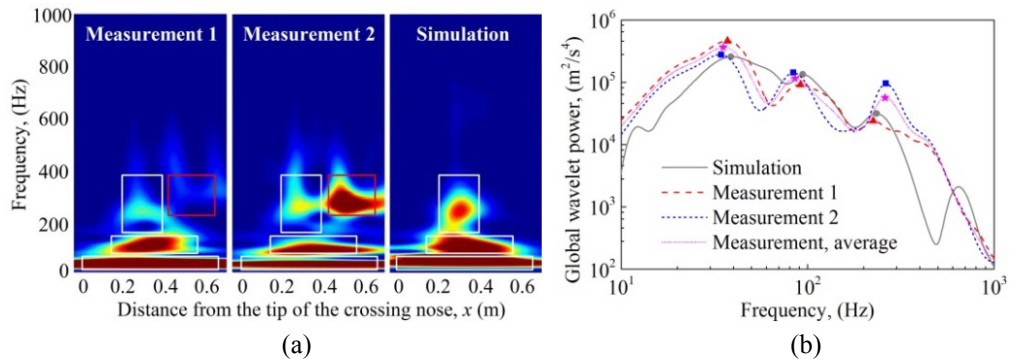


Figure 2.5: Wavelet analysis of the ABA signals. (a) Wavelet power spectrum of measured and simulated ABA. The white rectangles indicate the major frequency contents. The red rectangles mark the main difference between measurements. The impact happens at approximately 0.25 m from the tip of the crossing nose. (b) Global wavelet power spectra of measured and simulated ABA. The major frequency characteristics are around 35, 90 and 250 Hz.

Figure 2.4 shows the time history of the ABA signals. To obtain an insight into the characteristic time and frequency response of wheel-rail impact at crossings, wavelet transform analysis was used to extract the characteristic waveform from the measured and simulated ABA signals. In wavelet analysis, the signal processing is independent of the window size, making it suitable for investigating the transient processes of brief events. Figure 2.5(a) compares the wavelet power spectrum between the measured and simulated ABA, where the color bar shows the amount of energy concentrated at a certain location (the horizontal axis) and frequency (the vertical axis). Figure 2.5(b) shows the global wavelet spectra, defined as the wavelet spectrum averaged over the location at each frequency [27].

As can be seen from Figure 2.5, the measured and simulated signals were in good agreement in terms of the major frequency contents, wavelet power and impact position. The FE model captured the three major frequency characteristics, which arose around 35, 90 and 250 Hz (marked with white rectangles). The frequencies around 90 and 250 Hz were in the region where the wheelset jumped from the wing rail to the crossing nose, and were therefore related to the impact of the wheelset on the crossing nose. The 35 Hz frequency appeared before the impact region and was distributed along a longer distance, and at first glance seems irrelevant to the impact. However, the wavelet power, depicted by the colour, is higher around the impact region than elsewhere, suggesting that this frequency was also further excited by the impact.

Field observations (e.g., Figure 2 in [12] and Figure 2(c) in [14]) have shown that degradation will develop and accumulate at the location of the impact, exacerbating the impact, and extending and accelerating the degradation. It is thus highly likely that in degraded conditions the energy concentration can occur at a frequency higher than 250 Hz.

Because of randomness in the train-track system, the moving trajectory of the wheelset was different at each measurement. Therefore, each measured signal was somewhat different, as shown in Figure 2.5. For the same reason, it was difficult to achieve a precise match between the measurements and the simulation. Nevertheless, the major characteristics could be captured. It can be concluded that the FE model is able to represent the main dynamic characteristics of wheel-rail impact at crossing panel.

2.4 EVOLUTION OF FRICTIONAL WHEEL-RAIL CONTACT

The evolution of the frictional rolling contact as the wheelset passed through the crossing panel was investigated, and the adhesion-slip regions, pressure, surface shear traction, and micro-slip on the local surface of the wheel were determined. In the simulation, the wheelset passed through the crossing panel at 21 m/s in the facing-through direction. The wheelset is driven by a constant torque prescribed on the axle, which is expected to generate a longitudinal traction force equal to 30% of the static normal load when the inertia of the wheelset is ignored. During dynamic wheel-rail interaction, the ratio of the tangential contact force to the normal contact force varies with time along the track, and its variation can be exacerbated by the geometric discontinuity of crossings.

2.4.1 CONTACT FORCE

Figure 2.6 shows the time series of the normal contact force. As can be seen, the force on the stock rail fluctuated around the static load (84.3 kN), and the amplitude of the fluctuation reached a maximum of 24.9% during the transition. The force on the closure/wing rail fluctuated with a similar amplitude until the wheel jumped from the wing rail to the crossing nose. During the jump, the normal contact force on the wing rail dropped while the force on the crossing nose rose sharply, reaching its maximum value of 167.1 kN within 2 ms. This is approximately double the static load. Thereafter, the normal contact force decreased, returning to the static load.

2.4.2 CONTACT POSITION

To gain an insight into the evolution of the frictional contact during the transition, four instants (see Figure 2.6) were selected and a detailed analysis of the contact solutions was made at these instants. Figure 2.7 shows the contact status at each instant. The location of the contact patch when the wheelset was on the closure rail is given in Figure 2.7(a), where the contact was between the wheel tread and the rail top. Because the longitudinal axis of the wing rail was no longer aligned with the rolling direction of the wheelset (see Figure 2.1), the contact patch moved towards the field side of the wheel tread from t_1 to t_2 , as shown in Figure 2.7(b). The contact patch moved towards the field side of the wheel tread from t_3 to t_4 , as shown in Figure 2.7(c).

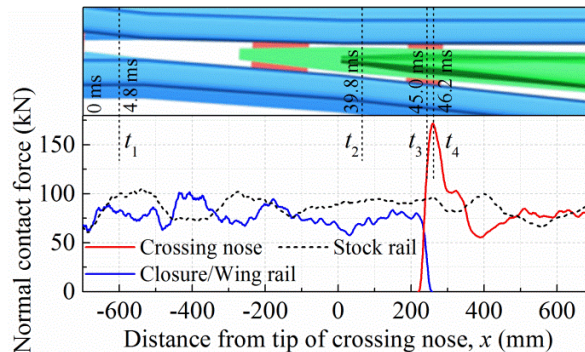


Figure 2.6: Time history of normal contact force in facing-through motion. The starting point (0 ms) is at 700 mm ahead of the nose tip.

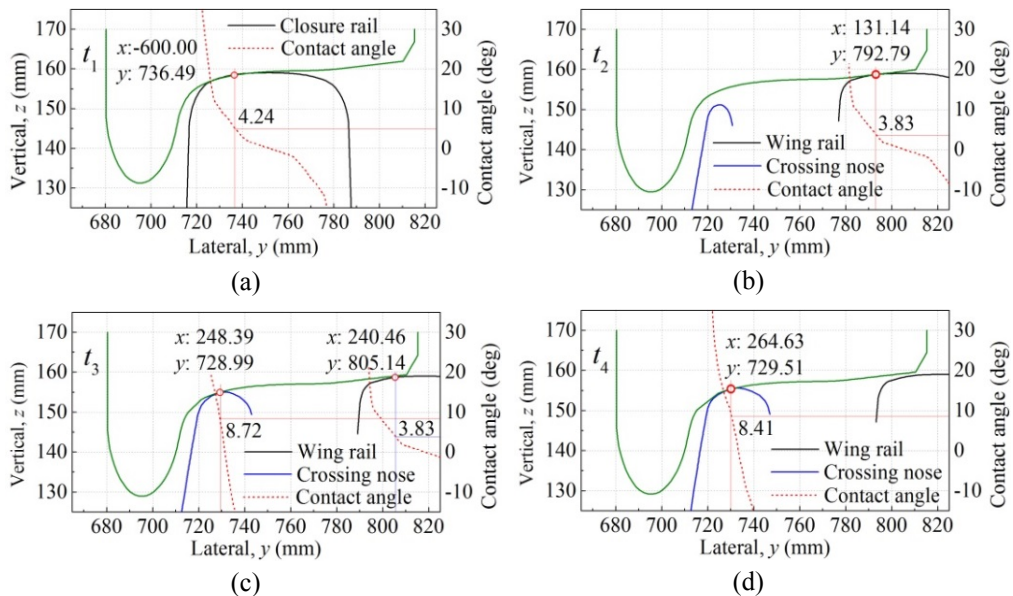


Figure 2.7: Contact status during the transition with the centre of the contact patch shown as \circ

Because the lateral-vertical sectional profile of the crossing nose widened along the longitudinal direction, the flange root of the wheel started to make contact with the crossing nose as the wheel rolled further from t_2 to t_3 . Hence, the situation of two-point contact occurred, an example of which is shown in Figure 2.7(c). Thereafter, the wheel gradually lost its contact with the wing rail and was supported solely by the crossing nose. Figure 2.7(d) shows the moment when the normal contact force on the crossing nose reached its maximum value. Note that the longitudinal coordinates x of the two contact patches at t_3 (Figure 2.7(c)) were different, being 240.46 mm on the wing rail and 248.39 mm on the crossing nose, respectively. This was attributed to the complex geometry of the crossing nose, in particular the rise in its height along the rolling direction. As a result, the centre of the contact patch on the crossing nose shifted forward in the rolling direction.

2.4.3 CONTACT STRESSES

Table 2.1 summarizes the contact solution at the four instants and Figure 2.8 presents the evolution of the adhesion-slip regions during the transition. As shown in Figure 2.8(a), the contact patch approximated the shape of an ellipse at t_1 . When the wheelset arrived at the wing rail, the contact patch rotated slightly clockwise (see Figure 2.8(b)) and became longer and narrower because of the misalignment between the rolling direction of the wheelset and the longitudinal axis of the wing rail. The size of the contact patch dropped by 6% from t_1 to t_2 , whereas the adhesion region increased from 51% to 69%.

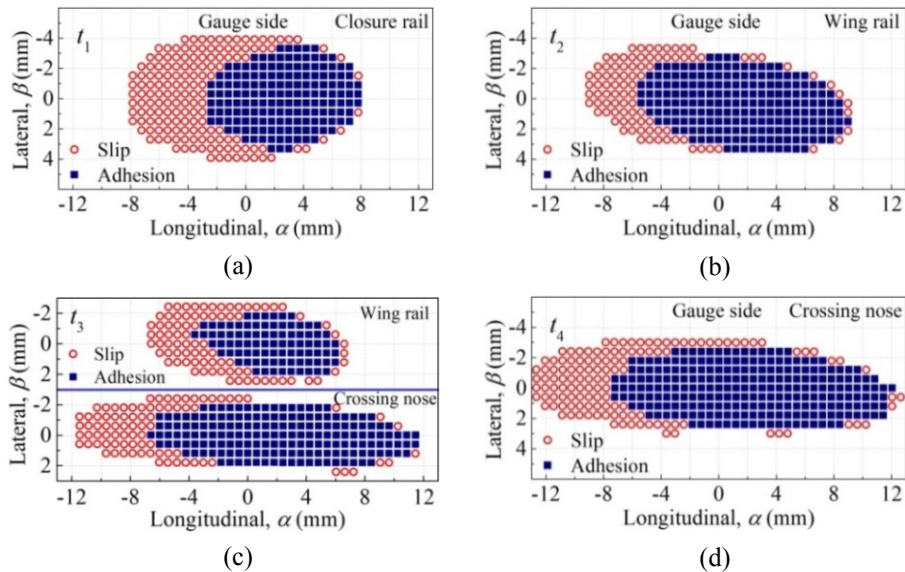


Figure 2.8: Distribution of adhesion-slip regions

As soon as the wheelset got contact with the crossing nose, the contact patch on the crossing nose grew whereas that on the wing rail shrank. At t_3 , the two contact patches were of equal width, but significantly different lengths (Figure 2.8(c)). This reflected the different radii of the wheel and rail profiles at their respective contact patches. The lateral radius of the wheel flange root is smaller than that of the wheel tread, whereas the lateral radius of the crossing

nose was smaller than that of the wing rail. The two contact patches on the crossing nose shown in Figure 2.8(c) and (d) appeared similar. The length and width, which were influenced by the widening of the crossing nose in the rolling direction, increased by 11% and 25% from t_3 to t_4 . The sectional profile of the crossing nose would eventually evolve into the normal UIC54 type, and the distribution of adhesion-slip regions would be analogous to that at t_1 .

Table 2.1: Contact solution during the transition

Time	Location	Contact patch			Max. contact force (kN)	Max. pressure (MPa)	Max. shear traction (MPa)
		$o'\alpha$ (mm)	$o'\beta$ (mm)	Area (mm ²)			
t_1	Closure rail	7.8	3.9	104.4	82.7	1317.6	616.9
t_2	Wing rail	9.0	3.3	98.7	74.9	1757.4	594.1
t_3	Wing rail	6.6	2.4	55.8	42.9	1169.7	551.3
t_3	Nose	11.4	2.4	94.0	108.3	2179.0	849.3
t_4	Nose	12.6	3.0	133.6	167.1	2303.4	858.0

Figure 2.9 shows the field of the surface shear traction during the transition. The maximum value of the shear traction was at the junctions between the adhesion and slip regions. At t_1 , the shear traction vectors pointed in approximately the moving direction of the wheelset. The small lateral components observed in Figure 2.9(a) can be attributed to geometric spin arising from the contact angle between the rolling axis of the wheelset and the local areas of the contact patch (see Figure 2.7(a)). As soon as the wheelset arrived at the wing rail, the rolling direction of the wheelset was no longer aligned with the longitudinal axis of the wing rail, and the contact patch moved from the tread towards the field side of the wheel. As a result, lateral creepage arose, and the lateral components of the shear traction at t_2 became larger (see Figure 2.9(b)).

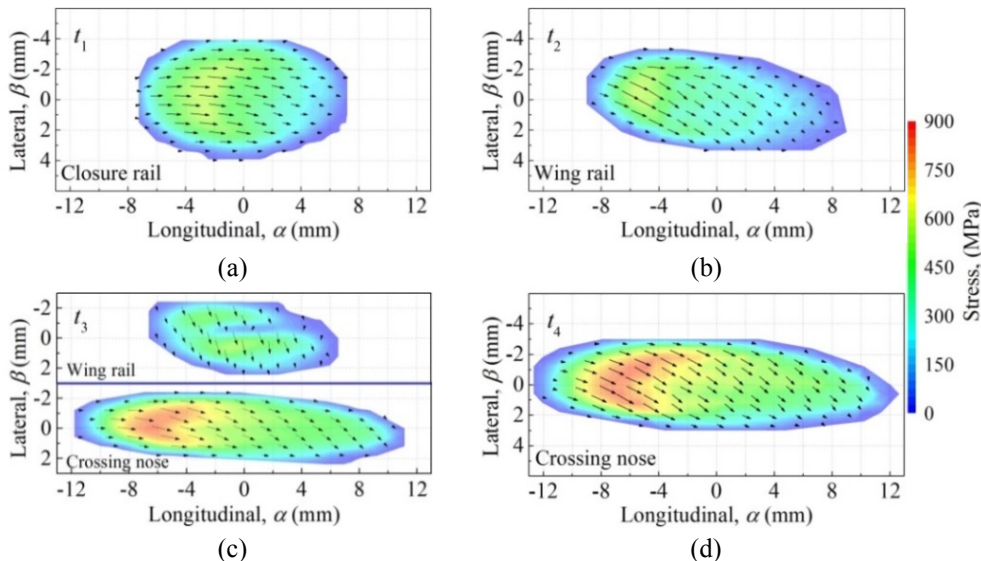


Figure 2.9: Field of surface shear traction

During the two-point contact, the shear traction vectors on the wing rail turned further clockwise (Figure 2.9(c)) to almost the lateral direction by t_3 . The change in direction can be explained by the distribution of the frictional force during the two-point contact, as shown in Figure 2.10(a). The longitudinal contact force on the wing rail decreased quickly to zero once the two-point contact occurred, whereas the decrease in the lateral contact force on the wing rail started later. The lateral contact force on the wing rail therefore remained, and the lateral shear traction on the wing rail in Figure 2.9(c) became dominant. The lateral contact force on the wing rail took longer to disappear, because the lateral creepage raised as a result of the misalignment between the longitudinal axis of the wing rail and the rolling direction of the wheel, as mentioned above.

Between t_3 and t_4 , the contact force on the wing rail quickly decreased to zero, and the crossing nose turned to solely take over the wheel load. The lateral contact force on the crossing nose consisted of three constituents. The first was the lateral component of the wheel load, pointed towards the wheel flange. The other two were lateral creep forces pointing to the field side of the wheel. One of these was from geometric spin, and its value was determined by the contact angle; the other was attributed to the misalignment between the trajectory of the contact patch and the moving direction of the wheel (see Figure 2.10(b)). In the current case, the latter constituent was dominant. In practice, such a high lateral creep force combined with the impact loading could cause the large plastic flow and cracks. At t_4 , both two-point contact and the misalignment of the wing rail disappeared, as did their contribution to the lateral shear traction. However, the misalignment caused by the widening of the crossing nose still persisted. In brief, the lateral shear traction in Figure 2.9(d) was mainly because of the misalignment, and to a lesser extent to the contact angle.

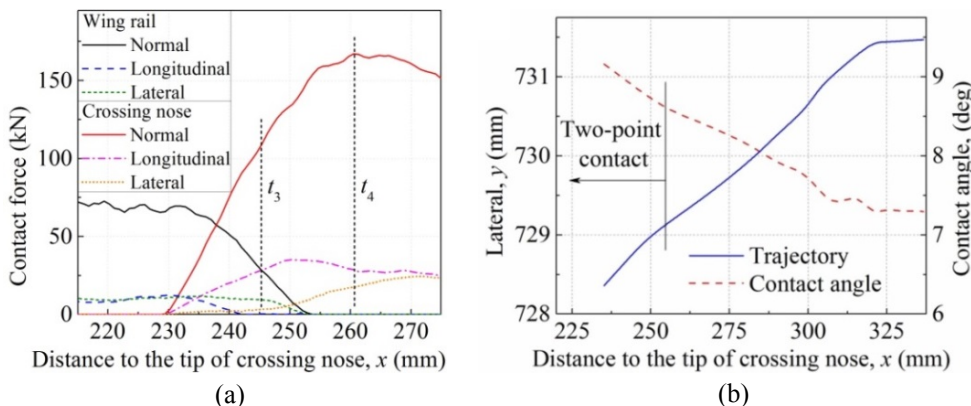


Figure 2.10: Tangent contact solution. (a) Time series of contact forces during the transition and (b) trajectory and contact angle of the centre of the contact patch.

As shown in Figure 2.10(a), the variations in the normal, longitudinal, and lateral contact forces were out-of-sync. On one hand, both the normal and lateral forces on the crossing nose rose from t_3 to t_4 , whereas the longitudinal force decreased. On the other hand, the decrease in the normal and lateral forces on the wing rail took more time than that of the longitudinal force. The normal, longitudinal, and lateral forces all reached their maxima between 0.25 and 0.27 m, whereas the crossing nose was still much narrower than the UIC54 profile (Figure 2.7(c) and (d)) and had a lower bearing capacity. It is reasonable to expect this region to be

vulnerable to damage. The out-of-sync dynamic forces exert the non-proportional loading in the materials and may significantly influence the initiation and growth of RCF [28]. These out-of-sync peak forces arise from the combination of the geometry and structure of the crossing panel, the misalignment of the wing rail and crossing nose, and the change in the contact angle. It is possible to optimize the geometry and structure of the crossing panel so as to minimize the forces during the impact, which will not only improve the ride quality of vehicles, but will also decrease the contact stresses and related damages.

Figure 2.11 shows the distribution of shear traction along the local longitudinal axis. Note that, because of the complex contact geometry, the maximum pressure and shear traction at each instant may not locate at the same local longitudinal axis. For illustration purposes, the local lateral coordinates of the axes as well as the traction bound, which is the pressure multiplied by the friction coefficient, are given. As can be seen, the peaks in the shear traction at all the selected instants occurred in the rear half of the contact patches. The pressure on the closure rail reached a maximum of 1317.6 MPa at t_1 and increased by 33% at t_2 , followed by a decrease as soon as the two-point contact occurred, whereas the maximum surface shear traction decreased by 11% from t_1 to t_3 . The maximum stresses were significantly higher on the crossing nose than on the closure/wing rail. A 75% increase in the pressure and a 39% increase in the surface shear traction were observed from t_1 to t_4 .

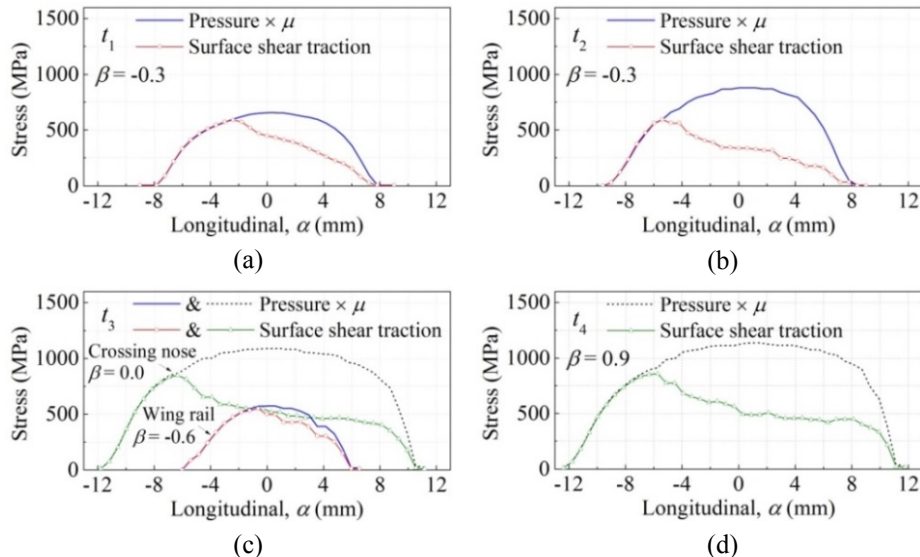


Figure 2.11: Distribution of surface shear traction along local longitudinal axis

2.4.4 MICRO-SLIP

Figure 2.12 shows the field of micro-slip during the transition. There was no micro-slip in the adhesion regions. The micro-slip in the slip regions was in an opposite direction to that of the surface shear traction, and the maximum micro-slip occurred around the trailing edge of the contact patch. The magnitudes of the micro-slip, indicated by color, increased progressively during the transition, with the maximum value increasing by 84% from t_1 to t_4 . It can be seen from Figure 2.12(c) and (d) that the distributions of the micro-slip at t_3 and t_4 were

not as regular as those in the earlier instants. This is because dynamic interactions between solids, especially during impact, inherently contain high frequency vibrations and waves. The vibrations and waves cause loading and unloading at local areas of the contact patch, resulting in a local change in the magnitude of micro-slip. The effect of this loading and unloading on the distribution of micro-slip became significant at t_3 and t_4 because of the impact.

2

As shown in Figures 2.10 and 2.12, both shear traction and micro-slip grew in magnitude during the impact, with a 39% increase in the maximum shear traction and an 84% increase in the maximum micro-slip from t_1 to t_4 . The combination of high micro-slip with high shear traction can produce high frictional power, speeding up the degradation of crossings.

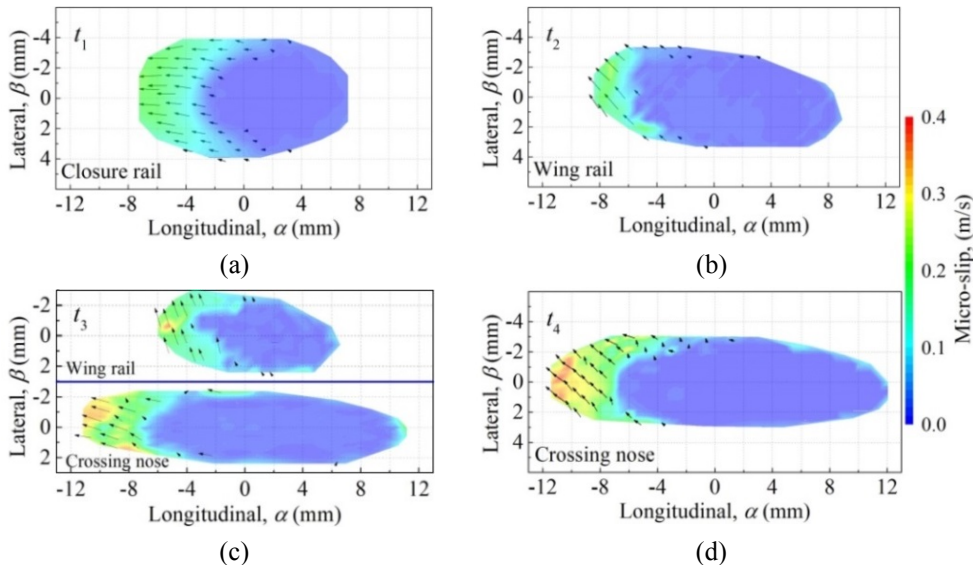


Figure 2.12: Field of micro-slip

2.5 CROSSING DEGRADATION DUE TO THE IMPACT

In this section, the degradation of the crossing nose by plastic deformation and frictional work [29, 30] during the impact is discussed, and the relationship between the trajectory of the contact patch and the degradation of the crossing nose is analysed.

2.5.1 PLASTIC DEFORMATION

The von Mises yield criterion was employed to calculate the plastic deformation. Figure 2.13(a) shows the distribution of the maximum von Mises stress along the longitudinal axis of the crossing nose. As can be seen, there was no plastic deformation in the initial stage of the two-point contact because of the small loads. As the load in the material exceeded the yield strength, plastic deformation grew quickly. Here, plastic deformation of the crossing nose distributed in the range of 230-330 mm from the tip of the crossing nose. The maximum von Mises stress of 1279 MPa occurred during two-point contact. After this, the value of von Mises stress decreased monotonically. At t_4 , the value was 1265 MPa, a drop of 1.1% from the maximum value.

Figure 2.13(b) shows the trajectories of the maximum von Mises stress as well as the centre of the contact patch. In general, the two trajectories were close to each other. The difference between the two trajectories can be mainly attributed to the complex contact geometry and the non-proportional loading conditions. Because the crossing nose widened along the longitudinal direction, the trajectory of the contact patch misaligned with the rolling direction of the wheelset, leading to large lateral creep forces. The lateral coordinate of the maximum von Mises stress increased with the movement of the wheel until the crossing nose profile evolved into the standard UIC54 type.

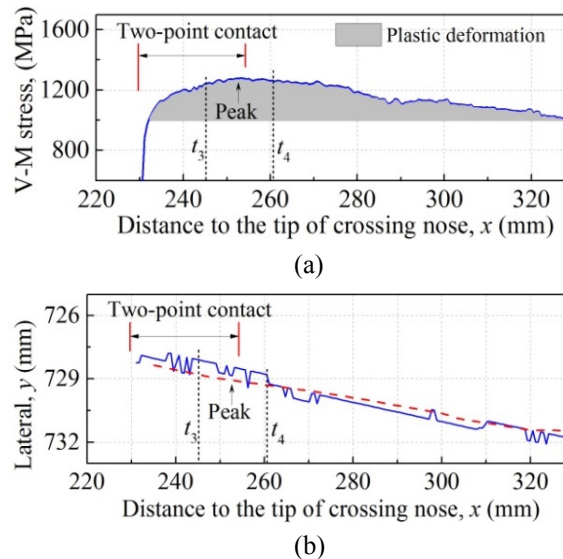


Figure 2.13: Plastic deformation of the crossing nose. (a) Maximum von Mises stress along the longitudinal direction and (b) trajectories for (—) the maximum von Mises stress and (--) the centre of the contact patch.

2.5.2 FRICTIONAL WORK

Figure 2.14(a) shows the distribution of the maximum frictional work along the longitudinal axis of the crossing nose. As can be seen, the maximum frictional work grew rapidly while the wheel was in touch with the crossing nose, reaching a peak of $2.85 \times 10^4 \text{ J/m}^2$ shortly after t_3 . The maximum frictional work occurred at approximately the same time. At t_4 , when the normal contact force reached its peak, the frictional work dropped to $2.21 \times 10^4 \text{ J/m}^2$, or 22.5% of the maximum value. Thereafter, the maximum frictional work fluctuated downwards, eventually stabilizing at around $0.56 \times 10^4 \text{ J/m}^2$.

Figure 2.14(b) compares the trajectories of the maximum frictional work and the centre of the contact patch during the impact. The maximum frictional work occurred around the centre of the contact patch with some fluctuations. Similar fluctuations can be observed in Figure 2.13(b), but are more frequent in Figure 2.14(b). Because frictional work is the product of shear traction and micro-slip [26] and reflects their non-smoothness (see Figures 2.10 and 2.12), the distribution of frictional work is not as smooth as that for plastic deformation.

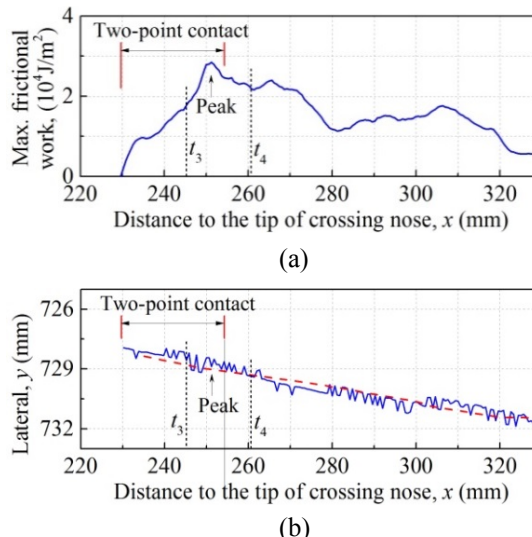


Figure 2.14: Frictional work on the crossing nose. (a) Maximum along the longitudinal direction and (b) trajectories for (—) the maximum frictional work and (---) the centre of the contact patch.

2.6 DISCUSSION

- **Non-proportional loading and crossing degradation**

In Section 2.5, it was noted that the maximum values for both plastic deformation and frictional work appeared during two-point contact rather than at the moment of maximum normal contact force. The degradation of the crossing can therefore be attributed to the combined effect of the normal, longitudinal, and lateral contact forces. Their non-proportionality should be taken into account [28]. This highlights the necessity for detailed analysis of stress and strain during the impact, to develop an insightful understanding of the initiation and growth of crossing degradation.

In this chapter, we have demonstrated the capacity of the FE model to analyse the plastic deformation and frictional work of the crossing nose. Regarding degradation such as RCF, the contact solution obtained from the FE model can also provide accurate input for damage prediction [31-34].

The analysis of crossing degradation presented in Section 2.5 is based on a single wheelset passage, and the effect of material hardening under cyclic loading was not considered. In future work, the performance of crossing panel in terms of RCF resistance under cyclic loading will be studied. This will be done by simulating multiple wheel passages and then estimating the crossing degradation over a long term.

- **Application of anomaly detection at crossings**

The present work has established a correlation between measured and simulated ABA signals. The FE model can be further employed to reproduce the ABA signal in the presence of track structural anomalies and to extract the signature waveform of ABA signal, which should allow anomalies at the crossing panel to be detected.

2.7 SUMMARY

In this chapter, the wheel-rail impact at crossing was investigated using a FE model. The model was first verified by comparing the simulated axle box acceleration with in situ measurements in terms of the major frequency contents, wavelet power, and impact position. Special attention was paid to reliable contact solutions that help extend our understanding of crossing degradation. The contact solution took account of not only the dynamic contact force, but also the distribution of adhesion-slip regions, pressure, shear traction and micro-slip. The contact solution was then used to calculate the plastic deformation and frictional work of the crossing nose during one wheelset passage. The following conclusions are drawn:

- The variations of normal and tangential contact forces on both wing rail and crossing nose are out-of-sync during the impact. This can lead to non-proportional loading in the materials and should be taken into account in damage analysis.
- The longitudinal axis of the wing rail is misaligned with the wheelset rolling direction. The widening of the crossing nose also causes misalignment between the wheelset rolling direction and the trajectory of the contact patch. As a consequence, the value of lateral creepage rises.
- At the two-point contact stage, the decrease in the lateral contact force on the wing rail is slower than that of the longitudinal contact force, and the vectors of shear traction and micro-slip on the wing rail therefore point almost towards the lateral direction. After the two-point contact, the longitudinal contact force on the crossing nose begins to decrease, whereas the increase in the lateral contact force speeds up.
- By optimizing the geometry and the structural design of the crossing panel, it is possible to minimize the forces and therefore the degradation. The relationship between the plastic deformation, the frictional work, the geometry, and the structure can be used for the optimization and performance prediction.
- The locations of the maximum values along the crossing nose do not coincide with the moving trajectory of the contact patch because of the complex contact geometry and the non-proportional loading condition.
- Under the assumption of nominal contact geometry and facing through motion of vehicles with the loading conditions studied, the maximum values of both the effective plastic deformation and the frictional work of the crossing nose occur during the two-point contact transition from the wing rail to the crossing nose rather than, as widely believed, at the moment of maximum normal contact force. For other scenarios such as degraded contact profiles and divergent motion of vehicles, more experimental and numerical works are required in further study, in an effort to obtain a more comprehensive understanding of the behaviour of dynamic wheel-rail interaction and the related failures at crossings.

REFERENCES

- [1] ProRail, *Jaarverslag* (Utrecht, Netherland, 2015), pp. 127.
- [2] I. Shevtsov, Rolling contact fatigue problems at railway turnouts – experience of ProRail, in *Materials Under Combined Durability Conditions* (Lochristi, Belgium, 2013), pp. 20.

2

- [3] C. Andersson, T. Dahlberg, *Wheel/rail impacts at a railway turnout crossing*, Proceedings of the Institution of Mechanical Engineers, Part F: Journal of Rail and Rapid Transit **212**, 123-134 (1998).
- [4] E. Kassa, J.C. Nielsen, *Dynamic train–turnout interaction in an extended frequency range using a detailed model of track dynamics*, Journal of Sound and Vibration **320**, 893-914 (2009).
- [5] S. Alfi, S. Bruni, *Mathematical modelling of train–turnout interaction*, Vehicle System Dynamics **47**, 551-574 (2009).
- [6] S. Bruni, I. Anastasopoulos, S. Alfi, A. Van Leuven, G. Gazetas, *Effects of train impacts on urban turnouts: Modelling and validation through measurements*, Journal of Sound and Vibration **324**, 666-689 (2009).
- [7] B.A. Pålsson, J.C. Nielsen, *Wheel–rail interaction and damage in switches and crossings*, Vehicle System Dynamics **50**, 43-58 (2012).
- [8] Y.Q. Sun, C. Cole, M. McClanahan, *The calculation of wheel impact force due to the interaction between vehicle and a turnout*, Proceedings of the Institution of Mechanical Engineers, Part F: Journal of Rail and Rapid Transit **224**, 391-403 (2010).
- [9] R.F. Lagos, A. Alonso, J. Vinolas, X. Pérez, *Rail vehicle passing through a turnout: Analysis of different turnout designs and wheel profiles*, Proceedings of the Institution of Mechanical Engineers, Part F: Journal of Rail and Rapid Transit **226**, 587-602 (2012).
- [10] V.L. Markine, M.J.M.M. Steenbergen, I.Y. Shevtsov, *Combatting RCF on switch points by tuning elastic track properties*, Wear **271**, 158-167 (2011).
- [11] D. Nicklisch, E. Kassa, J. Nielsen, M. Ekh, S. Iwnicki, *Geometry and stiffness optimization for switches and crossings, and simulation of material degradation*, Proceedings of the Institution of Mechanical Engineers, Part F: Journal of Rail and Rapid Transit **224**, 279-292 (2010).
- [12] A. Johansson, B. Pålsson, M. Ekh, J.C. Nielsen, M.K. Ander, J. Brouzoulis, E. Kassa, *Simulation of wheel–rail contact and damage in switches & crossings*, Wear **271**, 472-481 (2011).
- [13] Z. Li, X. Zhao, C. Esveld, R. Dollevoet, M. Molodova, *An investigation into the causes of squats—Correlation analysis and numerical modeling*, Wear **265**, 1349-1355 (2008).
- [14] M. Wiest, W. Daves, F. Fischer, H. Ossberger, *Deformation and damage of a crossing nose due to wheel passages*, Wear **265**, 1431-1438 (2008).
- [15] M. Pletz, W. Daves, W. Yao, H. Ossberger, *Rolling contact fatigue of three crossing nose materials—multiscale FE approach*, Wear **314**, 69-77 (2014).
- [16] M. Pletz, W. Daves, H. Ossberger, *A wheel set/crossing model regarding impact, sliding and deformation-Explicit finite element approach*, Wear **294**, 446-456 (2012).
- [17] P. Westeon, C. Ling, C. Roberts, C. Goodman, P. Li, R. Goodall, *Monitoring vertical track irregularity from in-service railway vehicles*, Proceedings of the institution of mechanical engineers, Part F: Journal of Rail and Rapid Transit **221**, 75-88 (2007).
- [18] J.S. Lee, S. Choi, S.-S. Kim, C. Park, Y.G. Kim, *A mixed filtering approach for track condition monitoring using accelerometers on the axle box and bogie*, IEEE Transactions on Instrumentation and Measurement **61**, 749-758 (2012).

[19] M. Molodova, Z. Li, A. Núñez, R. Dollevoet, *Automatic detection of squats in railway infrastructure*, IEEE Transactions on Intelligent Transportation Systems **15**, 1980-1990 (2014).

[20] M. Molodova, Z. Li, R. Dollevoet, *Axle box acceleration: Measurement and simulation for detection of short track defects*, Wear **271**, 349-356 (2011).

[21] M. Oregui, Z. Li, R. Dollevoet, *An investigation into the modeling of railway fastening*, International Journal of Mechanical Sciences **92**, 1-11 (2015).

[22] Z. Ren, S. Sun, W. Zhai, *Study on lateral dynamic characteristics of vehicle/turnout system*, Vehicle System Dynamics **43**, 285-303 (2005).

[23] X. Zhao, Z. Li, *The solution of frictional wheel-rail rolling contact with a 3D transient finite element model: Validation and error analysis*, Wear **271**, 444-452 (2011).

[24] Z. Wei, Z. Li, Z. Qian, R. Chen, R. Dollevoet, *3D FE modelling and validation of frictional contact with partial slip in compression-shift-rolling evolution*, International Journal of Rail Transportation **4**, 20-36 (2016).

[25] L. Chang, R. Dollevoet, R. Hanssen, *Railway infrastructure monitoring using satellite radar data*, International Journal of Railway Technology **3**, 79-91 (2014).

[26] X. Zhao, Z. Wen, M. Zhu, X. Jin, *A study on high-speed rolling contact between a wheel and a contaminated rail*, Vehicle System Dynamics **52**, 1270-1287 (2014).

[27] C. Torrence, G.P. Compo, *A practical guide to wavelet analysis*, Bulletin of the American Meteorological Society **79**, 61-78 (1998).

[28] Y. Liu, L. Liu, S. Mahadevan, *Analysis of subsurface crack propagation under rolling contact loading in railroad wheels using FEM*, Engineering fracture mechanics **74**, 2659-2674 (2007).

[29] J. Archard, *Contact and rubbing of flat surfaces*, Journal of applied physics **24**, 981-988 (1953).

[30] C. Rodkiewicz, Y. Wang, *A dry wear model based on energy considerations*, Tribology International **27**, 145-151 (1994).

[31] B. Dirks, R. Enblom, *Prediction model for wheel profile wear and rolling contact fatigue*, Wear **271**, 210-217 (2011).

[32] S. Bogdański, P. Lewicki, *3D model of liquid entrapment mechanism for rolling contact fatigue cracks in rails*, Wear **265**, 1356-1362 (2008).

[33] J. Santamaría, E. Vadillo, O. Oyarzabal, *Wheel-rail wear index prediction considering multiple contact patches*, Wear **267**, 1100-1104 (2009).

[34] D. Fletcher, L. Smith, A. Kapoor, *Rail rolling contact fatigue dependence on friction, predicted using fracture mechanics with a three-dimensional boundary element model*, Engineering Fracture Mechanics **76**, 2612-2625 (2009).

3

EVALUATING THE PERFORMANCE OF LONG-TIME SERVICED CROSSING RAILS

In this chapter, a method capable of evaluating the performance of long-term serviced crossing rails is proposed. The method composes of 1) in-situ 3D profile and hardness measurements serving as input, 2) FE simulation of wheel-rail interaction for analysing contact behaviour and 3) numerical prediction of rail degradation due to wear and plastic deformation. To demonstrate the method, a case study was conducted on a crossing which had serviced in the Dutch railway for a long-term. The case study indicates that the crossing experienced a run-in process in the major traffic direction, manifested as the widening of running band, the enlargement of contact patch size and thus the decrease of contact stresses, plastic deformation and wear. However, the wheel-rail interaction exacerbates in the minor traffic direction, coming with narrower running band, smaller contact patch size and larger contact stresses, eventually inducing severer plastic deformation and wear. With the aid of the method, preventive maintenance can be timely conducted and the service life of crossing can be extended.

This chapter is based on:

Wei Z, Núñez A, Boogaard A, Dollevoet R, Li Z. Method for evaluating the performance of railway crossing rails after long-term service. *Tribology International* 123 (2018): 337-348.

3.1 INTRODUCTION

The major function of railway crossings is to provide the flexibility of railway operation, i.e., intersecting different tracks at the same level. Figure 3.1 shows the main components of a railway crossing. At a crossing, a geometric discontinuity (i.e. a gap) is made by design between the wing rail and the crossing nose. Consequently, high wheel-rail contact forces and undesired vibrations arise during the passage of vehicles over the discontinuity, so that crossings degrade much faster than ordinary plain tracks [1, 2].

3

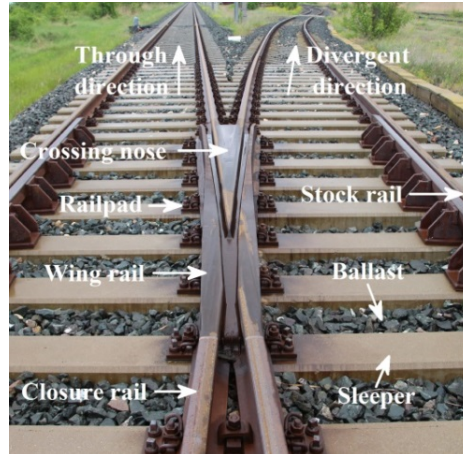


Figure 3.1: Main components of a railway crossing

During long-term service, crossing rails suffer from various types of degradations, e.g., RCF (such as head checks, spalling [3] and cracks [4]), accumulated plastic deformation and wear [5]. Crossings with severe RCF defects can be easily identified, so that corrective maintenance actions (e.g., grinding and welding [6]) can be timely conducted. For plenty of crossings without severe RCF defects, preventive maintenance is preferred but seldom taken even though their profiles have degraded significantly. On long-term serviced crossings, the wheel-rail contact behaviour may differ largely from the nominal state, increasing the risk of rail sudden failure and even train derailment. A better understanding on the performance of long-term serviced crossings due to traffic loads is beneficial to timely conduct preventive maintenance and extend their service life.

The dynamic wheel-crossing interaction can be analysed using MBD method, FE method and the combination of them. In the MBD model, the vehicle and track components are simplified as a combination of rigid or flexible bodies, springs and dampers [7-14]. The MBD method requires a limited number of degree of freedom, so that the computation procedure is fast. The MBD method is adept at analysing the long-distance vehicle-track interaction to assess the stability and ride quality of vehicles. For the wheel-rail contact model, the normal and tangent problems are solved independently [15-17], i.e., the (semi- or multi-) Hertz springs for the normal contact while usually the FASTSIM [18] for the tangent contact. These contact algorithms are restricted to the assumptions of half-space, linear elastic and steady state, so that their application at crossings is challenged by complex contact geometry (e.g., conformal contact and large variation of the contact angle [19-22]), nonlinear material

property and transient wheel/rail interaction [23].

To overcome the limitation of the MBD method in analysing the nonlinear material and complex contact geometry, Nicklisch *et al.* [24] developed an approach by combining the MBD with the FE methods. In the approach, a MBD model was used to simulate the vehicle dynamics and provide the input (e.g., contact force and contact position) for the FE modelling of rail degradation. A similar approach was also proposed in [25].

With the rapid development of computation power, the explicit FE method provides an alternative way for analysing the dynamic wheel-rail interaction. The main advantage of the explicit FE method is that realistic adhesion-slip state in the contact patch can be obtained, as the non-differentiability of the Coulomb's law [26] occurring in the implicit FE method is avoided in a physical way [27].

Pletz *et al.* [28, 29] developed an explicit FE model to simulate the dynamic wheel-crossing interaction. In their model, a wheel with a constant load on the axle moves over a short piece of crossing rails (with the length of 3 m) suspended on a Winkler foundation. This model was further improved by Xin *et al.* [30] through extending the dimension of the crossing model and including the missing components (e.g., railpad and sleeper). The preceding two FE wheel/crossing models focus on the normal contact behaviour, whereas the tangent contact parameters (e.g., adhesion-slip state and shear traction) are missing, so that they cannot accommodate satisfactory accuracy when analysing rail degradation. In chapter 2, an explicit FE model is presented to elaborate the evolution of wheel/crossing contact (in terms of contact patch, adhesion-slip state, contact stresses and micro-slip), and the simulated dynamic response (i.e., major frequencies and energy distributions of axle box acceleration) is verified via field ABA measurements. Yet, the FE model was only demonstrated at the nominal condition, i.e., with nominal rail geometry and material property, while the wheel/crossing contact behaviour at various degraded conditions (with the presence of deformed crossing profiles and non-identical material properties) still remains unclear. To fill the gap, this chapter integrates the FE model with other experimental and numerical approaches to analyse the dynamic wheel/rail interaction at long-term serviced crossings. This information is expected to provide a guideline for conducting preventive maintenance and to extend the service life of crossings.

To model the degraded rails with actual geometry, precise profile measurement is required. In the literature, the crossing rails were most commonly measured in 2D [5, 6, 25, 31]. The 2D measurements suffer from the following challenges. First, it is taken at each cross-section and is time-consuming when measuring numerous cross-sections. Therefore, a large spacing is often specified between adjacent cross-sections (e.g., 50-300 mm [6, 25, 31]), and the rail defects with short length may be missed or incompletely measured. Second, it is difficult to accurately correlate all of the separately measured cross-sections in the same coordinate, so that numerical errors may be introduced in the numerical modelling. In this study, the crossing rails will be measured in 3D, so that the crossing profiles can be fully captured in one measurement.

In this chapter, a method is proposed to evaluate the performance of long-term serviced crossings. In the method, the 3D profiles and hardness of crossing rails are measured to provide the input for the FE modelling of dynamic wheel-rail interaction, while the simulated contact behaviour is used to predict the rail degradation due to wear and plastic deformation. The structure of this study is arranged as follows. Section 3.2 describes the evaluating method,

including in-situ measurements and numerical simulations. Section 3.3 conducts a case study on a long-term serviced crossing in the Dutch railway. Finally, Section 3.4 draws the main conclusions.

3.2 EVALUATION PROCEDURE

In this section, the evaluation procedure of the method is described. The method composes of 1) in-situ 3D profile and hardness measurements serving as input, 2) FE modelling of wheel-rail interaction for analysing contact behaviour and 3) numerical prediction of rail degradation due to wear and plastic deformation. Figure 3.2 shows the flowchart of the evaluation method.

3.2.1 IN-SITU MEASUREMENTS

During long-term service, both the profile and the material behaviour of crossing rails can degrade compared to the nominal condition. These degradations can be captured by 3D profile and hardness measurements.

The 3D rail profiles are measured using the non-contact apparatus HandyScan. In the measurement, laser stripes are projected on the rail surfaces, while two cameras capture the reflected projections to extract the 3D data. The accuracy of the HandyScan device can be up to 0.03 mm in arbitrary directions, which is sufficient to capture slight changes of crossing profiles. Figure 3.2 shows an example of a measured crossing profile.

The hardness measurement is conducted on the surfaces of crossing rails. Because the crossing rails may experience non-uniform hardening process between the through and divergent directions, the rail hardness will be measured along both directions. In this study, the hardness serves as the input for the FE simulation of wheel/rail interaction and the prediction of rail degradation. In the simulation, the hardness H can be converted to yield strength σ_y using the following equation [32]

$$\sigma_y = H/3 \times (0.1)^m \quad (3.1)$$

where m is the hardness coefficient.

3.2.2 FE MODELLING OF WHEEL-RAIL INTERACTION

The dynamic wheel/rail interaction on the long-term serviced crossing is simulated using the commercial software ANSYS/LS-DYNA. In the FE model, the rails and sleepers are modelled with solid elements, while the railpads and ballast are modelled as linear springs and viscous dampers. The wheelset is modelled with solid elements, and the car body and bogie are simplified as lumped mass and supported on the wheel axle by linear springs and viscous dampers. The parameters of the vehicle and track components will be described in the case study of Section 3.3.2.

As the wheelset moves over the crossing, one wheel runs along the closure rail, the wing rail and then across the gap, impacting on the crossing nose, see Figure 3.1. The other wheel moves along the stock rail. The calculating procedure is as follows: 1) the static equilibrium of the wheelset standing still on the crossing is computed using the implicit solver of ANSYS; 2) the dynamic wheel-rail interaction is simulated using the explicit solver of LS-DYNA to

obtain the kinematic and dynamic results such as nodal displacement and force. Thereafter, the contact parameters in terms of contact patch, adhesion-slip state, shear traction and micro-slip can be extracted.

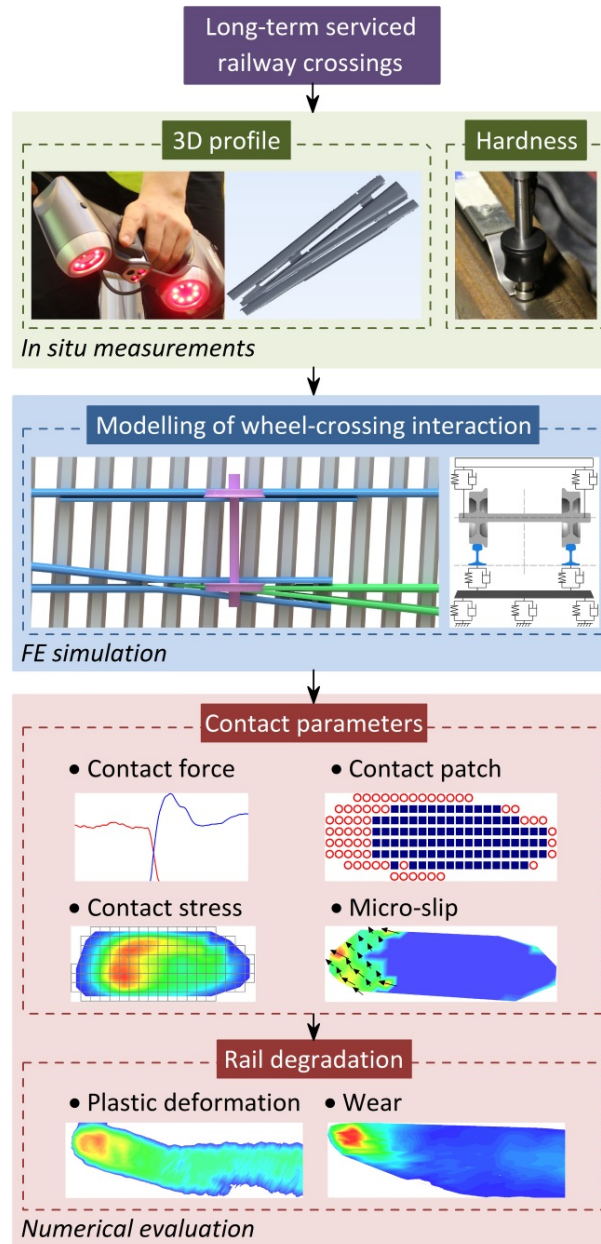


Figure 3.2: Flowchart of the evaluating method

3.2.3 PREDICTION OF RAIL DEGRADATION

The wheel-rail contact parameters obtained from the FE model are used to predict the rail degradation due to wear and plastic deformation. Wear is the removal of material from the wheel/rail interface. In the literature, the frictional work method and the sliding method are commonly used to analyse the distribution of wear. In the frictional work method, the material loss depends on the energy dissipation [33-35], i.e., the work generated at the wheel/rail interface. For long-term serviced crossings, the rails may experience non-identical hardening process at different regions, which can affect the distribution of wear. As the frictional work method does not directly include the influence of non-identical hardening on wear, the sliding method is considered in this study. The sliding method was initially proposed by Archard [36], where the wear volume V_{wear} is expressed as

$$V_{wear} = k_s \frac{F_n d}{H} \quad (3.2)$$

where F_n is the normal force, d is the sliding distance and H is the material hardness. k_s is the wear coefficient and can be obtained from the wear chart [37], see Figure 3.3.

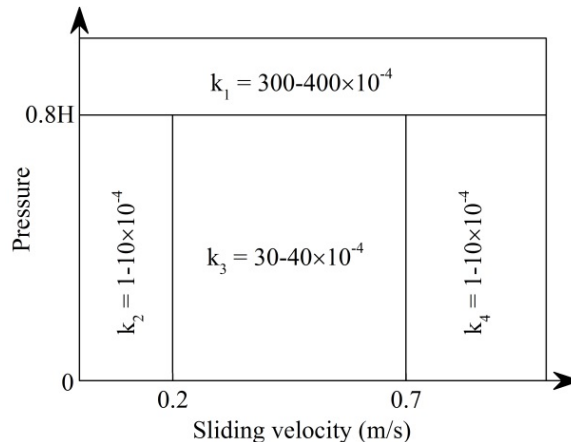


Figure 3.3: Wear coefficient of Archard's model at dry condition [37]

At a node of the rail surface, the wear depth can then be calculated by [14]

$$\Delta z = \frac{k_s}{H} \int_0^T p s dt = \frac{k_s}{H} \sum_{i=1}^n p_i s_i \Delta T \quad (3.3)$$

where p is the pressure and s is the sliding velocity. ΔT is the time step for output, T is the duration of wheel-rail contact at the node and equal to $n\Delta T$.

Plastic deformation originates from high contact stresses, it occurs when the stresses in the material exceed a threshold value. In this chapter, the von Mises yield criterion will be used to evaluate the plastic deformation, which is expressed as

$$\sigma_v = \sqrt{\frac{1}{2} \left[(\sigma_{xx} - \sigma_{yy})^2 + (\sigma_{yy} - \sigma_{zz})^2 + (\sigma_{zz} - \sigma_{xx})^2 + 6(\sigma_{xy}^2 + \sigma_{yz}^2 + \sigma_{zx}^2) \right]} \quad (3.4)$$

where σ_{xx} , σ_{yy} and σ_{zz} are the normal stress and σ_{xy} , σ_{yz} and σ_{zx} are the shear traction.

3.3 CASE STUDY

To demonstrate the method proposed in Section 3.2, a case study was carried out on a long-term serviced crossing in the Dutch railway, see Figure 3.4. The crossing is a 54E1-1:9 type, with the UIC54 rail profile and a crossing angle of 1:9. The crossing rails are made of the R260Mn rail material. During its long-term service, the crossing profile had changed significantly compared to the nominal condition, whereas no severe RCF defects can be observed. According to statistics, 87% of the total traffic loads was in the through moving direction (Figure 3.1) while the rest occurred in the divergent direction. In both directions, the train operational speed is limited to 40km/h.

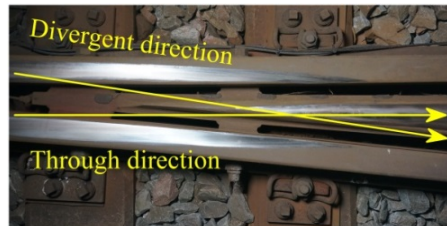


Figure 3.4: A long-term serviced crossing for case study

3.3.1 STEP 1: MEASURING THE DEGRADATION STATUS

3D profile and hardness measurements were conducted on the long-term serviced crossing. Figure 3.5 shows the measured 3D crossing profile from top view. In the profile measurement, a three-dimensional Cartesian coordinate system is adopted, with the origin o at the tip of the crossing nose, with the x , y and z axes oriented in the longitudinal, lateral and vertical directions of the through moving direction. The measured 3D crossing profile is composed of triangles (Figure 3.5), and the vertexes of these triangles are the measured data points.

In Figure 3.5, 12 cross-sections are selected to gain an insight into the profile change between nominal state and that after long-term service. Cross-sections W1 and W5 are along the centrelines of the wing rail, cross-section N1 is along the centrelines of the crossing nose, while cross-sections W2-W4, W6-W8 and N2-N4 are perpendicular to the x axis.

Figure 3.6 compares the crossing profile at nominal state and after long-term service. Along the centrelines of the wing rail, the height difference between the two states reaches the maxima of 0.5 mm at W1 and 0.8 mm at W5, respectively. Due to the misalignment between the rolling direction of the wheelset and the centrelines of the wing rail (W1 and W5), the running band on the wing rail shrinks laterally toward the gauge side, as indicated by the shiny running band in Figure 3.4. Consequently, no profile change can take place from $x=257$ mm on along W1 and from $x=304$ mm on along W5.

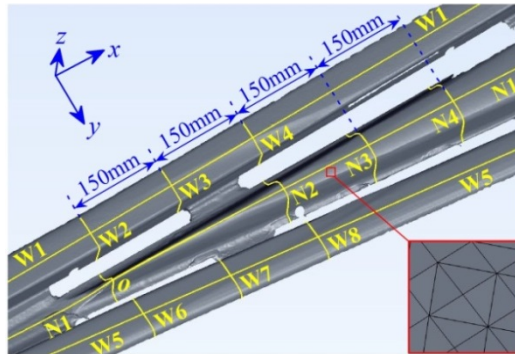


Figure 3.5: Measured 3D crossing profile with a close-up of data points. Cross-sections W1 and W5 are along the centrelines of wing rail, N1 is along the centreline of crossing nose, while W2-W4, W6-W8 and N2-N4 are perpendicular to the x axis.

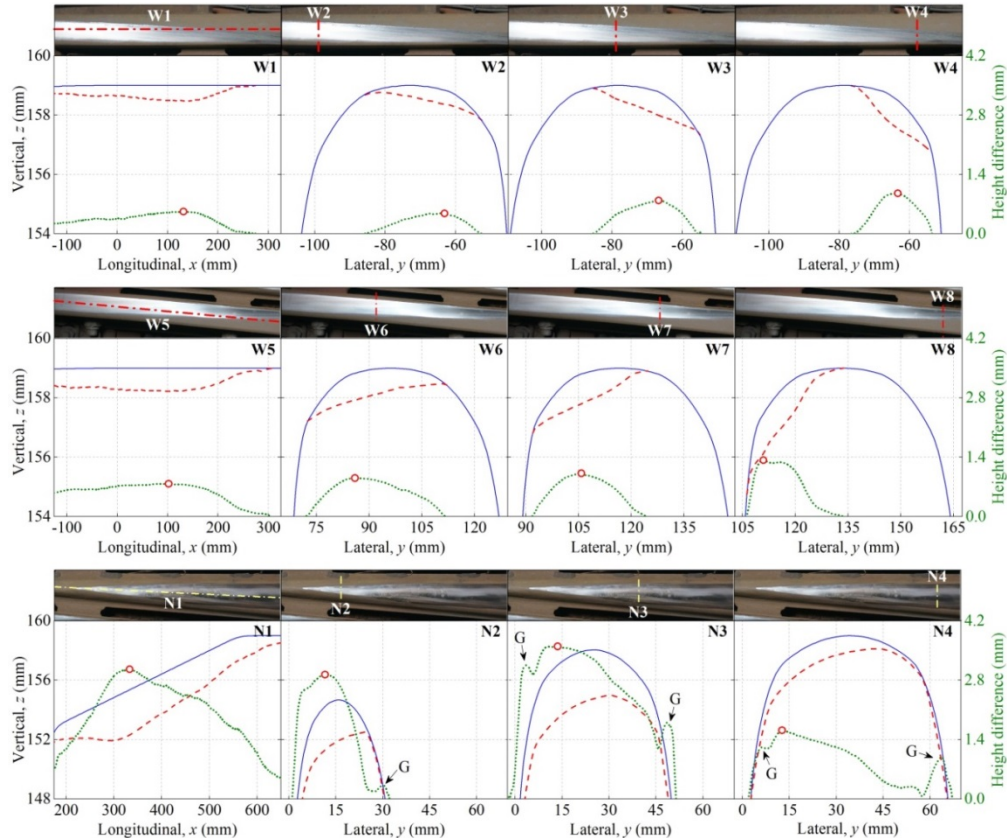


Figure 3.6: Comparison of crossing profile at nominal state and after long-time service. Line (—) indicates the profile at nominal state, line (---) the profile after long-term service and line (....) the height difference. Dot (○) indicates the maximum height difference. Arrow G denotes the profile change due to flange contact.

Regarding the lateral-vertical cross-sections of the wing rail, the maximal height difference increases from 0.5 mm (W2) to 0.8 mm (W3) and then to 1.0 mm (W4). Meanwhile, the distance between the maximal height difference and the centreline W1 increases from W2 to W4, as shown in the first row of Figure 3.6. Similar phenomena can also be observed in the second row of Figure 3.6, where the maximum height difference increases from 0.8 mm (W6) to 1.0 mm (W7) and then to 1.3 mm (W8). On the wing rail, the running band becomes narrower along the rolling direction; this exacerbates the profile change and moves the maximal height difference laterally away from the centrelines (W1 and W5) in an increasing manner.

On the crossing nose, the profile change is significantly larger than that on the wing rail. Along N1, the maximal height difference reaches 3.1 mm, which is approximately 3 times higher than that along W1 (0.8 mm). The maximum height difference at N2-N4 varies from 1.6 to 3.6 mm, while their locations move laterally away from the centreline N1, see the third row of Figure 3.6. Along N3 and N4, several small peaks in the height difference can be observed around the gauge corner, as denoted by arrows G. These peaks come with two-point contact, with the first contact occurring on the rail top and the second contact occurring at the gauge corner. The two-point contact can be either explicit or implicit (i.e., the second contact comes from the deformation at the first contact by wheel load, see Figure 6.7 in [20] and Figure 5 in [38]) depending on the contact geometry and the moving trajectory of the wheels.

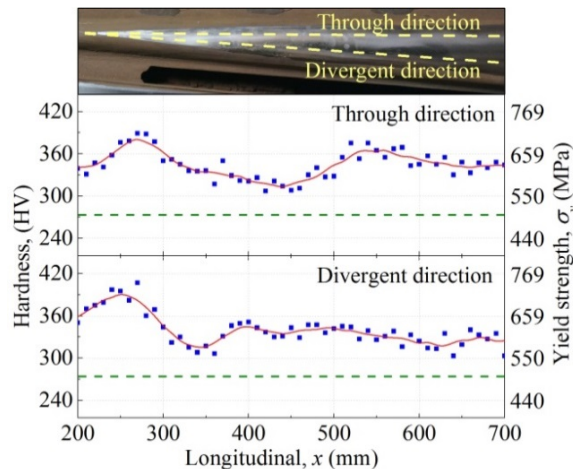


Figure 3.7: Hardness measured on the long-term serviced crossing. The rectangles (■) indicate the hardness measured every 10 mm along H1 and H2, the solid line (—) indicates the averaged hardness of every adjacent three points, the dashed lines (---) indicate the hardness of the nominal crossing rails.

Figure 3.7 shows the hardness measured on the long-term serviced crossing, which was measured every 10 mm along through and divergent directions. At $x=200-700$ mm, the hardness along through direction (Figure 3.7(a)) ranges from 302 HV to 389 HV, with the maximum occurring at $x=270$ mm. The hardness along divergent direction (Figure 3.7(b)) distributes between 303-407 HV, with the maximum also occurring at $x=270$ mm. The variation of the measured hardness should agree with the distribution of the wheel-rail contact stresses, which will be analysed in Sections 3.3.2 and 3.3.3.

In the FE modelling, the measured hardness is converted to yield strength using Equation (3.1). For the nominal R260Mn rail material, the typical hardness and yield strength are 274 HV and 500 MPa [37], so that the coefficient m in Equation (3.1) can be determined as -0.74. On the long-term serviced crossing, the yield strength of rails ranges between 553-712 MPa along through direction and between 555-746 MPa along divergent direction.

3.3.2 STEP 2: CHARACTERIZING WHEEL/RAIL CONTACT BEHAVIOR

This section simulates the passage of a wheelset over the long-term serviced crossing. The wheel profile is nominal S1002. The average axle load is 16.8 tons, while the stiffness and damping of the primary suspension are 880 kN/m and 4000 Ns/m [39]. A bilinear elastoplastic material model is used to account for the plastic deformation of contact bodies. The density, Young's modulus, Poisson's ratio and tangent modulus of the wheel and rail are 7800 kg/m³, 210 GPa, 0.3 and 21 GPa, respectively. The yield strength is converted from the measured hardness, see Figure 3.7. For the crossing, the stiffness and damping are 1560 MN/m and 67.5 kNs/m for a standard railpad, while the corresponding values of the ballast are 90 MN/m and 64 kNs/m for a standard concrete sleeper [40]. The sleepers are treated as linear elastic bodies, with the Young's modulus, density and Poisson's ratio being 38 GPa, 2480 kg/m³ and 0.2.

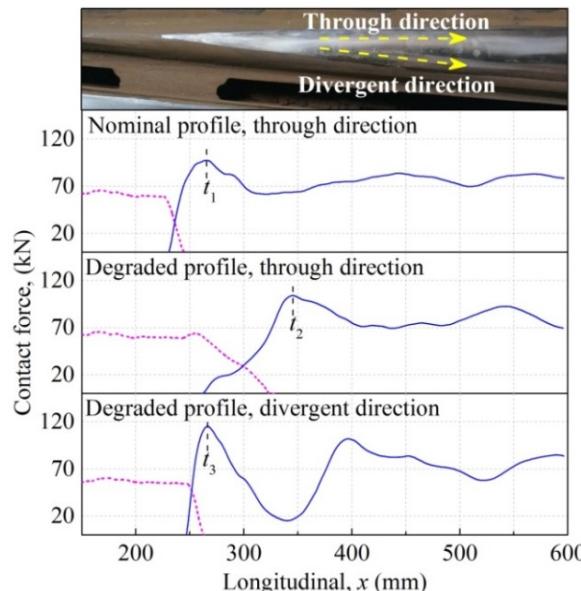


Figure 3.8: Distribution of normal contact force. t_1 , t_2 and t_3 indicate the instants with the maximum normal contact force. The solid lines (—) indicate the contact force on crossing nose, and the dashed lines (---) indicate the contact force on wing rail.

The frictional wheel-rail contact is defined by the Coulomb's law, with the frictional coefficient being 0.4 for dry condition [41]. At the wheel/rail interface, the minimum element size is set to 1×1 mm. In total, the FE model contains 478553 elements. In the explicit FE simulation, the output time step ΔT is set to 4×10^{-5} s, at which the wheelset translates 0.44 mm.

On the nominal crossing, the rail profiles are symmetric with respect to the centreline N1. On the long-term serviced crossing, however, the measured profiles are no longer symmetric (see Figure 3.6), resulting in different wheel-rail contact geometry between through and divergent moving directions. To account for the influence of asymmetric crossing profile on the wheel-rail contact behaviour, both the through and divergent motions of the wheelset are simulated. In both directions, the train speed is set to 40 km/h.

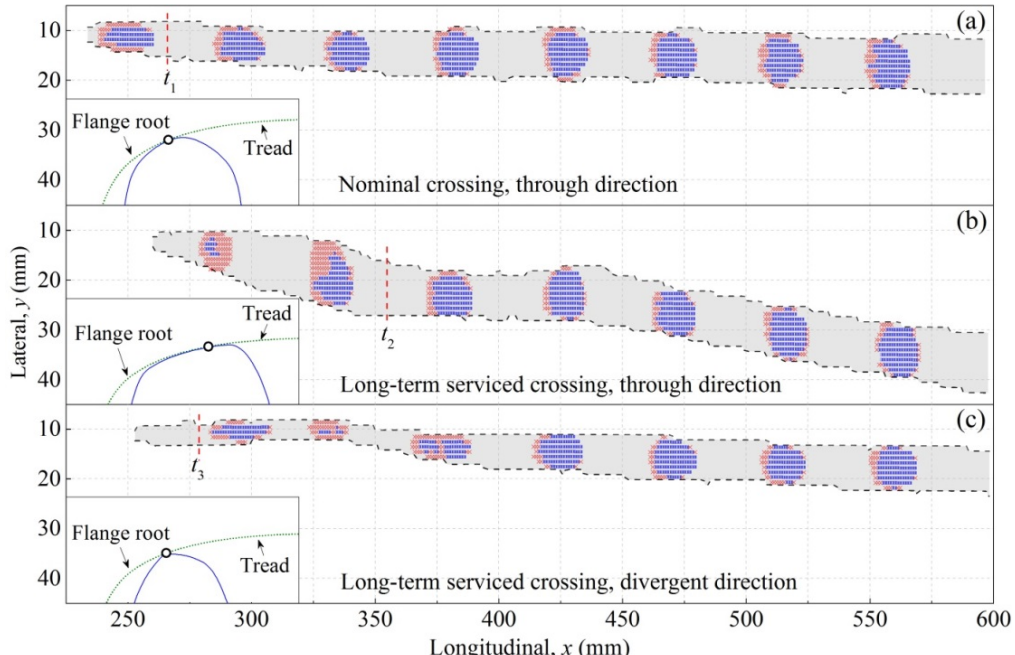


Figure 3.9: Distribution of the running band. The dashed line (---) indicates the boundary of the running band. The symbols (■) and (✖) indicate the adhesion and slip regions, respectively. The insets indicate the wheel/rail contact positions at instants t_1 - t_3 . The solid line (—) and dot line (···) indicate the crossing and wheel profiles, respectively. The symbol (○) in the insets indicates the contact patch centre.

Figure 3.8 compares the normal contact force. The wheel starts to contact with the nominal crossing nose at $x=230$ mm, while the initial contact on the long-term serviced crossing nose shifts forward to $x=261$ mm in the through direction and to $x=246$ mm in the divergent direction. On the long-term serviced crossing, the shift forward of the initial contact is mainly attributed to uneven crossing profile change (see Figure 3.6), i.e., severer change of the crossing nose than the wing rail should correspond to larger shift of the initial contact. Regarding the maximum contact force, it is 97 kN on the nominal crossing; on the long-term serviced crossing, it increases to 104 kN in the through direction and to 115 kN in the divergent direction. The increase of the contact force is also related to severer profile change of the crossing nose and thus larger wheel-rail impact energy.

Figure 3.9 shows the running band on the crossing nose. In the figure, the wheel-rail contact positions at the instants with the maximum contact force (i.e., t_1 , t_2 and t_3 Figure 3.8)

are attached. On the nominal crossing, the width of the running band, measured along the y axis, is up to 11 mm at $x=230-600$ mm. On the long-term serviced crossing, the maximum band width raises to 14 mm in the through direction. The wider running band is mainly from the enlargement of the curvature radius of the lateral-vertical nose profile (see the inset of Figure 3.9).

For easier comparison of the running band between the through and divergent directions, the running band obtained in the divergent direction is projected to the through direction by mirroring across the centreline N1 (Figure 3.6(a)). During the divergent motion on the long-term serviced crossing (Figure 3.9(c)), the width of the running band is smaller than the other two scenarios (Figure 3.9(a) and 3.9(b)). For example, the band width in Figure 3.9(c) is as small as 5 mm at $x=230-350$ mm, which is much smaller than the values during the through motion on the nominal crossing (8 mm in Figure 3.9(a)) and on the serviced crossing (14 mm in Figure 3.9(b)). The narrower running band is mainly attributed to the smaller curvature radius of the lateral-vertical crossing profile, as shown in the inset of Figure 3.9(c).

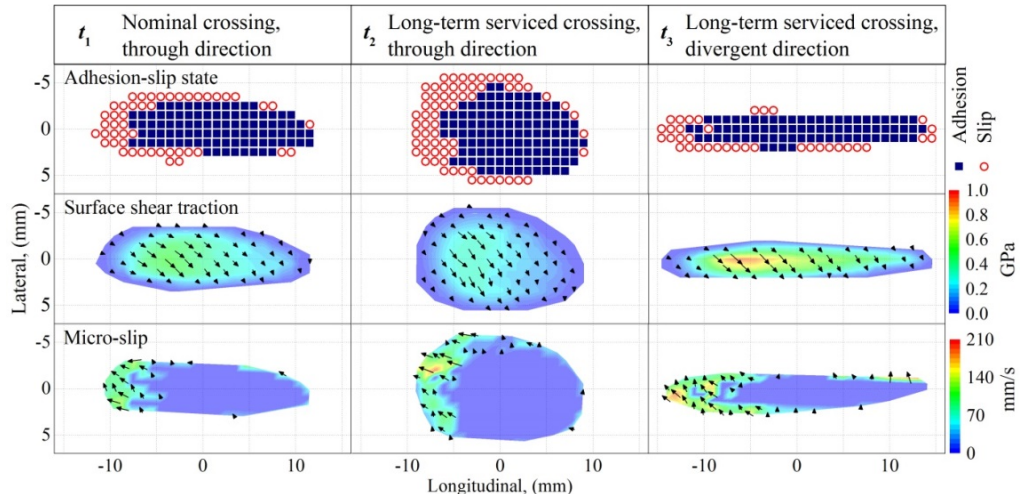


Figure 3.10: Contact parameters at instants t_1 , t_2 and t_3 . The first row is the adhesion-slip state, the second row is the field of surface shear traction and the third row is the field of micro-slip. The coordinate is adjusted for easier comparison of the results at different instants.

In Figure 3.9, the running band on both the nominal and the serviced crossings shifts laterally from wheel flange root toward wheel tread, i.e., from rail gauge corner to rail top. On the nominal crossing, the lateral shift is 6 mm at $x=230-600$ mm. On the long-term serviced crossing, the lateral shift raises to 24 mm in the through direction and to 7 mm in the divergent direction. The deviation in the lateral shift mainly comes from the non-identical and complex wheel/rail contact geometry, see Figure 3.6. During the through motion on the long-term serviced crossing, the larger lateral shift of the running band may have negative effects on the ride quality of vehicles, which will be analysed in future work.

To gain an insight into the wheel-crossing contact characteristics, the contact parameters in terms of adhesion-slip state, surface shear traction and micro-slip at instants t_1 , t_2 and t_3 are shown in Figure 3.10 and Table 3.1.

Table 3.1: Summary of contact parameters

Instant	Contact patch			Max. pressure (MPa)	Max. shear traction (MPa)	Max. micro-slip (mm/s)
	Length (mm)	Width (mm)	Area (mm ²)			
t_1	22	7	142	1583	529	146
t_2	18	11	185	1044	320	197
t_3	29	4	112	2691	918	201

At the selected instants, the contact patch obtained during the through motion on the long-term serviced crossing (t_2) is with the largest width (11 mm) and size (185 mm²). This is mainly due to, on one hand, larger curvature radius of the crossing profile (see the inset of Figure 3.9); on the other hand, the wheel-rail contact position is closer to wheel tread, where the curvature radius is larger than at flange root. On the contrary, the divergent motion on the long-term serviced crossing (t_3) corresponds to the smallest width (4 mm) and size(112 mm²) of the contact patch. Therefore, the curvature radius of the crossing profile and the wheel-rail contact position are the crucial factors determining the shape and size of the contact patch.

In the through direction, the magnitude of the normal contact force on the long-term serviced crossing (104 kN at t_2) is 7% larger than that on the nominal crossing (97 kN at t_1). Yet, higher value of contact force does not lead to higher values of contact stresses, since the maxima of pressure and shear traction on the long-term serviced crossing (1044 and 320 MPa at t_2) reduce by 34% and 40% compared to the values on the nominal crossing (1583 and 529 MPa at t_1). The non-synchronized variation between contact force and contact stresses is caused by the more significant growth of the contact patch size (30% from 142 to 185 mm²) than the contact force (7% from 97 to 104 kN), thus suppressing the magnitudes of contact stresses. On the long-term serviced crossing, the decrease of the contact stresses in the through direction is a benefit of the run-in process, i.e., the adjustment in the crossing profiles to achieve a stable relationship for the remainder of their service life. The run-in manifests as the widening of running band, the enlargement of contact patch size and eventually the reduction of contact stresses. On the long-term serviced crossing, 87% of the total traffic loads occurred in the through direction, so that the crossing profiles were adjusted to adapt for the major traffic loads in the through direction.

On the long-term serviced crossing, the run-in occurred in the through direction; however, it reduces the curvature radius of the crossing profile in the divergent direction, leading to narrower running band, smaller contact patch size and thus larger contact stresses. For example, the magnitudes of both pressure and shear traction (2691 and 918 MPa at t_3) are the largest among the three scenarios. Therefore, the run-in beneficial for the major traffic direction (through direction in the case study) can exacerbate the wheel-rail contact of the minor traffic direction (divergent direction in the case study).

Regarding the distribution of micro-slip, there was no micro-slip in the adhesion region (Figure 3.10). In the slip region, the maximum micro-slip takes place at around the rear edge of the contact patch. On the nominal crossing, the micro-slip is up to 146 mm/s at t_1 . On the

long-term serviced crossing, the maximum micro-slip raises to 197 mm/s in the through direction at t_2 and to 201 mm/s in the divergent direction at t_3 . Note that the combination of high contact stresses and micro-slip during the divergent motion on the long-term serviced crossing is expected to produce high value of wear, which will be examined in Figure 3.12.

The analysis in Section 3.3.2 shows the following wheel-rail contact characteristics on the long-term serviced crossing along the major traffic direction (through direction in the case study):

- The long-term serviced crossing experienced the run-in process, manifested as the increase of the curvature radius of the crossing profile, the widening of the running band and the enlargement of the contact patch size.
- Despite the slight increase of contact force on the serviced crossing, the magnitudes of pressure and shear traction decrease because of the run-in.
- The lateral shift of running band from wheel flange towards wheel tread increases significantly on the long-term serviced crossing.

3

Along the minor traffic direction (divergent direction in the case study), the following contact characteristics can be observed on the long-term serviced crossing:

- Both the width and size of the contact patch decrease on the long-term serviced crossing, owing to the decrease of the curvature radius of the crossing profile and the lateral shift of the wheel-rail contact position.
- The combination of increased contact force and decreased contact patch size raises the magnitudes of both pressure and shear traction on the long-term serviced crossing.

3.3.3 STEP 3: PERFORMANCE EVALUATION

In this section, the wheel-rail contact parameters from the FE simulation are used to calculate the distributions of plastic deformation and wear. By comparing these results between nominal and long-term serviced crossings, the performance of the long-term serviced crossing can be addressed.

Figure 3.11(a) shows the distribution of the von Mises stress, which is calculated using Equation (3.4). On the nominal crossing, the von Mises stress exceeds the yield strength (500 MPa) from $x=231$ mm on, with the maximum being 947 MPa occurs at $x=255$ mm. On the long-term serviced crossing, the maximum von Mises stress decreases by 26% to 700 MPa in the through direction, and the region with plastic deformation shrinks to $x=294$ -509 mm. The decrease of the von Mises stress and plastic deformation in the through direction is a benefit of the run-in. In the divergent direction, the von Mises stress on the long-term serviced crossing is up to 2098 MPa at $x=276$ mm, which raises by 122% compared to that on the nominal crossing. Suffered from the significantly increased von Mises stress, plastic deformation takes place from $x=249$ mm on.

Figure 3.11(b) shows the field of the von Mises stress within the running band. In the figure, the trajectories of the contact patch centre as well as the maximum von Mises stress are given. The two trajectories do not coincide with each other, and the lateral distance between them varies along the longitudinal direction. On the nominal crossing, the lateral distance is up

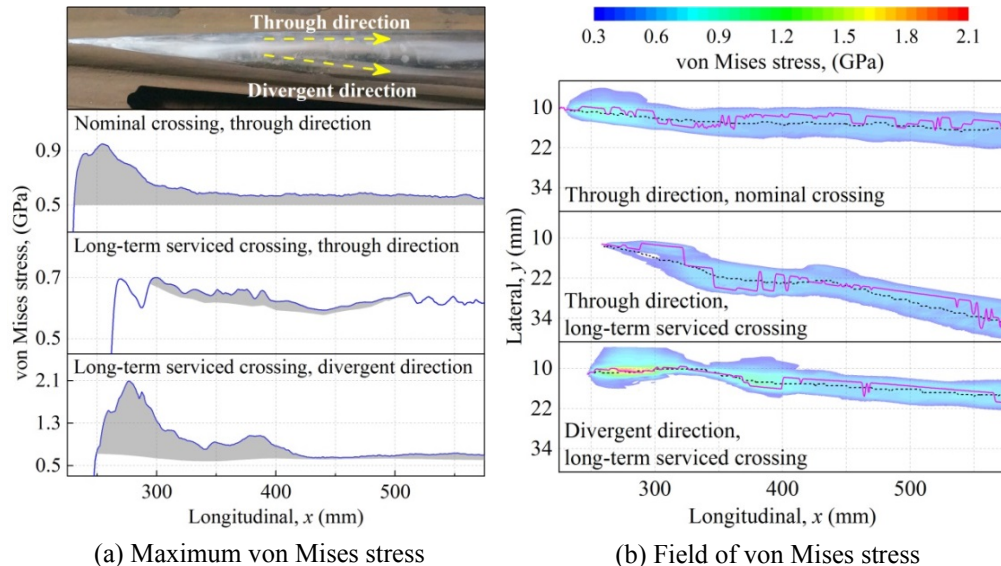


Figure 3.11: Plastic deformation of crossing nose. The shadow area in (a) indicates the region with plastic deformation. The scales in (a) are different for each subplot. The solid line (—) and the dashed line (---) in (b) indicate the trajectories of the maximum von Mises stress and the contact patch centre.

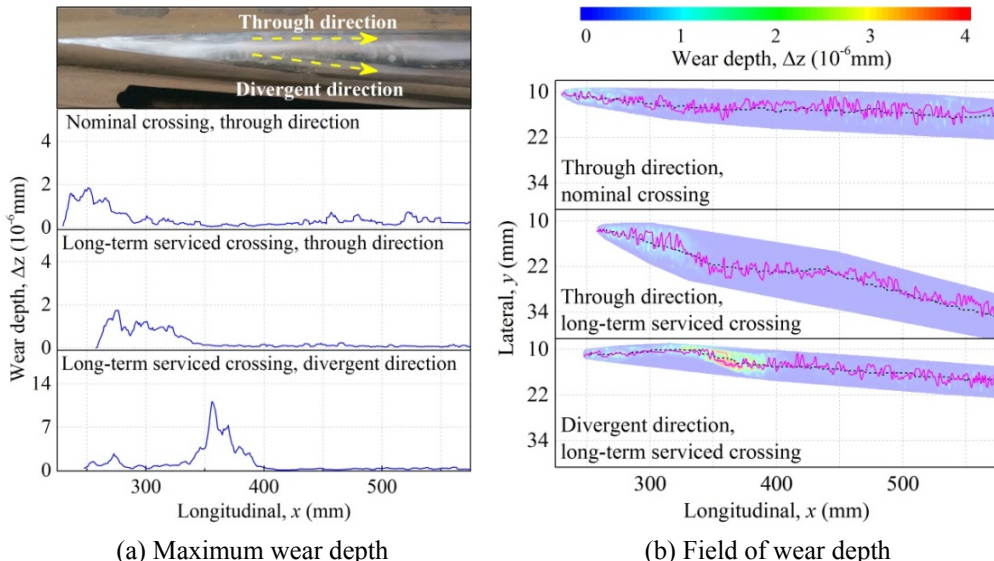


Figure 3.12: Wear of crossing nose. The scales in (a) are different for each subplot. The solid line (—) and the dashed line (---) in (b) indicate the trajectories of the maximum wear depth and the contact patch centre.

to 3.7 mm; on the long-term serviced crossing, the maximum lateral distance raises to 4.9 mm in the through direction whereas reduces to 2.8 mm in the divergent direction. Due to the complex wheel-crossing contact geometry, the maximum von Mises stress may occur any region within the running band. Thus, wider running band generally comes with larger value of lateral distance, and vice versa.

Figure 3.12(a) shows the distribution of wear caused by one wheelset passage, which is calculated using Equation (3.4). On the nominal crossing, the wear depth caused by one wheel passage reaches its maximum of 1.9×10^{-6} mm at $x=252$ mm; on the long-term serviced crossing, the maximum reduces by 11% to 1.7×10^{-4} mm at $x=277$ mm in the through direction. The slight decrease of the wear depth is a benefit of the run-in, manifested as the decreased pressure (Table 3.1) as well as the increased hardness (Figure 3.7). In the divergent direction, the maximum wear depth on the long-term serviced crossing is 11.2×10^{-6} mm at $x=356$ mm, which raises by 489% compared to that on the nominal crossing. The sharp increase of the wear depth is owing to the growth of both pressure and micro-slip (Table 3.1). of lateral distance, and vice versa.

Figure 3.12(a) shows the distribution of wear caused by one wheelset passage, which is calculated using Equation (3.4). On the nominal crossing, the wear depth caused by one wheel passage reaches its maximum of 1.9×10^{-6} mm at $x=252$ mm; on the long-term serviced crossing, the maximum reduces by 11% to 1.7×10^{-4} mm at $x=277$ mm in the through direction. The slight decrease of the wear depth is a benefit of the run-in, manifested as the decreased pressure (Table 3.1) as well as the increased hardness (Figure 3.7). In the divergent direction, the maximum wear depth on the long-term serviced crossing is 11.2×10^{-6} mm at $x=356$ mm, which raises by 489% compared to that on the nominal crossing. The sharp increase of the wear depth is owing to the growth of both pressure and micro-slip (Table 3.1).

Figure 3.12(b) shows the field of wear depth within the running band. In the figure, the trajectories of the contact patch centre as well as of the maximum wear depth are given. As can be seen, the lateral distance between the two trajectories varies along the longitudinal direction, and wider running band generally comes with larger lateral distance (which is 4.0 mm, 4.5 mm and 3.8 mm at the three scenarios). This behaviour, similar to that observed from von Mises stress (Figure 3.11(b)), is also related to the complex measured wheel-rail contact geometry. Comparing Figure 3.12(b) with Figure 3.11(b), the trajectory of the maximum wear depth is not as smooth as the maximum von Mises stress, because the wear is a product of pressure and micro-slip, and contains the irregularities of both components.

The analysis in Section 3.3.3 shows the following characteristic distributions of plastic deformation and wear on the long-term serviced crossing:

- In the major traffic direction (through direction in the case study), the magnitudes of both von Mises stress and wear depth decrease compared to those on the nominal crossing, which is a benefit of the run-in.
- In the minor traffic direction (divergent direction in the case study), the magnitudes of both von Mises stress and wear depth raise significantly on the long-term serviced crossing.
- The trajectories of the maximum von Mises stress and wear depth do not coincide with the centreline of the running band. The lateral distance between them varies along the

longitudinal direction, and wider running band generally comes with larger lateral distance.

Based on the case study presented in Section 3.3, the performance of the long-term serviced crossing can be assessed. On one hand, the crossing experienced a run-in process in the through direction (major traffic direction in the case study), so that the rail degradation is slow and it would not necessarily be the major cause for urgent maintenance. On the other hand, the crossing rails would suffer from much faster degradation in the divergent direction (minor traffic direction in the case study). To avoid the sudden failure of rails in the minor traffic direction, preventive maintenance (e.g., grinding and repair welding) would actually be required, so that the safety of railway operation can be guaranteed.

3.4 DISCUSSION

3.4.1 COMPARISON OF NUMERICAL RESULTS WITH MEASUREMENTS

To demonstrate the capability of the proposed method, the second 3D profile measurement were performed 274 days after the first one. During the period, 87% of the total traffic loads (1.06 million wheel cycles or 15.10 million gross tons) took place in the through direction, while the rest was in the divergent direction. Figure 3.13(a) shows the measured profile change of the crossing nose during the period. For comparison purpose, the simulated running bands in both through and divergent directions are attached. In the figure, the regions with significant measured profile changes are almost enveloped by the simulated running bands. These regions mainly distribute at around $x=250-500$ mm in the through direction and around $x=250-450$ mm in the divergent direction, at which the simulated plastic deformation (Figure 3.11) and wear depth (Figure 3.12) also reach large values. This information demonstrates the capability of the proposed method in representing the characteristic rail degradation on the long-term serviced crossing. There are some small regions with clearly visible profile changes yet outside of the simulated running bands, probably attributed to: 1) the FE model only employs the nominal wheel profile and nominal parameters of the track components, whereas they can also degrade (e.g., hollow wheel tread and worn railpad) during usage, which further affect the frictional wheel/rail contact; 2) Randomness of wheel-rail interaction (e.g., hunting oscillation) is neglected in the analysis.

Figure 3.13(b) shows a spalling fatigue observed on the crossing nose, which took place in the divergent trajectory. In general, spalling is associated with high contact stresses in the material. In the numerical analysis, the contact stresses in the divergent direction are significant higher than those in the through direction (Figure 3.9), so that a spalling has more chance to grow in the divergent direction. A reasonable agreement can be achieved between in-situ observation and numerical simulation.

3.4.2 CRITERIA FOR GUIDING PREVENTIVE MAINTENANCE

The spalling fatigue in Figure 3.13(b) can be prevented if maintenance actions (e.g., grinding and welding) can be timely conducted. Proper criteria should be specified to determine the strategy of the maintenance. In general, high value of contact stresses in the material could be more dangerous than high value of wear, because the former can induce not only plastic deformation but also rolling contact fatigue (e.g., spalling, head checks, and shelling). Since severe rolling contact fatigue may result in the sudden failure of crossing rail,

stricter criterion should be specified for contact stress.

3

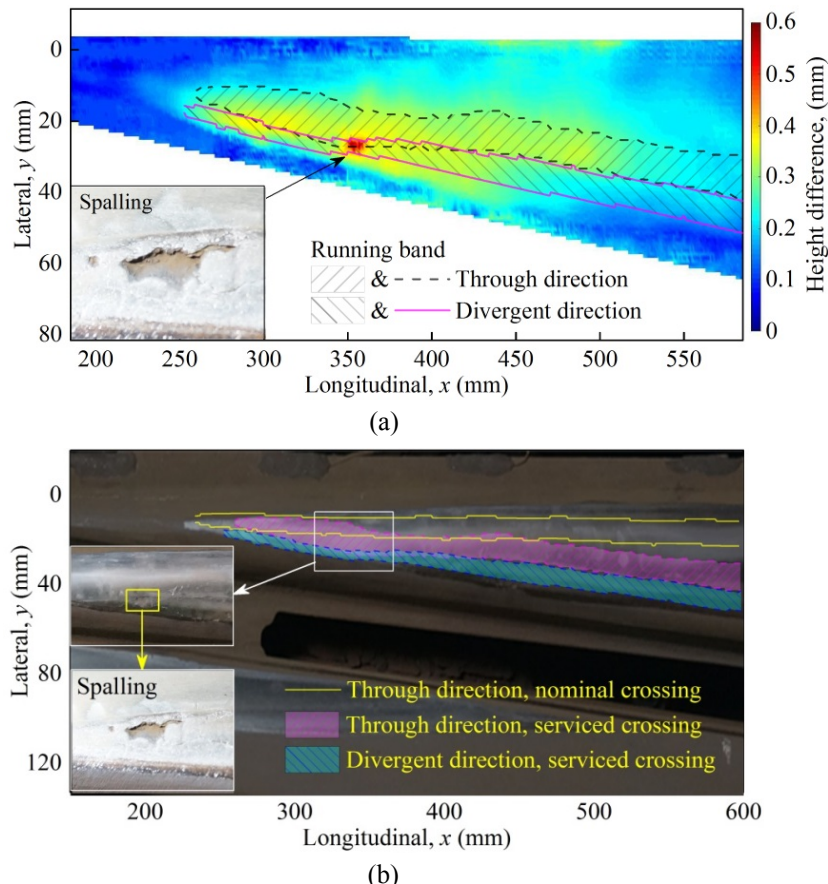


Figure 3.13: Results from subsequent profile measurement and observation. (a) Measured profile change of crossing nose during 274-day usage. (b) Spalling observed on the crossing nose

In the divergent direction, the maxima of the von Mises stress and wear depth on the serviced crossing increase by 122% and 489% compared to the baselines on the nominal crossing (see Figures 3.11 and 3.12). To minimize the presence of rolling contact fatigue, the criterion for the maximum von Mises stress is set to 2 times of the baseline. In addition, the criterion for the maximum wear depth, which can be less strict, is set to 3 times of the baseline. If the evaluation results exceed these criteria, preventive maintenance actions should be timely performed.

Note that the preceding criteria are set for the crossing type of 54E1-1:9 at a train operational speed of 40 km/h. These criteria should be adjusted at different crossing types and operational conditions. For example, stricter criteria are required for higher train speed, so that the safety of railway operation can be guaranteed.

3.4.3 EXTENDING THE CAPABILITY OF THE PROPOSED METHOD

In the present study, we analyse the degradation of crossing rails during the passage of one wheelset. To investigate the rail degradation caused by the passage of a number of wheels, the following study should be done in the subsequent work: 1) Analysis on the residual stress in the rail material; 2) Regular measurement of rail hardness to correct the yield strength of rail material; 3) Prescribe the statistics of axle load, train speed and moving direction for the FE simulation.

Apart from crossing rails, other track components (e.g., ballast and sleeper) can also experience degradation during long-term usage. For example, the presence of void ballast, moving sleeper as well as worn fastening and railpad exacerbate dynamic wheel-rail interaction and speed up the failure of the track structure. In future work, the parameters of these track components will be derived via in-situ impact measurements [42, 43], in an effort to achieve a more comprehensive evaluation of the condition of long-term serviced crossings.

3.5 SUMMARY

In the railway industry, the systematic evaluation of the performance of long-term serviced crossing rails is important to timely conduct preventive maintenance actions and avoid the sudden failure of the track infrastructure. In this paper, we propose a method capable of analysing the dynamic wheel/rail interaction at long-term serviced crossings. The method composes of 1) 3D profile and hardness measurements serving as the input, 2) FE simulation of wheel/rail interaction for simulating the contact behaviour and 3) numerical prediction of rail degradation. A case study was then conducted on a long-term serviced crossing to demonstrate the proposed method. A good agreement is achieved between the measured hardness and the simulated von Mises stress, which demonstrates the capability of the method in capturing the wheel/rail contact characteristics at long-term serviced crossings. From the preceding analysis, the following performance of the long-term serviced crossings is assessed:

- In the major traffic direction (in terms of the percentage of the total traffic loads), the long-term serviced crossing experienced a run-in process, manifested as the widening of running band, the enlargement of contact patch size and eventually the reduction of contact stresses. The magnitude of micro-slip raises on the long-term serviced crossing, whereas its growth is not as significant as the decrease of shear traction, so that the wear depth decreases.
- The run-in process occurred in the major traffic direction at the long-term serviced crossing; however, it exacerbates the wheel/rail contact in the minor traffic direction by decreasing the curvature radius of the crossing profile. Consequently, the running band narrows, the contact patch size decreases and the contact stresses enlarge, eventually leading to significantly increased von Mises stress and wear depth on the long-term serviced crossing. This information indicates the necessity to conduct preventive maintenance actions, so that the safety of railway operation can be guaranteed.

REFERENCES

[1] J.C. Nielsen, R. Lundén, A. Johansson, T. Vernersson, *Train-track interaction and mechanisms of irregular wear on wheel and rail surfaces*, Vehicle System Dynamics **40**, 3-54 (2003).

- [2] O.F. Eker, F. Camci, A. Guclu, H. Yilboga, M. Sevkli, S. Baskan, *A simple state-based prognostic model for railway turnout systems*, IEEE Transactions on Industrial Electronics **58**, 1718-1726 (2011).
- [3] M. Wiest, W. Daves, F. Fischer, H. Ossberger, *Deformation and damage of a crossing nose due to wheel passages*, Wear **265**, 1431-1438 (2008).
- [4] Z. Wei, C. Shen, Z. Li, R. Dollevoet, *Wheel-rail impact at crossings: relating dynamic frictional contact to degradation*, Journal of Computational and Nonlinear Dynamics **12**, 12:041016 (2017).
- [5] P. Wang, J. Xu, K. Xie, R. Chen, *Numerical simulation of rail profiles evolution in the switch panel of a railway turnout*, Wear **366**, 105-115 (2016).
- [6] C. Wan, V. Markine, I. Shevtsov, *Improvement of vehicle-turnout interaction by optimising the shape of crossing nose*, Vehicle System Dynamics **52**, 1517-1540 (2014).
- [7] C. Andersson, T. Dahlberg, *Wheel/rail impacts at a railway turnout crossing*, Proceedings of the Institution of Mechanical Engineers, Part F: Journal of Rail and Rapid Transit **212**, 123-134 (1998).
- [8] Z. Ren, S. Sun, W. Zhai, *Study on lateral dynamic characteristics of vehicle/turnout system*, Vehicle System Dynamics **43**, 285-303 (2005).
- [9] X. Shu, N. Wilson, C. Sasaoka, J. Elkins, *Development of a real-time wheel/rail contact model in NUCARS® and application to diamond crossing and turnout design simulations*, Vehicle System Dynamics **44**, 251-260 (2006).
- [10] E. Kassa, C. Andersson, J.C. Nielsen, *Simulation of dynamic interaction between train and railway turnout*, Vehicle System Dynamics **44**, 247-258 (2006).
- [11] S. Alfi, S. Bruni, *Mathematical modelling of train-turnout interaction*, Vehicle System Dynamics **47**, 551-574 (2009).
- [12] S. Bruni, I. Anastasopoulos, S. Alfi, A. Van Leuven, G. Gazetas, *Effects of train impacts on urban turnouts: Modelling and validation through measurements*, Journal of Sound and Vibration **324**, 666-689 (2009).
- [13] Y.Q. Sun, C. Cole, M. McClanahan, *The calculation of wheel impact force due to the interaction between vehicle and a turnout*, Proceedings of the Institution of Mechanical Engineers, Part F: Journal of Rail and Rapid Transit **224**, 391-403 (2010).
- [14] J.C. Nielsen, B.A. Pålsson, P.T. Torstensson, *Switch panel design based on simulation of accumulated rail damage in a railway turnout*, Wear **366**, 241-248 (2016).
- [15] M. Ansari, I. Hazrati, E. Esmailzadeh, S. Azadi, *Wear rate estimation of train wheels using dynamic simulations and field measurements*, Vehicle System Dynamics **46**, 739-759 (2008).
- [16] B. Ripke, K. Knothe, *Simulation of high frequency vehicle-track interactions*, Vehicle System Dynamics **24**, 72-85 (1995).
- [17] E. Kassa, J.C. Nielsen, *Stochastic analysis of dynamic interaction between train and railway turnout*, Vehicle System Dynamics **46**, 429-449 (2008).
- [18] J.J. Kalker, *Three-dimensional elastic bodies in rolling contact* (Kluwer, 1990).
- [19] Z. Li, J.J. Kalker, *The computation of wheel-rail conformal contact*, in *4th World Congress on Computational Mechanics* (Buenos Aires, Argentina, 1998).

[20] Z. Li, *Wheel-rail rolling contact and its application to wear simulation*, PhD dissertation, Delft University of Technology (2002).

[21] N. Burgelman, Z. Li, R. Dollevoet, *A new rolling contact method applied to conformal contact and the train–turnout interaction*, Wear **321**, 94-105 (2014).

[22] J. Blanco-Lorenzo, J. Santamaría, E.G. Vadillo, N. Correa, *On the influence of conformity on wheel–rail rolling contact mechanics*, Tribology International **103**, 647-667 (2016).

[23] Z. Yang, Z. Li, R. Dollevoet, *Modelling of non-steady-state transition from single-point to two-point rolling contact*, Tribology International **101**, 152-163 (2016).

[24] D. Nicklisch, E. Kassa, J. Nielsen, M. Ekh, S. Iwnicki, *Geometry and stiffness optimization for switches and crossings, and simulation of material degradation*, Proceedings of the Institution of Mechanical Engineers, Part F: Journal of Rail and Rapid Transit **224**, 279-292 (2010).

[25] A. Johansson, B. Pålsson, M. Ekh, J. Nielsen, M. Ander, J. Brouzoulis, *Simulation of wheel–rail contact and damage in switches & crossings*, Wear **271**, (472-481) 2011.

[26] P. Wriggers, *Computational contact mechanics*, (Springer, 2006).

[27] X. Zhao, Z. Li, *The solution of frictional wheel–rail rolling contact with a 3D transient finite element model: Validation and error analysis*, Wear **271**, 444-452 (2011).

[28] M. Pletz, W. Daves, H. Ossberger, *A wheel set/crossing model regarding impact, sliding and deformation-Explicit finite element approach*, Wear **294**, 446-456 (2012).

[29] J. Wiedorn, W. Daves, U. Ossberger, H. Ossberger, M. Pletz, *Simplified explicit finite element model for the impact of a wheel on a crossing-validation and parameter study*, Tribology International **111**, 254-264 (2017).

[30] L. Xin, V. Markine, I. Shevtsov, *Numerical analysis of the dynamic interaction between wheel set and turnout crossing using the explicit finite element method*, Vehicle System Dynamics **54**, 301-327 (2016).

[31] E. Kassa, J.C. Nielsen, *Dynamic interaction between train and railway turnout: full-scale field test and validation of simulation models*, Vehicle System Dynamics **46**, 521-534 (2008).

[32] J. Cahoon, W. Broughton, A. Kutzak, *The determination of yield strength from hardness measurements*, Metallurgical Transactions **2**, 1979-1983 (1971).

[33] T. Pearce, N. Sherratt, *Prediction of wheel profile wear*, Wear **144**, 343-351 (1991).

[34] I. Zobory, *Prediction of wheel/rail profile wear*, Vehicle System Dynamics **28**, 221-259 (1997).

[35] Z. Li, J.J. Kalker, *Simulation of severe wheel-rail wear*, in *6th International Conference on Computer Aided Design, Manufacture and Operation in the Railway and Other Mass Transit Systems* (Lisbon, Portugal, 1998), pp. 393-402.

[36] J. Archard, W. Hirst, *The wear of metals under unlubricated conditions*, Proceedings of the Royal Society of London A: Mathematical, Physical and Engineering Sciences, 397-410 (1956).

[37] T. Jendel, *Prediction of wheel profile wear—comparisons with field measurements*, Wear **253**, 89-99 (2002).

3

- [38] R. Dollevoet, Z. Li, O. Arias-Cuevas, *A method for the prediction of head checking initiation location and orientation under operational loading conditions*, Proceedings of the Institution of Mechanical Engineers, Part F: Journal of Rail and Rapid Transit **224**, 369-374 (2010).
- [39] X. Zhao, Z. Li, J. Liu, *Wheel-rail impact and the dynamic forces at discrete supports of rails in the presence of singular rail surface defects*, Proceedings of the Institution of Mechanical Engineers, Part F: Journal of Rail and Rapid Transit **226**, 124-139 (2012).
- [40] M. Oregui, Z. Li, R. Dollevoet, *An investigation into the modeling of railway fastening*, International Journal of Mechanical Sciences **92**, 1-11 (2015).
- [41] Y. Areiza, S. Garcés, J. Santa, G. Vargas, A. Toro, *Field measurement of coefficient of friction in rails using a hand-pushed tribometer*, Tribology International **82**, 274-279 (2015).
- [42] K. Knothe, Y. Wu, *Receptance behaviour of railway track and subgrade*, Archive of Applied Mechanics **68**, 457-470 (1998).
- [43] M. Oregui, Z. Li, R. Dollevoet, *Identification of characteristic frequencies of damaged railway tracks using field hammer test measurements*, Mechanical Systems and Signal Processing **54**, 224-242 (2015).

4

IDENTIFYING THE CHARACTERISTICS OF ABA AT CROSSING

Monitoring the condition of railway crossings using ABA measurements requires a better understanding of the characteristics of ABA under various test conditions. In this chapter, we combine the ABA and hammer test measurements to analyse the influence of train speed, moving direction (facing and trailing directions with respect to the crossing), sensor position (leading and rear wheels of a bogie) and the natural response of track structure on ABA signals. Our results indicate that the major frequency bands of the vertical ABA at 240-305 and 505-620 Hz are related to the natural frequencies of the crossing at 265, 490, 548 and 621 Hz; thus, these frequency bands are not greatly affected by variations in train speed, moving direction and sensor position. The vibration energy concentrated at the major frequency bands of the vertical ABA increases at higher train speeds, along the facing direction and from the leading wheel. The vibrations of the crossing rails at the major frequency bands of the vertical ABA are a combination of bending and torsion rather than solely bending, as the vibrations of the wing rails are not synchronized. These results can be used to calibrate and improve the ABA system for monitoring the condition of crossings.

This chapter is based on:

Wei Z, Boogaard A, Núñez A, Li Z, Dollevoet R. An integrated approach for characterizing the dynamic behavior of the wheel-rail interaction at crossings. IEEE Transactions on Instrumentation and Measurement, to be published. DOI: 10.1109/TIM.2018.2816800

4.1 INTRODUCTION

Railway systems are a major mode of passenger and freight transportation worldwide. In recent years, the increased demands on railway systems, including higher speeds, greater capacity and longer service times, have accelerated the deterioration of track infrastructure. In particular, crossings deteriorate much faster than plain tracks because of the impact of wheels on rails [1] at geometric discontinuities (e.g., the gap between the closure rail and crossing nose in Figure 4.1). In turn, deteriorated crossings exacerbate the dynamic vehicle/track interaction, increase maintenance costs and endanger the safety of railway operations. Therefore, it is important to efficiently monitor the condition of crossings so that maintenance measures, such as grinding and welding [2], can be performed in a timely fashion on deteriorated crossings.

4

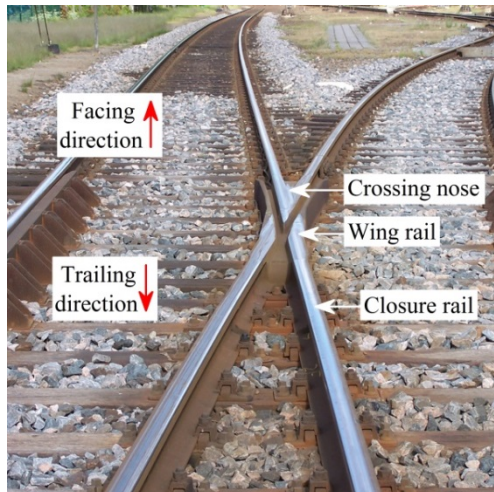


Figure 4.1: Schematic diagram of a crossing

In the Dutch railway network, crossings are inspected by human visual inspection and ultrasonic measurement. Visual inspection involves visiting the tracks or watching videos of tracks, which requires a substantial number of man-hours for large-scale railway networks. In addition, visual assessment of the severity of defects is subjective. Ultrasonic measurement is better able to detect internal cracks [3] but is not suitable for rail surface defects [4]. To fill the gap between the increased demands on the railway network and the low efficiency of the current inspection methodologies, a prompt diagnostic system is required.

Train-borne inspection systems based on ABA measurements represent an automatic and efficient method for condition monitoring of track infrastructure. Because the ABA signal is related to the contact force at the wheel/rail interface, small or minor defects can be detected if they affect the dynamic wheel-rail contact force. Moreover, the ABA system can be installed on in-service trains running at operational speeds; thus, they do not affect railway operations. The ABA system has been used to assess both periodic defects (e.g., corrugations [5] and wheel flats [6]) and isolated defects (e.g., squats [7], worn welds [8] and insulated joints [9]) on plain tracks. The defect detection mechanism employed by the ABA system relies on identifying changes in the temporal and frequency response with respect to the nominal

condition. At crossings, the application of the ABA system is more complicated than at plain tracks because the measured ABA signals reflect dynamic responses related to both inherent geometric discontinuities and undesirable defects.

To evaluate the health condition of crossings using the ABA system, the influence of various test conditions (e.g., train speed and moving direction) on the ABA signals must be studied, as it is impossible to keep these conditions constant during implementation on in-service trains. In addition, previous studies have shown that the characteristic frequencies of ABA on plain tracks are related to the natural behaviour of the track structure [10]. If this is also the case at crossings, the natural response of crossings and their relationship to the characteristics of ABA must be investigated because the natural response can differ greatly between crossing types.

This chapter investigates the characteristics of ABA at crossings under various test conditions. These conditions include train speed, train moving direction (facing and trailing direction with respect to the crossing), sensor position (leading and rear wheels in a bogie) and crossing natural response. Several previous studies have examined ABA signals at crossings [11-13], but they did not investigate the characteristics of ABA under various test conditions and did not combine ABA measurements with other methodologies (e.g., hammer tests [14]) to understand the relationship between vehicle and track dynamics. We aim to fill this knowledge gap by correlating ABA measurements with the results from a roving-accelerometer hammer test. The results will not only provide a better understanding of dynamic vehicle-crossing interaction but also advance the utility of the ABA system for condition monitoring of crossings.

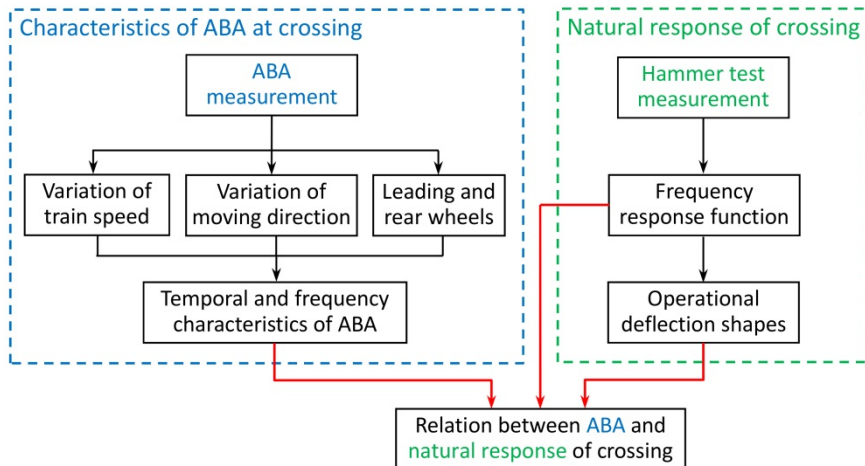


Figure 4.2: Structure of this chapter

Figure 4.2 illustrates the methodology of this chapter. Section 4.2 introduces the in-situ ABA and hammer test measurements. Section 4.3 analyses the characteristics of ABA under various test conditions, including train speed, moving direction (facing and trailing direction with respect to the crossing) and sensor position (leading and rear wheels in a bogie). Section 4.4 investigates the relationship between the characteristics of ABA and the natural responses of a crossing. Finally, Section 4.5 states the main conclusions.

4.2 IN-SITU ABA AND HAMMER TEST MEASUREMENTS

In-situ ABA and hammer test measurements are used to analyse the dynamics of the vehicle-track system. The measurements were conducted on a nominal crossing of the 54E1-1:9 type (with the UIC54 rail profile and a crossing angle of 1:9). The train operational speed over the crossing is limited to 40 km/h.

4.2.1 ABA MEASUREMENT SYSTEM

The ABA system comprises three main components: accelerometers, a GPS antenna and a tachometer. The system was installed on a measurement coach in the Netherlands, see Figure 4.3(a). In the system, accelerometers were mounted on the axle boxes of a bogie to record the ABA signals, see Figure 4.3(b). The sampling frequency of ABA was set to 25.6 kHz to make sure that the ABA up to 3 kHz can be accurately captured with a broad range of measuring speed. A GPS antenna was installed on the train roof to record the position of the train. Besides, a tachometer was used to record the train speed and obtain a better positioning of the ABA signals.

Table 4.1 lists the test scenario for the ABA measurements. The ABA signals were acquired 1) at two speeds of 28 and 36 km/h, 2) along two moving directions (facing and trailing in Figure 4.3(c)) and 3) from two wheels 1 and 2. In the ABA measurement, the train speeds of 28-36 km/h are restricted by the speed limit at the measured crossing (40 km/h).

Table 4.1: Test scenario for ABA measurements

Item	Parameter
Train speed	28 km/h
	36 km/h
Moving direction	Facing direction (from closure rail to crossing nose)
	Trailing direction (from crossing nose to closure rail)
Sensor position	Wheel 1 (leading wheel in facing direction)
	Wheel 2 (rear wheel in facing direction)

The ABA signals were measured in the time domain. However, it is not straightforward to extract the characteristic dynamic response only by analysing the waveform and amplitude of the ABA signals. Frequency analysis is required because it can provide crucial information that is challenging to identify in the time domain. In general, the majority of the conventional time-frequency analysis techniques can be classified into two categories: linear transform (e.g., short-time Fourier transform (STFT) [15] and wavelet transform (WT) [16]) and quadratic transform (e.g., Wigner-Ville distribution (WVD) [17] and its variants). The STFT uses a fixed window size such that a trade-off must be made between time and frequency resolutions. The WT employs scaling and translating windows that can effectively preserve the transient characteristics of a signal. However, the WT is a non-adaptive method and the time-frequency presentation relies on a pre-determined basis, independent of the analysed signal. The WVD can provide a high resolution of the time-frequency representation, but it is subjected to the interference of cross-term.

In Figure 4.4, we compare the performance of four time-frequency analysis methods, including continuous wavelet transform (CWT, non-adaptive linear method), synchro-

squeezing transform [18] (SST, non-adaptive linear method), WVD (non-adaptive quadratic method) and empirical mode decomposition [19] (EMD, adaptive method). The ABA signals to be processed are measured with a sampling frequency of 25.6 kHz, and the frequency of interest is 150-800 Hz. In general, the WVD has the poorest performance due to the cross-term interference. In this study, the CWT is used because: 1) The sampling frequency of the ABA is 25.6 kHz and the interested frequency is 150-800 Hz, such that the limitation of the CWT (low time resolution at very low frequency range and low frequency resolution at very high frequency) can be significantly reduced; 2) the capability of the CWT in processing ABA signals has been demonstrated in the literature [7, 20, 21]; and 3) the ABA signals are not very noisy due to the thorough type selection and instrumentation of accelerometers, and it is not difficult to distinguish the characteristic frequencies.

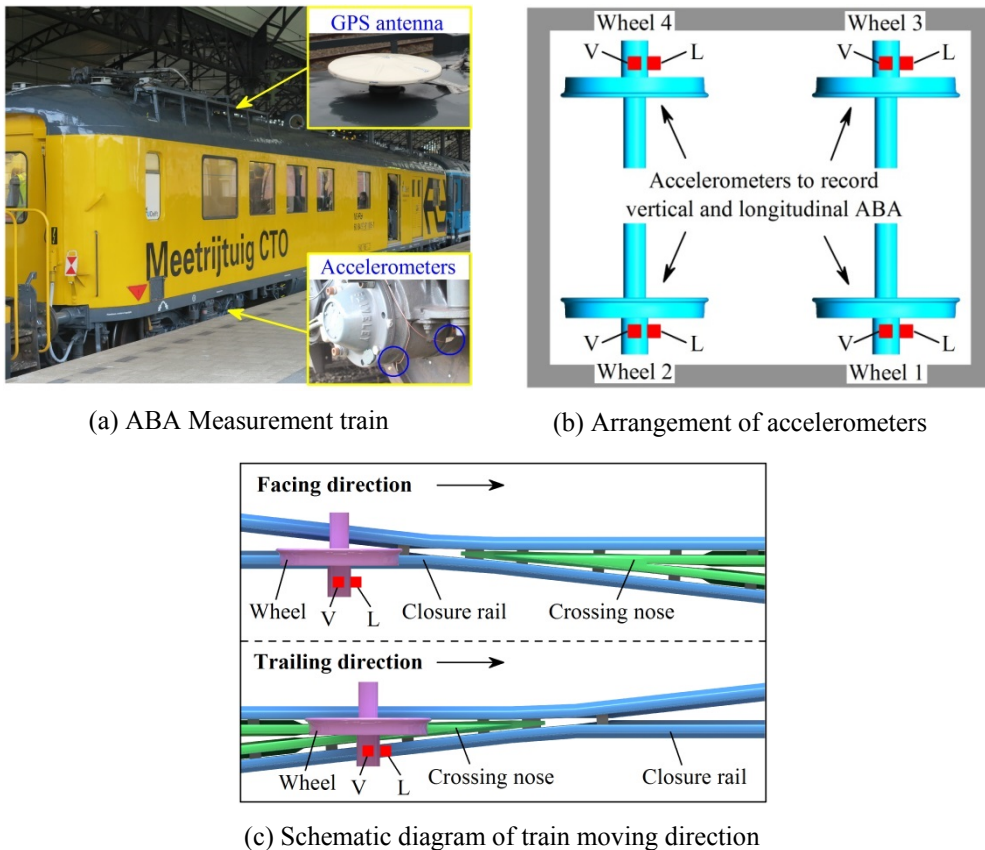


Figure 4.3: ABA measurement system. Letters V and L denote the accelerometers mounted in vertical and longitudinal directions. The wheel moves from closure rail to crossing nose in the facing direction, while it moves oppositely in the trailing direction.

In the CWT, the convolutions of the analysed signal are calculated with a group of scaled and shifted wavelet functions. The wavelet coefficients $W_n(s)$ of the analyzed signal x can be represented as follows [16]:

$$W_n(s) = \sum_{n'=0}^{N-1} x_{n'} \psi^* \left[\frac{(n'-n)\delta_t}{s} \right] \quad (4.1)$$

where ψ is the mother wavelet, s is the wavelet scale, N is the number of points in the time series, $n' = 0, \dots, N-1$, δ_t is the time step, n is the continuous variable for the translation and $*$ denotes a complex conjugate. Here, the Morlet function was used as the mother wavelet [22].

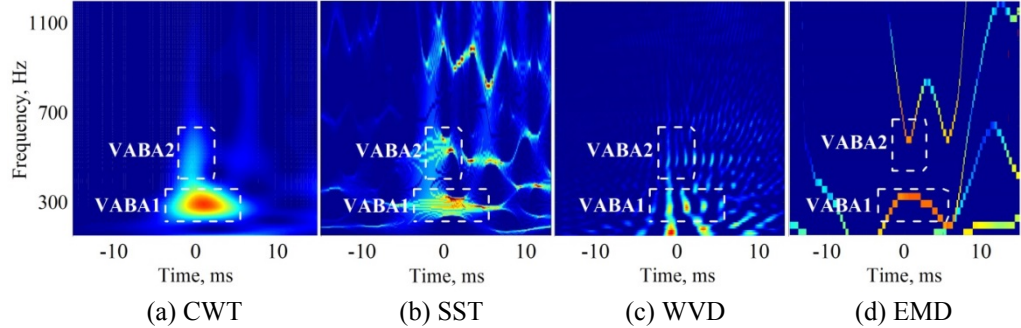


Figure 4.4: Time-frequency representation of the ABA with (a) CWT, (b) SST, (c) WVD and (d) EMD. VABA1 and VABA2 indicate the major ABA frequency bands at 265-305 and 510-600 Hz.

Thereafter, the WPS was calculated through the square of the wavelet coefficients $|W_n^2(s)|$. To quantify the distributions of the WPS at each frequency, the GWPS $|\bar{W}^2(s)|$ was calculated and expressed as follows:

$$\bar{W}^2(s) = \frac{1}{N} \sum_{n=0}^{N-1} |W_n^2(s)| \quad (4.2)$$

4.2.2 SETUP OF HAMMER TEST

Impact measurements are commonly used to characterize the dynamics of the track structure [23] and derive the parameters of the track components [24]. Several impact methodologies are specified in the literature for various components and conditions. For example, the track vibrations in the low frequency range (below 150 Hz) mainly correspond to the properties of the track substructure components (e.g., subgrade and ballast) [25]; thus, the falling weight test [26] is capable to provide sufficient energy to fully excite these components. In contrast, track vibrations at 150-800 Hz are closely related to the properties of the rails and track superstructure components (e.g., fastening, railpad and sleeper); these vibrations are best tested using a sledgehammer with a soft tip. At higher frequencies (800-3000 Hz), the structural vibrations are dominated by the rails, and thus a light hammer with a hard tip should be used.

In this study, an instrumented sledge hammer (PCB-086D50) with a plastic tip is used, see Figure 4.5(a). The sledge hammer is selected because its capability covers the interested characteristic frequencies of the vertical ABA, which will be analysed in Section 4.4. To record the vertical vibrations of the crossing, seven accelerometers (Brüel & Kjær 4514-004) were placed on the rail head and baseplate with magnet base. The hammer and accelerometers

are connected to a data logger device (MBBM-PAK-MKII). The sampling frequency of the force and acceleration signals was set to 4096 Hz, and the duration of the signals was set to 1000 ms.

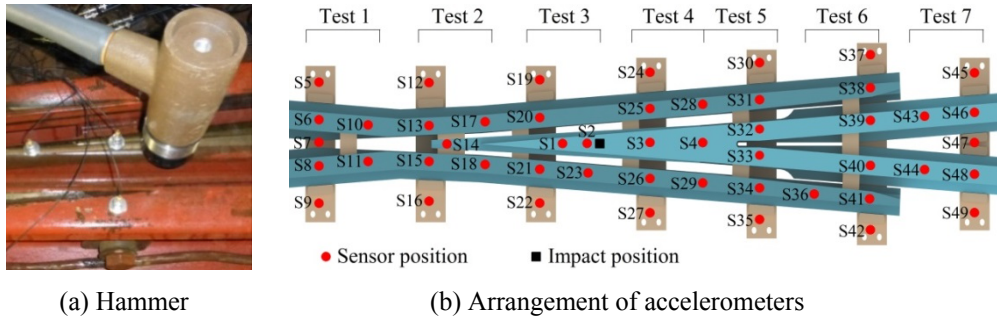


Figure 4.5: In-situ hammer test measurements

4

In the literature, the natural behaviour of railway tracks is commonly measured at fixed positions [14, 27, 28]; two typical positions are the on-support and mid-span [29, 30]. This simplified setup is appropriate for plain tracks, but is less useful at crossings due to their complex structure and discontinuous geometry. This means that the measured vibrations may differ greatly at each sensor position, leaving the dynamic behaviour of the entire structure unclear. Therefore, it is preferable to highlight the global nature of the crossing by measuring the vibrations at many positions. In this study, a roving-accelerometer approach [31-33] was used for the hammer test. The impact occurred in the same position throughout measurement, while the accelerometers were rearranged seven times. Figure 4.5(b) shows the arrangement of the accelerometers. Using the roving-accelerometer approach, the track vibrations at many positions can be recorded with a limited number of accelerometers and data acquisition channels. In total, the crossing vibrations at 49 positions were recorded, covering the length of six sleeper spans (approximately 3.7 m).

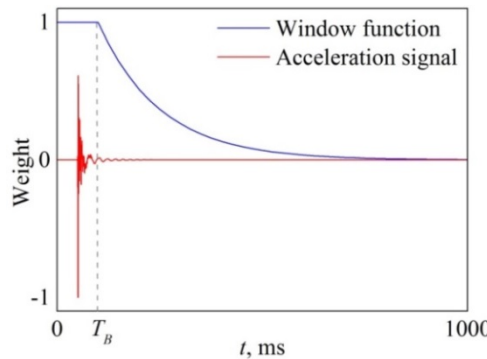


Figure 4.6: Block-exponential window function

To characterize the natural frequencies of the crossing, the measured force signals $F(t)$ and acceleration signals $a(t)$ are transformed into frequency domain via the FFT. To reduce the leakage of the transient-type signals, a block-exponential window [34] is applied during the

transform. Figure 4.6 shows the window function, which is expressed as:

$$w(t) = \begin{cases} 1 & \text{if } t < T_B \\ e^{-(t-T_B)/\tau} & \text{if } t > T_B \end{cases} \quad (5.3)$$

where T_B is the length of the block and τ is the decay rate. Here, the values of T_B and τ are set to 100 ms and 150 ms, respectively.

To minimize the random errors during measurements, the hammer impact was applied four times at each run. Thereafter, the calculated frequency spectra of the force and acceleration are averaged among the four impacts, so that the FRF $H(f)$ is determined by [34]:

$$H_1(f) = \frac{\sum_{i=1}^4 S_{aF}^i(f)}{\sum_{i=1}^4 S_{FF}^i(f)} \quad (4.4)$$

$$H_2(f) = \frac{\sum_{i=1}^4 S_{aa}^i(f)}{\sum_{i=1}^4 S_{aF}^i(f)} \quad (4.5)$$

where f is the frequency, i is the impact number at each run, $S_{aF}^i(f)$ is the cross-spectrum between the force and the acceleration, $S_{FF}^i(f)$ is the auto-spectrum of the force and $S_{aa}^i(f)$ is the auto-spectrum of the acceleration. Under ideal conditions, Equations (4.4) and (4.5) should provide the same results. Yet, the quality of the calculated frequency response function is affected by several factors, such as the response curve of the hammer. Therefore, the coherence function $\gamma^2(f)$ is calculated to evaluate the quality of the analysis:

$$\gamma^2(f) = \frac{H_1(f)}{H_2(f)} \quad (4.6)$$

where $\gamma^2 \in [0,1]$. High value of γ^2 corresponds to high quality. In general, the analysis is regarded as high qualified if the value of γ^2 is above 0.9.

4.3 ABA SIGNALS AT VARIOUS TEST CONDITIONS

ABA measurements were performed at a crossing with various train speeds, moving directions (facing and trailing direction with respect to the crossing) and sensor positions (leading and rear wheels in a bogie) so that their influence on the characteristics of ABA could be determined. In each test scenario (Table 4.1), measurements were conducted several times to confirm the repeatability of the ABA signals.

4.3.1 TRAIN SPEED

In this section, we compare the ABA signals acquired at 28 and 36 km/h. During the measurements, the train ran over the crossing in the facing direction (from closure to crossing nose) and the ABA signals were recorded at the rear wheel (Wheel 2 in Figure 4.3(b)) to avoid disturbance from non-identical test conditions. The ABA signals acquired from the leading wheel and in the trailing direction will be analysed in later sections.

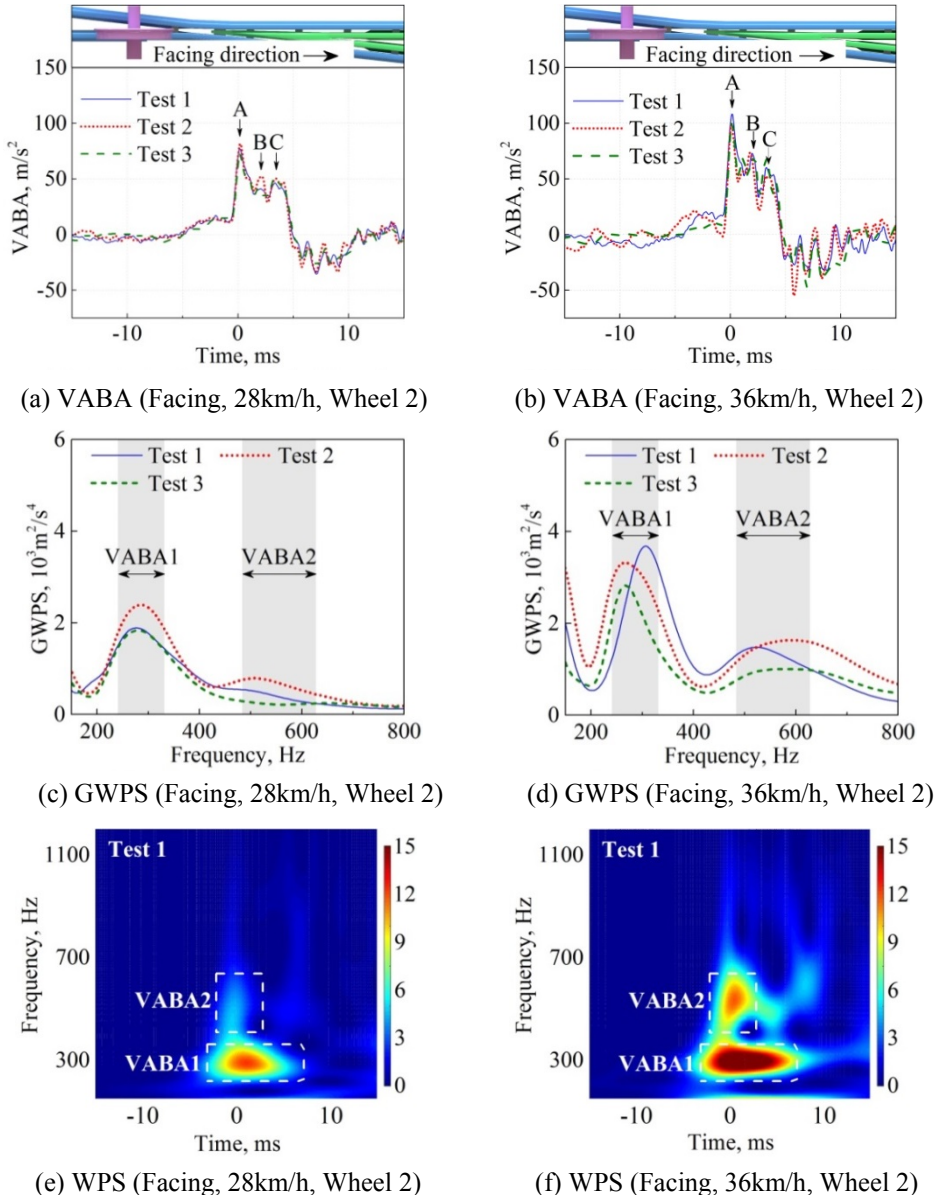


Figure 4.7: VABA acquired in the facing direction. The signals were from the rear wheel. The boxes marked VABA1 and VABA2 indicate the major frequency bands of VABA at 265-305 and 510-600 Hz.

Figure 4.7(a)-(b) shows the vertical ABA (VABA) acquired in the facing direction. In the figure, the origin of the abscissa aligns with the crest of the first major peak, denoted by arrow A. At both train speeds, the waveforms and amplitudes of the ABA signals acquired from the various tests were generally consistent, demonstrating the repeatability of the ABA

measurements. Minor deviations between tests can likely be attributed to random features of the vehicle-track interactions such as the hunting oscillation. The waveforms of the VABA are similar at speeds of 28 and 36 km/h. The amplitude of the VABA, however, increases with train speed. For example, the amplitudes at arrows A, B and C increased by 30-77%.

Figure 4.7(c)-(d) shows the GWPS of the VABA acquired in the facing direction. The GWPS was calculated from the ABA signals between -28 ms and 28 ms (which is equal to the rolling distance of 436 mm at 28 km/h and 560 mm at 36 km/h) to reduce disturbance from vibrations other than those from the wheel/rail impact. The frequencies of interest were between 150-800 Hz for two reasons. First, the low-frequency components below 150 Hz are mainly relevant to the properties of the track substructure components (e.g., subgrade and ballast) rather than the crossing rails. Second, the high-frequency components above 800 Hz have much lower energy than the lower-frequency components, making them less visible at the same scale. At 28 and 36 km/h, the major frequency bands of VABA occurred at 265-305 Hz and 510-600 Hz, indicating that they are not greatly affected by variations in train speed. However, the energy concentrated in these frequency bands increased with the train speed. For example, the GWPS increased by approximately 54-60% for the first major frequency band and by approximately 93-107% for the second major frequency band.

Previous studies of plain tracks have shown that variations in train speed generally influence the vibration energy at the major frequencies of the ABA, rather than the major frequencies themselves [10]. The study in [10] indicated that the major frequencies of VABA at squats (300 and 1060 Hz) are rarely affected by train speed (from 20 to 140 km/h). Based on hammer test measurements and numerical simulations, the authors showed that the major frequencies of the VABA at squats correspond to the natural response of the plain track structure [10]. Therefore, we infer that the major frequency bands of the VABA at crossings are also related to the natural response of the structure, which will be examined in Section 4.4.

Based on the analysis in Section 4.3.1, we suggest that train speed affects the characteristic VABA in the following ways:

- In the facing moving direction, variations in the train speed do not strongly influence the major frequency bands of the VABA at 265-305 and 510-600 Hz.
- The amplitude of the VABA and vibration energy concentrated at the major frequency bands increase with train speed.

4.3.2 TRAIN MOVING DIRECTION

Figure 4.8 shows the VABA acquired in the trailing direction. The waveform (Figure 4.7(a)-(b)) and the major frequency bands (Figure 4.8(c)-(d)) of the VABA are not strongly affected by variations in train speed, whereas the amplitude of the major peak (arrows D, E and F in Figure 4.8(a)-(b)) and the vibration energy increase with train speed. For example, the GWPS increased by 127-165% at the first major frequency band and by 73-83% at the second major frequency band when the train speed increased from 28 to 36 km/h.

Comparing Figure 4.8 to Figure 4.7, the major frequency bands of the VABA occurred at 265-305 Hz and 510-600 Hz in the facing direction (Figure 4.7), while they shifted slightly to 240-290 Hz and 505-545 Hz in the trailing direction (Figure 4.8). The slight shift in the major frequency bands between the two moving directions can be attributed to different wheel-rail

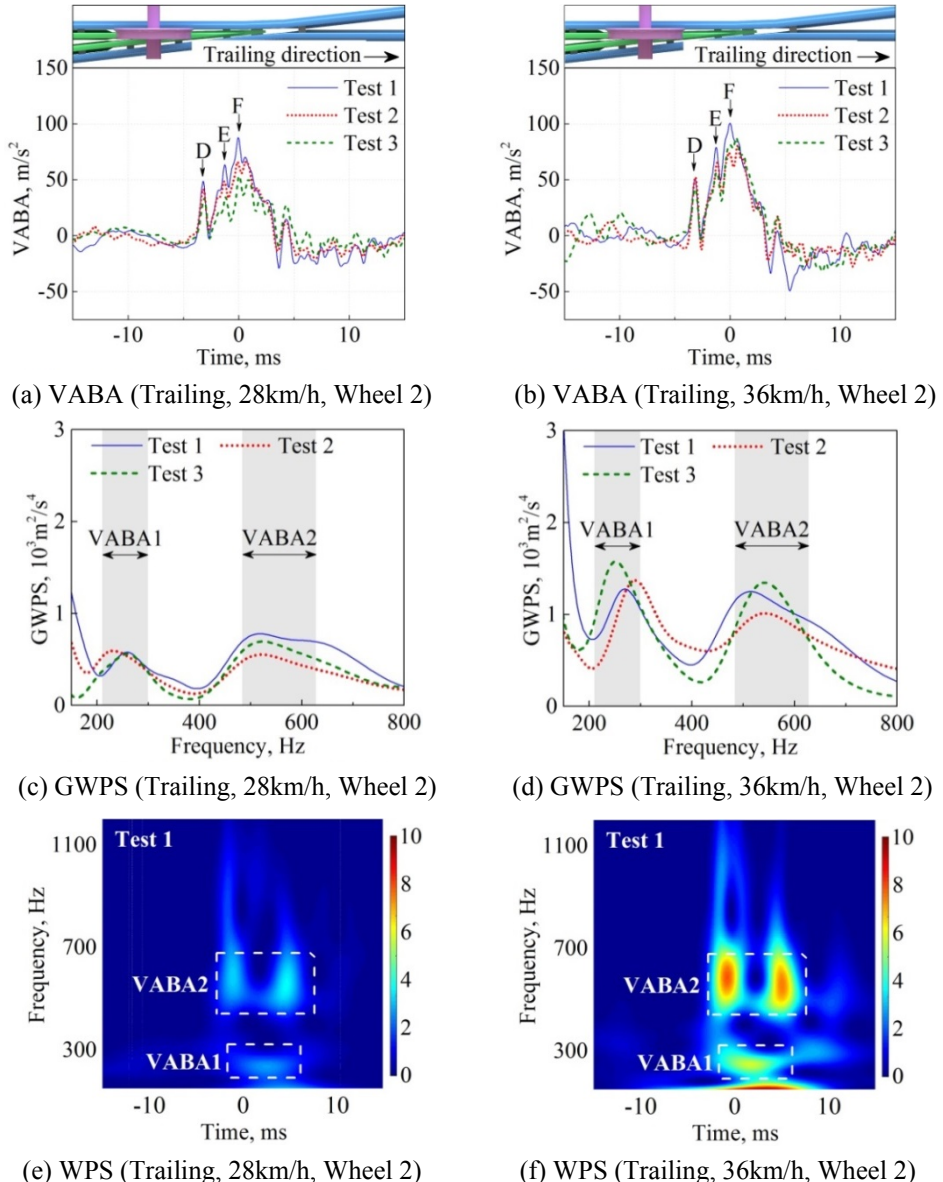


Figure 4.8: VABA acquired in the trailing direction. The signals were from the rear wheel. The boxes marked VABA1 and VABA2 indicate the major frequency bands of VABA at 240-290 and 505-545 Hz, respectively.

impact positions. That is, the wheel impacts the crossing nose in the facing direction but the wing rail in the trailing direction. Consequently, the dynamic response of the system, which is influenced by the impact position [35], differs between the two directions. In addition, the

energy at the major frequency bands depends on the moving direction. At the first major frequency band, the GWPS in the facing direction (Figure 4.7(c)-(d)) increased by 129-227% compared to the value in the trailing direction (Figure 4.8(c)-(d)).

Based on the analysis in Section 4.3.2, we suggest that the moving direction influences the characteristic VABA in the following ways:

- The moving direction does not significantly affect the major frequency bands of VABA; these occur at 265-305 Hz and 510-600 Hz in the facing direction and 240-290 Hz and 505-545 Hz in the trailing direction.
- The energy concentrated at the major frequency bands of the VABA depends on the moving direction. In general, facing motion is associated with greater vibration energy compared to trailing motion.

4

4.3.3 SENSOR POSITION

In the ABA system, accelerometers were mounted on both wheels 1 and 2 (see Figure 4.3(b)). The difference between the two wheels is that Wheel 1 is the leading wheel in the facing direction, running over the crossing ahead of Wheel 2; in contrast, Wheel 2 becomes the leading wheel in the trailing direction. In this section, we compare the VABA acquired from wheels 1 and 2.

Figure 4.9 shows the VABA acquired from Wheel 1 at 36 km/h. The two major frequency bands of the VABA occurred at 275-285 Hz and 530-620 Hz, respectively. Comparing Figure 4.9(b) to Figure 4.7(d), the major frequency bands are generally consistent between wheels 1 and 2 (these occurred at 265-305 Hz and 520-590 Hz for Wheel 2). However, the leading wheel (Wheel 1) generally had a larger amplitude and higher vibration energy. For example, at arrow A, the amplitude of the VABA for Wheel 1 (130-146 m/s² in Figure 4.9(a)) was 30-35% larger than the amplitude for Wheel 2 (100-108 m/s² in Figure 4.7(b)). As another example, at the first major frequency band, the GWPS from Wheel 1 increased by 21-32% compared to Wheel 2. Deviations in the amplitude, vibration energy and major frequency bands of the VABA between the two wheels can be explained by randomness associated with the wheel-rail interactions (e.g., the hunting oscillation), as well as the different loading conditions. When the rear wheel (Wheel 2) impacts the crossing nose, the latter is pre-loaded by the leading wheel (Wheel 1), thus changing the mass participating in the structural vibrations and the stiffness of the system (e.g., the railpad and voided ballast [36]).

Based on the analysis in Section 4.3.3, we suggest that the sensor position has the following effects on the characteristic VABA:

- The different sensor positions do not significantly affect the two major frequency bands of the VABA, which occurred at 275-285 Hz and 530-620 Hz for the leading wheel and 265-305 Hz and 520-590 Hz for the rear wheel.
- The leading wheel is associated with a larger VABA amplitude and greater vibration energy.

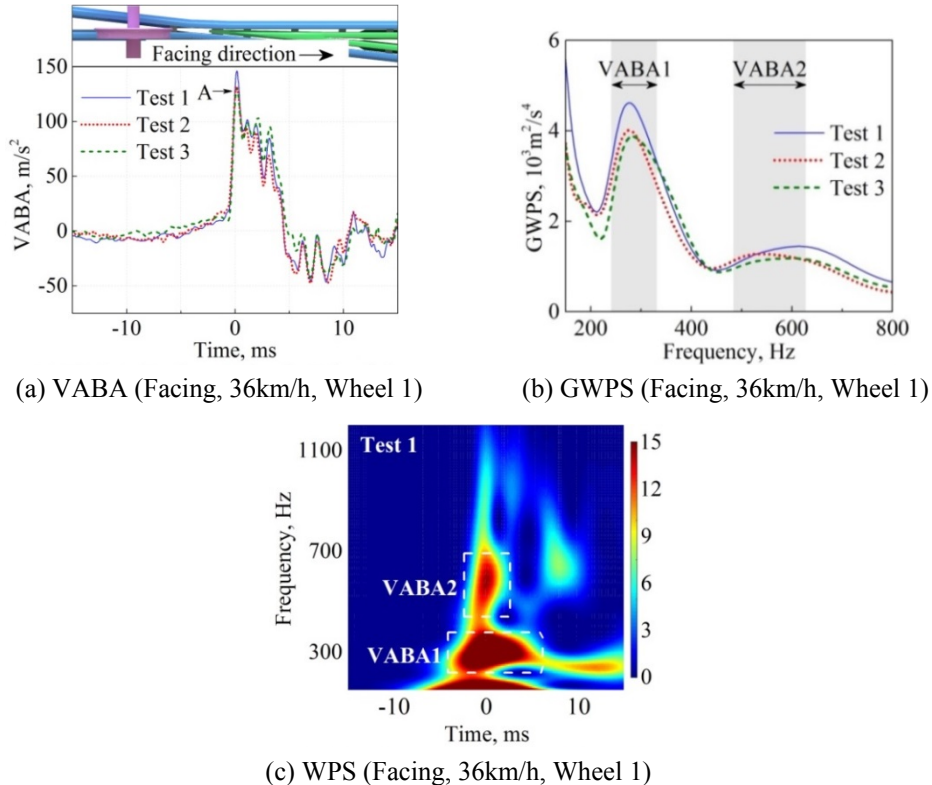


Figure 4.9: VABA from the leading wheel. The signals were acquired in facing direction with the train speed of 36 km/h. The boxes marked VABA1 and VABA2 indicate the major frequency bands of VABA at 275-285 and 530-620 Hz.

4.3.4 CHARACTERISTICS OF LONGITUDINAL ABA

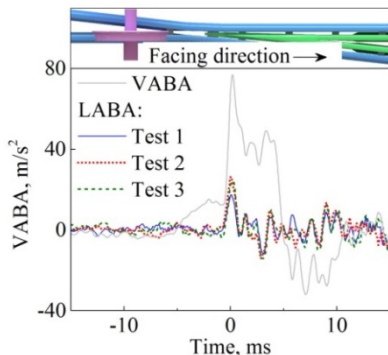
As illustrated in [7], the longitudinal ABA (LABA) is more sensitive to minor rail defects (e.g., light squats) than the VABA. The hit rate for detecting light defects can be improved by combining the LABA and VABA. Therefore, a better understanding of the characteristics of the LABA and its relationship to the VABA will help with condition monitoring of crossings. In this section, we analyse the characteristics of the LABA.

Figure 4.10(a)-(b) compares the LABA and VABA. The maximum amplitude of the LABA was 67-76% smaller than the VABA in the facing direction and 58-72% smaller in the trailing direction. In addition, the variations in the LABA and VABA are not synchronized. For example, Figure 4.10(b) shows that the maximum LABA (arrow B) occurred prior to the maximum VABA (arrow A). Similar out-of-sync variations of the normal and longitudinal contact forces at crossings were discussed in [37]. The study indicated that this behaviour can be attributed to the complex wheel-rail contact geometry and the evolution of the two-point contact (with one contact patch on the wing rail and the other on the crossing nose). Since the ABA is related to the contact force at the wheel/rail interface, the same rationale could explain the out-of-sync variations in the LABA and VABA.

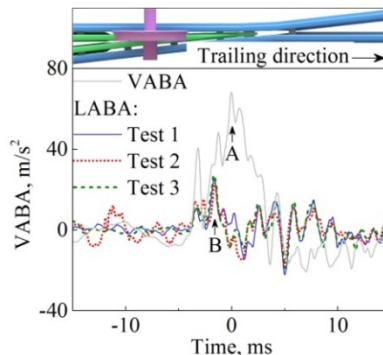
Figure 4.10(c)-(d) compares the GWPS of the LABA and VABA. The major frequency bands of the LABA occurred at 205-215 and 500-540 Hz in the facing direction and at 200-210 and 540-560 Hz in the trailing direction. Therefore, as with the VABA, the moving direction does not significantly affect the major frequency bands of the LABA (Figures 4.7 and 4.8).

Figure 4.11 compares the GWPS of the LABA between 28 and 36 km/h. As shown, variations in train speed do not strongly affect the major frequency bands of the LABA. In addition, the energy at the major frequency bands of the LABA increases with train speed. For example, the GWPS of the LABA increased by 111-138% at the first major frequency band and by 65-133% at the second major frequency band.

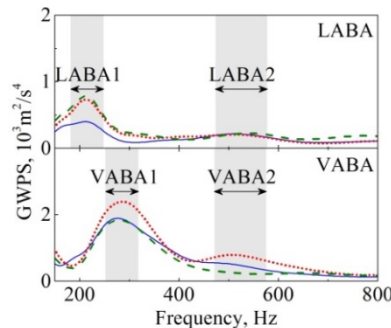
4



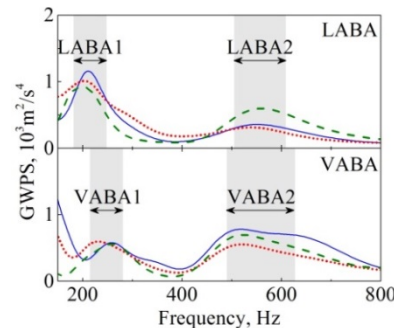
(a) LABA (Facing, 28km/h, Wheel 2)



(b) LABA (Trailing, 36km/h, Wheel 1)



(c) GWPS (Facing, 28km/h, Wheel 2)



(d) GWPS (Trailing, 28km/h, Wheel 1)

Figure 4.10: Comparison between the LABA and VABA. The signals were acquired from the rear wheel at 28 km/h. VABA1 and VABA2 indicate major frequency bands of VABA, while LABA1 and LABA2 indicate major frequency bands of LABA.

Based on the preceding analysis, we conclude the following regarding the characteristics of the LABA:

- The major frequency bands of the LABA, which occurred at 205-215 Hz and 500-540 Hz in the facing direction and at 200-210 Hz and 540-560 Hz in the trailing direction, are not strongly affected by the moving direction.

- Variations in train speed significantly affect the vibration energy at the major frequency bands of the LABA rather than the major frequency bands themselves, similar to the VABA.

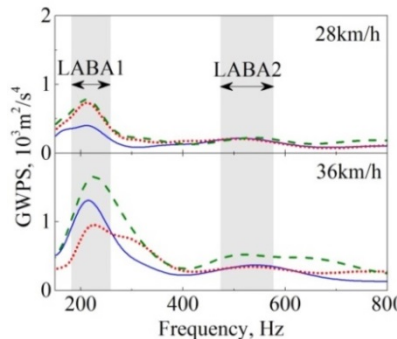


Figure 4.11: GWPS of LABA in the facing direction. The signals were acquired from the rear wheel. LABA1 and LABA2 indicate the major frequency bands of the LABA.

4

4.4 RELATION BETWEEN ABA AND CROSSING NATURAL RESPONSE

Previous studies have shown that the characteristic frequencies of the VABA correspond to the natural frequencies of plain track structures [10]. Since various types of crossings may have different natural behavior, it is important to understand the natural response of crossings to calibrate and improve the ABA system.

The natural response of the crossing was determined based on the roving-accelerometer hammer test measurements (see Figure 4.5(b)). Figure 4.12 shows examples of the impact force and acceleration signals for Tests 1-7. The starting point of the hammer impact was aligned to 50 ms, as denoted by the dashed line (---). In all tests, the impact force had a duration of approximately 2 ms and an amplitude of approximately 25 kN. Since it takes time for vibration energy to propagate from the impact position to the sensor position, the response of the crossing rail was delayed with respect to the dashed line. The delay time varied among the accelerometers depending on the distance between the impact position and the sensor position. For example, the delay time for Tests 1 and 7 was much longer than that for Tests 3 and 4 (see Figure 4.12).

The acceleration function was calculated using equation (4.4). To highlight the global nature of the structure, the acceleration function calculated from accelerometers S1-S4 was averaged (Figure 4.13(a)). Accelerometers S1-S4 were located on the top of the crossing nose and near the impact position (Figure 4.5(b)). Figure 4.13(b) shows the coherence for accelerometers S1-S4. At the frequencies of interest (150-800 Hz), the coherence was greater than 0.97, demonstrating the reliability of the hammer test.

Figure 4.13(a) shows that four natural frequencies of the crossing, namely, 265, 490, 548 and 621 Hz, are dominant at 150-800 Hz. Comparing the major frequency bands of the VABA (240-305 and 510-620 Hz in Figures 4.6-4.8) to the natural frequencies of the crossing demonstrates that the crossing natural frequency of 265 Hz is near the first major VABA frequency band of 240-305 Hz. In addition, the crossing natural frequencies at 490, 548 and

621 Hz are near the second major VABA frequency band of 510-620 Hz. The major frequency band of the VABA and the natural frequencies of the crossing are not exactly the same, likely due to the different loading conditions. The crossing was pre-loaded by vehicles during the ABA measurements, but this pre-loading was absent in the hammer tests. The wheel and hammer may not have impacted at precisely the same position, which could also affect the FRF.

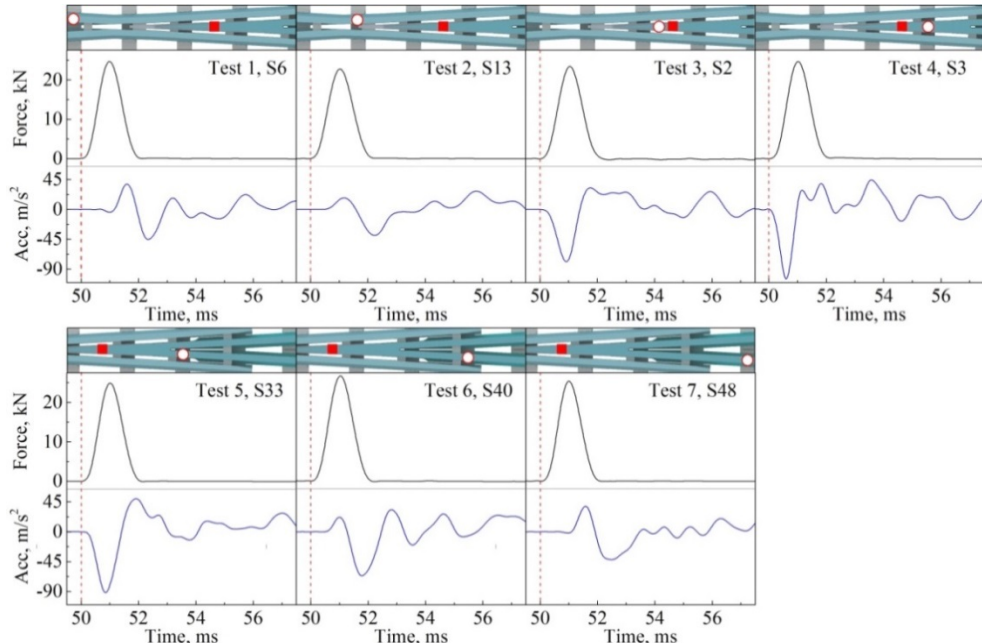


Figure 4.12: Examples of the impact force and acceleration signals. The symbols (■) and (○) indicate the impact position and the sensor position. The dashed line (—) indicates the beginning of the hammer impact at 50 ms.

To gain insight into the dynamics of the crossing, the operational deflection shapes (ODSs) were analysed. The ODSs are the spatial representation of the FRF at each frequency [38]. Both mode shapes and ODSs are commonly used to determine the dynamic behaviour of a structure. In this study, we analysed the ODSs rather than the mode shapes because the ODSs can be measured directly and do not depend on post-processing parameters [39]. In contrast, the mode shapes are obtained via curve-fitting; thus, their accuracy is influenced by the parameter settings.

Figure 4.14 shows the ODSs of crossing rails (including the closure rail, wing rail and crossing nose) at two phases: where the impact force was the maximum (Figure 4.14(a)) and where it reached zero (Figure 4.14(b)). The figure demonstrates that lower natural frequencies generally correspond to longer ODS wavelengths. At all the natural frequencies examined, the vibrations of the crossing rails were dominated by bending. However, the vibrations are not solely derived from bending because the vibrations of two wing rails were not synchronized, as shown by arrows W1 and W2. We suggest that the vibrations of the crossing rails are a combination of bending and torsion, which is common for asymmetric structures.

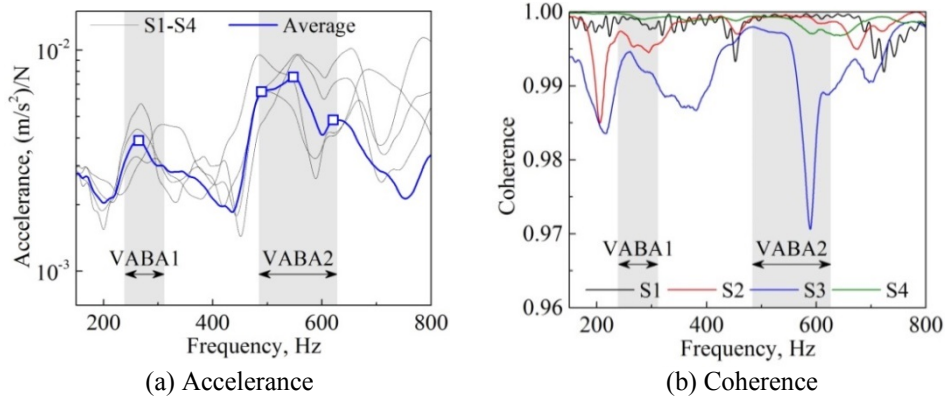


Figure 4.13: Frequency response function. The rectangles (□) indicate the natural frequencies of the crossing at 265, 490, 548 and 621 Hz. VABA1 and VABA2 indicate the major frequency bands of the VABA at 240-305 and 510-620 Hz.

4

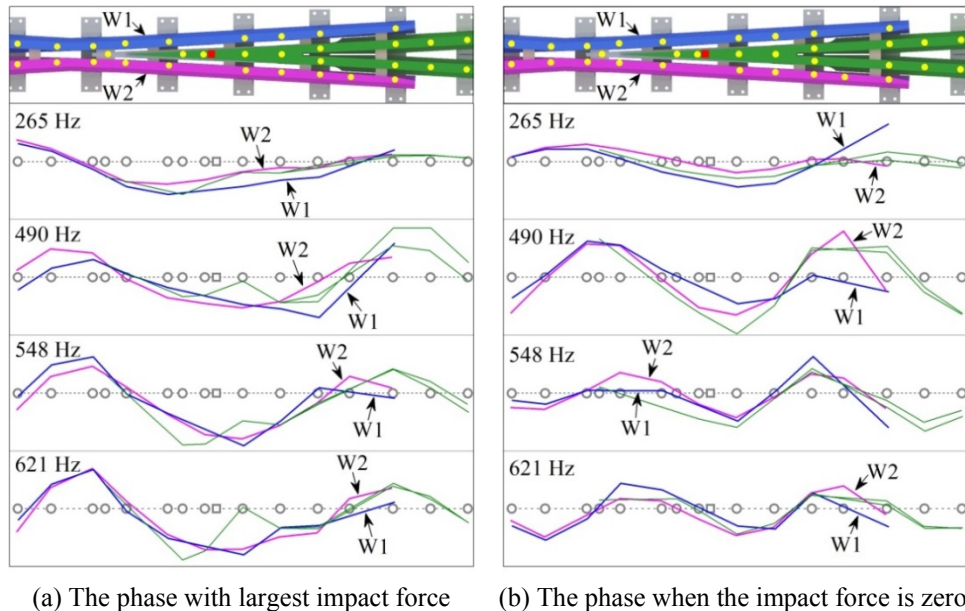


Figure 4.14: ODSs of crossing rails at the crossing natural frequencies of 265, 490, 548 and 621 Hz. The circles (○) indicate the sensor positions and the rectangles (□) indicate the impact position. The arrows marked W1 and W2 indicate the non-synchronized vibrations of the two wing rails.

In Figure 4.14, the maximum amplitude of the ODSs in a full vibration cycle may not occur at the two specified phases. Therefore, Figure 4.15 shows the ODSs of the crossing nose over a full vibration cycle to analyse how their shape and amplitude evolves. In the figure, the ODSs at 60 phases of a vibration cycle are shown. At the natural frequency of 265 Hz, the ODS amplitude is smaller than the amplitudes at higher natural frequencies. This phenomenon

likely occurs because of differences in the effective mass participating in the structural vibration. The mass of the system commonly participates less in structural vibrations at higher frequencies. With the normalized impact force, the amplitudes of the ODSs tend to be larger at higher frequencies. After the crossing nose divides into two separate pieces, the two pieces vibrate with different amplitudes, at 490 and 548 Hz, as indicated by the arrows N1 and N2. This behavior suggests that the vibrations of the crossing nose also arise from a combination of bending and torsion rather than pure bending.

4

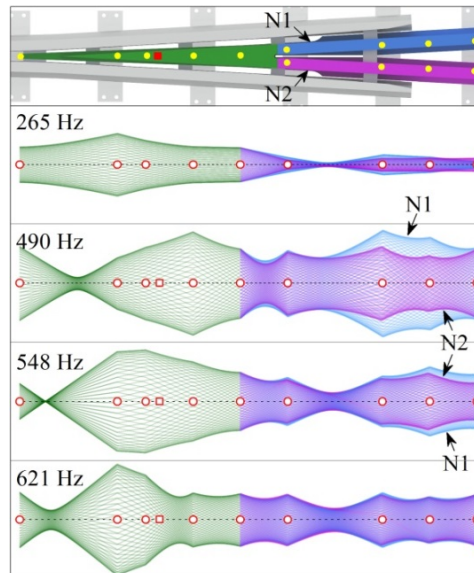


Figure 4.15: ODSs of the crossing nose at 60 phases of a full vibration cycle. The ODSs are symmetric about the stationary state, i.e., the dashed line (---). The circles (○) indicates the sensor positions and the rectangles (□) indicate the impact positions. Arrows N1 and N2 indicate the non-identical vibration amplitudes of the two pieces of the crossing nose.

In summary, the major frequency bands of the VABA (240-305 and 510-620 Hz) are related to the crossing natural frequencies (265, 490, 548 and 621 Hz). As a consequence, variations in train speed, train moving direction and sensor position do not significantly affect the major frequency bands of the VABA. In addition, the vibrations of crossing rails at the major frequency bands of the VABA are a combination of bending and torsion rather than pure bending, because the vibrations of the two wing rails are not synchronized.

The natural response of the track structure discussed in this section was determined using the 54E1-1:9 crossing type. Since there are several crossing types on the Dutch railway network, it is important to characterize the natural behavior for each crossing type via in-situ hammer test measurements. Because access to these crossings is limited by the safety regulations of the railway authority, we were only allowed to perform in-situ measurements at a single crossing. The natural response of crossings could also be analyzed using numerical simulations [29], which might allow for easier determination of the natural responses of various crossing types and their relationships to the ABA.

4.5 SUMMARY

In this chapter, the characteristics of ABA at a railway crossing is analysed under various test conditions. These conditions included the train speed, moving direction (facing and trailing directions with respect to the crossing) and sensor position (leading and rear wheels of a bogie), as these factors can influence the monitoring results of the ABA system. In addition, in-situ hammer test measurements were conducted to address the relationship between the major frequencies of the ABA and the crossing natural response. We draw the following conclusions from the results of this study:

- The correlation between the ABA and hammer test measurements indicates that the major frequency bands of the VABA at 240-305 and 505-620 Hz are related to the natural frequencies of the crossing at 265, 490, 548 and 621 Hz. Therefore, the major frequency bands of the VABA are not greatly affected by variations in train speed, moving direction or sensor position.
- The amplitude of the VABA and the energy concentrated at the major frequency bands depend on train speed, moving direction and sensor position. In particular, higher vibration energy occurs at faster train speeds, along the facing moving direction and from the leading wheel.
- At the characteristic frequency bands of the VABA, the vibrations of the crossing rails are a combination of bending and torsion rather than pure bending, because the vibrations of the two wing rails are not synchronized.
- Variations in train speed and moving direction do not significantly affect the major frequency bands of the LABA, which are similar to those of the VABA.

REFERENCES

- [1] S. Alfi, S. Bruni, *Mathematical modelling of train–turnout interaction*, Vehicle System Dynamics **47**, 551-574 (2009).
- [2] C. Wan, V. Markine, I. Shevtsov, *Improvement of vehicle–turnout interaction by optimising the shape of crossing nose*, Vehicle System Dynamics **52**, 1517-1540 (2014).
- [3] R.S. Edwards, S. Dixon, X. Jian, *Characterisation of defects in the railhead using ultrasonic surface waves*, NDT & E International **39**, 468-475 (2006).
- [4] M.P. Papaelias, C. Roberts, C. Davis, *A review on non-destructive evaluation of rails: state-of-the-art and future development*, Proceedings of the Institution of Mechanical Engineers, Part F: Journal of Rail and rapid transit **222**, 367-384 (2008).
- [5] M. Boccilone, A. Caprioli, A. Cigada, A. Collina, *A measurement system for quick rail inspection and effective track maintenance strategy*, Mechanical Systems and Signal Processing **21**, 1242-1254 (2007).
- [6] S. Alfi, S. Bruni, *Estimation of long wavelength track irregularities from on board measurement*, in *4th International Conference on Railway Condition Monitoring* (Derby, UK, 2008), pp. 1-6.

4

- [7] M. Molodova, Z. Li, A. Núñez, R. Dollevoet, *Automatic Detection of Squats in Railway Infrastructure*, IEEE Transactions on Intelligent Transportation Systems **15**, 1980-1990 (2014).
- [8] M. Molodova, Z. Li, R. Dollevoet, *Axle box acceleration: Measurement and simulation for detection of short track defects*, Wear **271**, 349-356 (2011).
- [9] M. Molodova, M. Oregui, A. Núñez, Z. Li, R. Dollevoet, *Health condition monitoring of insulated joints based on axle box acceleration measurements*, Engineering Structures **123**, 225-235 (2016).
- [10] M. Molodova, Z. Li, A. Nunez, R. Dollevoet, *Parameter study of the axle box acceleration at squats*, Proceedings of the Institution of Mechanical Engineers, Part F: Journal of Rail and Rapid Transit **229**, 841-851 (2014).
- [11] C.P. Ward, P. Weston, E. Stewart, H. Li, R.M. Goodall, C. Roberts, T. Mei, G. Charles, R. Dixon, *Condition monitoring opportunities using vehicle-based sensors*, Proceedings of the Institution of Mechanical Engineers, Part F: Journal of Rail and Rapid Transit **225**, 202-218 (2011).
- [12] S. Kaewunruen, *Monitoring structural deterioration of railway turnout systems via dynamic wheel/rail interaction*, Case Studies in Nondestructive Testing and Evaluation **1**, 19-24 (2014).
- [13] P. Salvador, V. Naranjo, R. Insa, P. Teixeira, *Axlebox accelerations: Their acquisition and time-frequency characterisation for railway track monitoring purposes*, Measurement **82**, 301-312 (2016).
- [14] E. Kassa, J.C. Nielsen, *Dynamic interaction between train and railway turnout: full-scale field test and validation of simulation models*, Vehicle System Dynamics **46**, 521-534 (2008).
- [15] D. Gabor, *Theory of communication. Part 1: The analysis of information*, Journal of the Institution of Electrical Engineers-Part III: Radio and Communication Engineering **93**, 429-441 (1946).
- [16] M. Vetterli, J. Kovacevic, *Wavelets and subband coding* (Prentice-Hall, 1995).
- [17] J. Ville, *Théorie et applications de la notion de signal analytique*, Cables et transmission **2**, 61-74 (1948).
- [18] I. Daubechies, J. Lu, H-T. Wu, *Synchrosqueezed wavelet transforms: An empirical mode decomposition-like tool*, Applied and Computational Harmonic Analysis **30**, 243-261 (2011).
- [19] N. Huang, Z. Shen, S. Long, M. Wu, H. Shih, Q. Zheng, et al., *The empirical mode decomposition and the Hilbert spectrum for nonlinear and non-stationary time series analysis*, Proceedings of the Royal Society of London A: mathematical, physical and engineering sciences **454**, 903-995 (1998).
- [20] A. Garinei, G. Risitano, L. Scappaticci, F. Castellani, *An optimized method to evaluate the performance of trench isolation for railway-induced vibration*, Measurement **94**, 92-102 (2016).
- [21] Z. Li, M. Molodova, A. Núñez, R. Dollevoet, *Improvements in axle box acceleration measurements for the detection of light squats in railway infrastructure*, IEEE Transactions on Industrial Electronics **62**, 4385-4397 (2015).

[22] A. Grinsted, J.C. Moore, S. Jevrejeva, *Application of the cross wavelet transform and wavelet coherence to geophysical time series*, Nonlinear processes in geophysics **11**, 561-566 (2004).

[23] C.A. Ribeiro, R. Calçada, R. Delgado, *Experimental assessment of the dynamic behaviour of the train-track system at a culvert transition zone*, Engineering Structures **138**, 215-228 (2017).

[24] M. Oregui, Z. Li, R. Dollevoet, *An investigation into the modeling of railway fastening*, International Journal of Mechanical Sciences **92**, 1-11 (2015).

[25] K. Knothe, Y. Wu, *Receptance behaviour of railway track and subgrade*, Archive of Applied Mechanics **68**, 457-470 (1998).

[26] S. Kaewunruen, A.M. Remennikov, *Progressive failure of prestressed concrete sleepers under multiple high-intensity impact loads*, Engineering Structures **31**, 2460-2473 (2009).

[27] J. Smutny, *Measurement and analysis of dynamic and acoustic parameters of rail fastening*, NDT & E International **37**, 119-129 (2004).

[28] A.P. de Man, *DYNATRACK: A survey of dynamic railway track properties and their quality*, PhD dissertation, Delft University of Technology (2007).

[29] M. Oregui, Z. Li, R. Dollevoet, *An investigation into the vertical dynamics of tracks with monoblock sleepers with a 3D finite-element model*, Proceedings of the Institution of Mechanical Engineers, Part F: Journal of Rail and Rapid Transit **230**, 891-908 (2015).

[30] N. Vincent, D.J. Thompson, *Track dynamic behaviour at high frequencies. Part 2: experimental results and comparisons with theory*, Vehicle System Dynamics **24**, 100-114 (1995).

[31] M. Batel, *Operational modal analysis-another way of doing modal testing*, Sound and Vibration **36**, 22-27 (2002).

[32] S. Gade, N.B. Møller, H. Herlufsen, H. Konstantin-Hansen, *Frequency domain techniques for operational modal analysis*, in *1st International Operational Modal Analysis Conference* (Copenhagen, Denmark, 2005), pp. 261-271.

[33] A. Remennikov, S. Kaewunruen, *Experimental investigation on dynamic railway sleeper/ballast interaction*, Experimental Mechanics **46**, 57-66 (2006).

[34] N. Maia, J. Silva, *Theoretical and experimental modal analysis* (Research Studies Press, 1997).

[35] M. Oregui, Z. Li, R. Dollevoet, *Identification of characteristic frequencies of damaged railway tracks using field hammer test measurements*, Mechanical Systems and Signal Processing **54**, 224-242 (2015).

[36] A. Paixão, E. Fortunato, R. Calçada, *The effect of differential settlements on the dynamic response of the train-track system: A numerical study*, Engineering Structures **88**, 216-224 (2015).

[37] Z. Wei, C. Shen, Z. Li, R. Dollevoet, *Wheel-rail impact at crossings: relating dynamic frictional contact to degradation*, Journal of Computational and Nonlinear Dynamics **12**, 041016 (2017).

[38] B.J. Schwarz, M.H. Richardson, *Introduction to operating deflection shapes*, CSI Reliability Week (Orlando, USA, 1999).

[39] M.H. Richardson, *Is it a mode shape, or an operating deflection shape?* SV Sound and vibration **31**, 54-61 (1997).

5

EVALUATING CROSSING DEGRADATION USING ABA MEASUREMENT

In this chapter, we investigate the capability of an ABA system to evaluate the degradation at railway crossings. For this purpose, information from multiple sensors, namely, ABA signals, 3D rail profiles, GPS and tachometer recordings, was collected from both nominal and degraded crossings. By proper correlation of the gathered data, an algorithm was proposed to distinguish the characteristic ABA related to the degradation and then to evaluate the health condition of crossings. The algorithm was then demonstrated on a crossing with an unknown degradation status, and its capability was verified via a 3D profile measurement. The results indicate that the ABA system is effective at monitoring two types of degradation. The first type is uneven deformation between the wing rail and crossing nose, corresponding to characteristic ABA frequencies of 230-350 and 460-650 Hz. The second type is local irregularity in the longitudinal slope of the crossing nose, corresponding to characteristic ABA frequencies of 460-650 Hz. The types and severity of the degradation can be evaluated by the spatial distribution and energy concentration of the characteristic frequencies of the ABA signals.

This chapter is based on:

Wei Z, Núñez A, Li Z, Dollevoet R. Evaluating degradation at railway crossings using axle box acceleration measurements. Sensors 17 (2017): 2236.

5.1 INTRODUCTION

A railway crossing is one of the fundamental components of track infrastructure because it intersects different tracks at the same level. Figure 5.1 shows a schematic diagram of a crossing. A crossing constitutes a geometric discontinuity (i.e., a gap) between the closure rail and crossing nose such that the clearance of a wheel flange is guaranteed. During the passage of vehicles, high wheel-rail impact forces and undesirable vibrations arise and accelerate degradation at crossings. Crossings account for a large fraction of maintenance and renewal costs in railway systems worldwide. For example, faults associated with switches and crossings in Sweden correspond to over 13% of maintenance costs [1]. On the Dutch railway network, a total of 826 crossings were replaced between 2011 and 2015 [2]. The Dutch railway authority (ProRail) stipulates that severely degraded crossings must be replaced within 24 hours after they are detected, resulting in unpredictable traffic delays in the railway system.

5

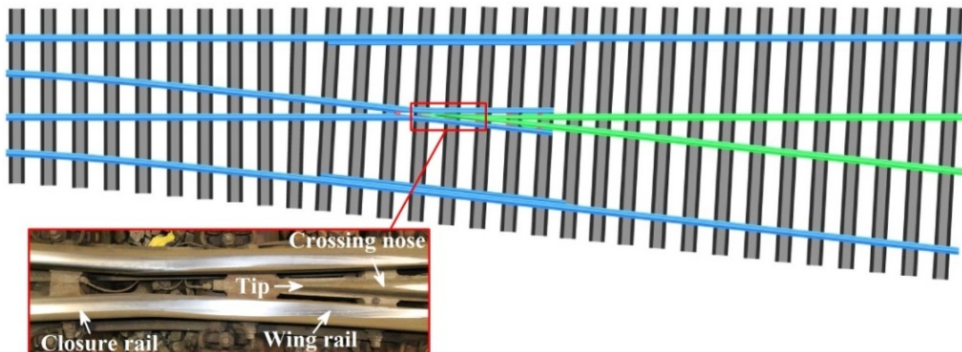


Figure 5.1: Schematic diagram of a railway crossing

Figure 5.2 shows two examples of severe degradation at crossings. Both crossings required urgent replacement due to shelling and squats [3]. If the degradation was to be identified at an early stage when they are local and minimal, preventive maintenance (e.g., grinding and welding) could be performed, and their service life could be extended. Therefore, an effective diagnostic method is required for the prompt detection of degradation at crossings.



(a) Shelling

(b) Squats

Figure 5.2: Examples of severe degradation at crossings

Currently, the monitoring of crossings highly relies on human visual inspection, i.e., technicians visit the tracks or watch videos of tracks to identify degradation. This task is labour-intensive and inefficient, and the detection results may be subjective and erroneous. Consequently, most degraded crossings are reactively replaced when they reach severe degradation. The limitations of manual inspection motivate the development of on-board monitoring technologies, such as ultrasonic measurement [4, 5], eddy current testing [6, 7], magnetic induction [8], image recognition [9-11], vibration-based inspection [12, 13], guided-wave inspection [14], radio detection and ranging sensors [15, 16], thermography [17, 18], acoustic emission systems [19, 20] and ground-penetrating radar [21, 22].

Each of these technologies is adept at detecting certain defects but suffers from certain limitations. Ultrasonic measurement shows the best performance in detecting cracks, whereas it is not adept at detecting surface defects. Eddy current testing is able to detect surface defects. However, the probe in the eddy current system must be positioned at a constant distance from the rail head, making it unavailable at geometric discontinued crossings. The magnetic induction method, which can be used for near-surface or surface transverse defects, also suffers from the restriction of a constant distance between sensors and rail surfaces. The image recognition method can detect visible defects on rail surface and other track components (e.g., loose bolts and moving sleepers), whereas it is adversely affected by illumination inequality and inconsistent reflection properties on plain tracks and by the complex structure and discontinued geometry at crossings. Vibration-based inspection can be used for several purposes, such as monitoring track irregularity and detecting train derailment, whereas some of its applications (such as detecting long wave rail irregularity) require moderate train speeds. Guided-wave inspection is capable of detecting several defect types, such as cracks and corrosion, but is limited by the critical size of defects. Radio detection and ranging sensors are able to detect obstacles endangering railway operation (e.g., moving cars at level crossings). Acoustic emission systems can detect several defects, such as poor track alignment and squats, but its on-board implementation is disturbed by the noise generated by airflow. The thermography method can detect cracks and ballast conditions, but the method is disturbed by fluctuations in weather conditions. Ground-penetrating radar is adept at monitoring track substructure components such as ballast and subgrade. Among the above-mentioned inspection methods, those that can be applied at geometric discontinued crossings (e.g., ultrasonic measurement) are adept at crack detection. Regarding the numerous crossings without cracks yet with significant profile degradation because of plastic deformation and wear, an effective diagnostic method is required for prompt detection.

In this chapter, we investigate the feasibility of the ABA system for the condition monitoring of railway crossings. ABA measurement is a vibration-based inspection method, and its detection algorithm relies on extracting changes in dynamic responses with respect to the nominal condition. On plain tracks, the ABA system has been used to detect isolated defects (e.g., squats [23], poorly qualified welds [24] and worn insulated rail joints [25]) and periodic defects (e.g., corrugation [26-28] and wheel flats [29]).

At railway crossings, the application of the ABA system is more complex because of the complex structure and discontinued geometry. The ABA signals measured at crossings contain information related to both the inherent geometric discontinuity and the undesired defects; thus, the ABA system must be able to identify the characteristic vibrations related to defects [30]. Few studies in the literature have applied an ABA system to crossings [31, 32]. These studies did not distinguish the dynamic responses belonging to different sources, making them

unable to evaluate the type, location and severity of crossing defects.

To overcome the challenges faced in these previous works, this chapter measures both ABA signals and crossing profiles over time and attempts to extract the relationships between the gathered data. With the aid of an interpretation-based approach, the ABA system is potential to estimate the type, location and severity of crossing defects. Figure 5.3 shows the structure of the methodology. Information from multiple sensors, namely, ABA signals, GPS, tachometer recordings and measured 3D profiles, was obtained from reference crossings of the same type with different conditions (both nominal and degraded) to extract the signature vibrations related to crossing degradation.

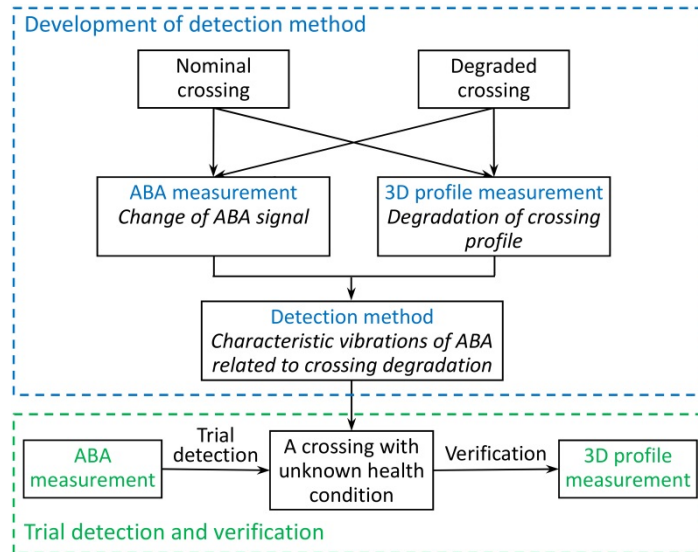


Figure 5.3: Structure of the methodology

This chapter is organized as follows. Section 5.2 presents the ABA and 3D profile measurement systems. Section 5.3 investigates the characteristic vibrations of ABA related to the degradation at a crossing and proposes a detection method. In Section 5.4, ABA measurement is performed on a crossing with an unknown degradation status as a trial, and the detection results are verified using 3D profile measurements and field observations. Section 5.5 discusses the aspects helpful to extend the capability of the ABA system. Finally, Section 5.6 presents conclusions and recommends possible future work.

5.2 ABA AND 3D PROFILE MEASUREMENTS

In this section, in situ ABA and 3D profile measurements were conducted on two reference crossings. The two crossings are of the same type: a 54E1-1:9 type with a UIC54 rail profile and a crossing angle of 1:9. The crossings have different profiles: the first was newly installed and nearly in the nominal state, while the second had been in the track for a long term and had degraded significantly. At both crossings, the train operational speed was limited to 40 km/h, and over 96% of the total traffic loads (approximately 20 million gross tons per year) occurred in the facing direction, namely, from closure rail to crossing nose.

5.2.1 ABA MEASUREMENT

The ABA system is composed of accelerometers, a GPS antenna and a tachometer; see Figure 5.4. The accelerometers are mounted on the axle boxes of the train to measure the vertical ABA signals. The sampling frequency of ABA is set to 25.6 kHz to ensure that sufficient information is captured from the moving sensors over a broad range of measuring speeds. The GPS antenna is installed on the train roof to record the location, and the tachometer is used to record train speed and ensure optimal positioning of the ABA signals.

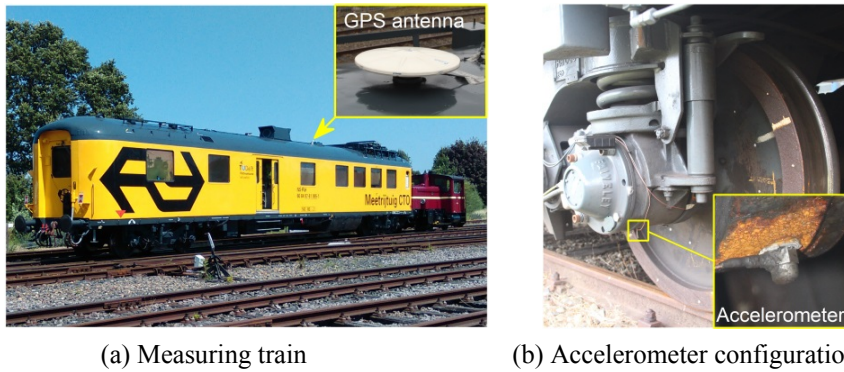


Figure 5.4: Instrumentation of ABA system

When a train passes over ordinary tracks under nominal conditions, the ABA signal fluctuates because of the natural response of the vehicle-track system. The presence of undesired degradation (e.g., poor qualified welds and worn railpads) or intrinsic geometric discontinuity (e.g., crossing and insulated rail joint) can significantly affect the vehicle-track interaction, which is captured in the ABA signal. Figure 5.5(a) shows an example of the measured ABA at a crossing and two adjacent welds, where the origin of the abscissa is aligned with the wheel-crossing impact position. At the crossing and welds, only a minimal difference arises in the amplitudes and durations of the ABA signals; thus, it is not straightforward to first differentiate them and then extract sufficient information to evaluate their degradation condition in the time domain. Consequently, frequency analysis is applied for degradation detection because it can provide crucial information that is challenging to detect in the time domain.

The CWT method has been effectively used to identify the characteristic vibrations of ABA at squats and worn insulated joints [25,32]. With the adjustment of certain parameters, the method can also be used to detect degradation at crossings. Wavelet analysis is used because the signal processing is independent of the window size, making it suitable for investigating the transient processes of brief events [33]. In the CWT, the convolutions of the analysed signal are calculated with a group of scaled and shifted wavelet functions. The wavelet coefficients $W_n(s)$ of the analysed signal x_n can be represented as follows [34]:

$$W_n(s) = \sum_{n'=0}^{N-1} x_{n'} \psi^* \left[\frac{(n'-n)\delta_t}{s} \right] \quad (5.1)$$

where ψ is the mother wavelet [35], s is the wavelet scale, N is the number of points in the time series, $n' = 0, \dots, N - 1$, δ is the time step, n is the continuous variable for the translation and $*$ denotes a complex conjugate.

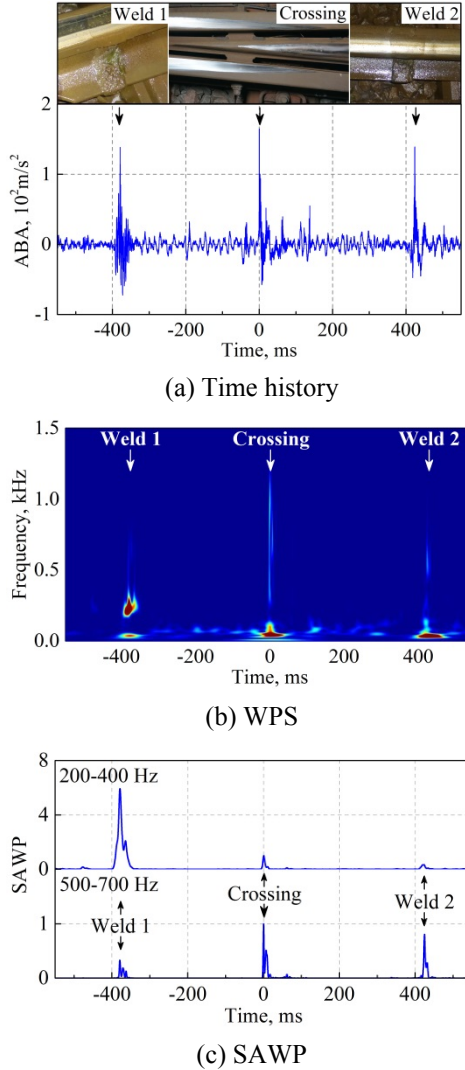


Figure 5.5: An example of the measured ABA at crossing

Figure 5.5(b) is an example of the WPS, which is calculated using the square of the wavelet coefficients $|W_n^2(s)|$. The colour indicates the amount of energy at a certain position (the horizontal axis) and frequency (the vertical axis). In the figure, the crossing and welds correspond to different dynamic responses in terms of the major frequency components and the energy concentration. To achieve improved quantification of the distributions of the WPS in certain frequency bands, the SAWP is calculated. The SAWP is defined as the weighted

sum of the WPS in the frequency band f_1 to f_2 [36]:

$$\bar{W}_n^2[f_1, f_2] = \frac{\delta_j \delta_t}{C_\delta} \sum_{j=f_1}^{f_2} \frac{|W_n(s_j)|^2}{s_j} \quad (5.2)$$

where δ_j is the scale step and C_δ is an empirically derived reconstruction factor. To facilitate the comparison of different scenarios, the SAWP is divided by a constant γ :

$$\bar{W}^2[f_1, f_2] = \frac{\bar{W}_n^2[f_1, f_2]}{\gamma} \quad (5.3)$$

where γ is the value of the SAWP in the nominal state and at the position of wheel-crossing impact.

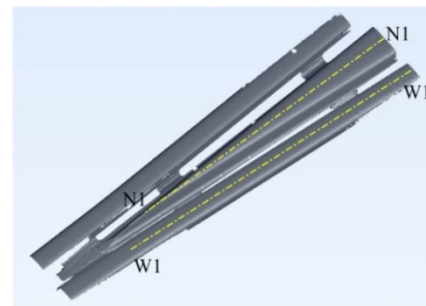
To Figure 5.5(c) shows an example of the SAWP at 200-400 Hz and 500-700 Hz. The two welds correspond to different frequency responses: weld 1 exhibits a large value of $\bar{W}^2[200,400]$ and a small value of $\bar{W}^2[500,700]$, in contrast with the values at weld 2. This information reveals that the two welds feature different degradation conditions. The crossing health condition can also be evaluated by comparing the SAWP of the measured ABA with the value in the nominal state.

5.2.2 3D PROFILE MEASUREMENT

The crossing profile was measured in 3D using the laser-based non-contact apparatus HandyScan; see Figure 5.6(a). In this measurement, the laser stripes project a reference on the rail surface, which is captured by two cameras. The accuracy of HandyScan is 0.03 mm in arbitrary directions. Figure 5.6(b) shows an example of the measured 3D profile.



(a) Measurement using HandyScan



(b) A measured 3D crossing profile

Figure 5.6: 3D profile measurement. Cross-sections W1 and N1 are along the centrelines of the wing rail and crossing nose, respectively.

To gain insight into the measured profile, two longitudinal-vertical cross-sections are selected from the wing rail and crossing nose; see Figure 5.6(b). The cross-sections W1 and N1 are along the centrelines of the wing rail and crossing nose, respectively. Figure 5.7 compares the crossing profile of the nominal and degraded states, where the origin of the abscissa aligns with the tip of the crossing nose. Along W1, the height difference between the

nominal and the degraded profiles reaches the maximum of 0.8 mm at 102 mm. Because of the misalignment of the rolling direction of the wheelset and the centreline of the wing rail, the running band on the wing rail shrinks laterally towards the gauge side, ultimately reaching zero at 305 mm.

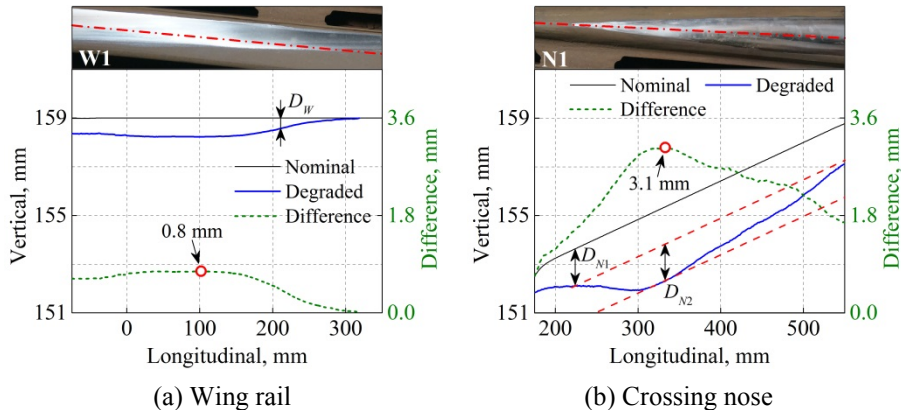


Figure 5.7: Measured crossing profile along W1 and N1. The dot (○) indicates the maximum difference in height between the nominal and degraded states. D_W denotes the difference in the height of the wing rail, while D_{N1} and D_{N2} denote the difference in the height of the crossing nose.

On the crossing nose, wheel-rail contact occurs from 235 mm onward, as indicated by the shiny running band in Figure 5.7(b). In this region, the difference in height between the nominal and degraded state is D_{N1} , which is larger than the difference in the height of the wing rail D_W between the two states. The difference increases along N1 and reaches its maximum of 3.1 mm at 333 mm. Thereafter, the height difference decreases such that the degradation at D_{N2} is more severe than in its surrounding area, leading to local irregularity in the longitudinal slope of the crossing nose.

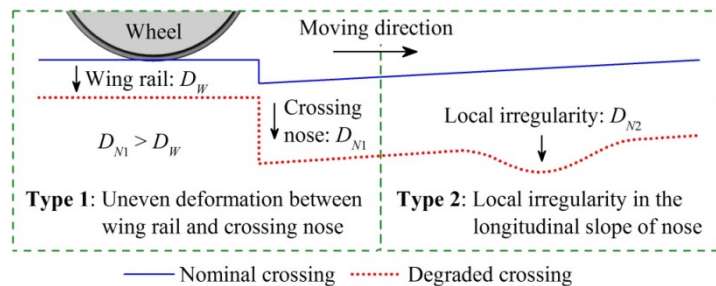


Figure 5.8: Two types of degradation at the measured crossing. D_W denotes the difference in the height of the wing rail, while D_{N1} and D_{N2} denote the difference in the height of the crossing nose.

Based on the measured crossing profiles shown in Figure 5.7, the degradation at the measured crossing can be divided into two types, as illustrated in Figure 5.8. The first type is

the uneven deformation between the wing rail and the crossing nose (i.e., $D_{N1} > D_W$ in Figure 5.7), which is caused by the dominance of the facing motion of vehicles and the related large impact forces and stresses on the crossing nose. The second type is the local irregularity in the longitudinal slope of the crossing nose (i.e., D_{N2} in Figure 5.7(b)). This local irregularity is caused by the complex crossing geometry and the related non-identical distributions of the plastic deformation and wear on the crossing nose [37].

5.3 CHARACTERISTICS OF ABA RELATED TO MEASURED CROSSING DEGRADATION

The characteristic vibrations of ABA related to the degradation are extracted by comparing the measured ABA and 3D profiles of nominal and degraded crossings. With this information, an algorithm capable of detecting crossing degradation is proposed.

5.3.1 REPEATABILITY OF MEASURED ABA

To demonstrate the repeatability of the measured ABA, the measurements were performed three times using the same train at the nominal crossing. In each measurement, the train passed over the crossing at a speed of 26-28 km/h in the facing direction.

Figure 5.9(a) compares the ABA signals of the measurements, where the origin of the abscissa is aligned with the crest of the first major peak, as indicated by arrow A. In general, these ABA signals coincide well with each other in terms of the waveform and amplitude of major peaks. There are three major peaks in all the signals, denoted by arrows A, B and C. The dispersion in the amplitudes at arrows A, B and C are up to 12%, 23% and 10% among the measurements. The dispersion is mainly attributed to the randomness of vehicle-track interaction, for example, the hunting oscillation. Relative to the amplitudes, the wavelengths of the three peaks are in closer agreement among the measurements. Because the wavelengths are relevant to the frequency components of ABA, the frequency components are preferred for evaluating crossing degradation.

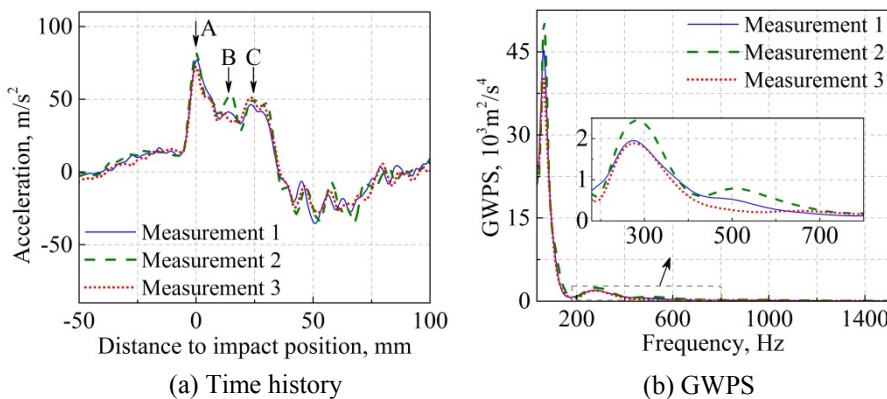


Figure 5.9: Measured ABA at the nominal crossing

Figure 5.9(b) compares the GWPS of ABA, defined as WPS averaged over the location at each frequency [36]. In the figure, the time history of ABA distributed between -28 and 28 ms

is analysed to reduce the disturbance of vibrations far from the wheel-crossing impact. In general, satisfactory agreement can be achieved in terms of the major frequency components of ABA. The most dominant frequency occurs at approximately 65 Hz, while higher-frequency components of approximately 270 and 520 Hz can also be observed, albeit with much lower energy. High vibration energy is concentrated in the low-frequency range for the following two reasons. First, the energy of the vehicle-track interaction depends on the train speed, particularly in the high-frequency range [38]. In the measurements, a low measuring speed (i.e., 26-28 km/h) makes the high-frequency response less pronounced than the components of the low-frequency response. Second, the high-frequency components, which are generally localized within short duration, are averaged over a long rolling distance from -28 to 28 ms, thus reducing the magnitude of the GWPS.

In Figure 5.9, the measured ABA signals are coherent with each other in terms of the amplitudes of the major peaks and the major frequency components. Because of the non-identical moving trajectory of the wheelset, it is challenging to achieve a precise match between measurements. Nevertheless, the ABA measurement demonstrates satisfactory repeatability in both the spatial and frequency domains, which is essential for detecting crossing degradation.

5

5.3.2 COMPARISON OF ABA BETWEEN NOMINAL AND DEGRADED CROSSINGS

Figure 5.10(a) compares the WPS of the nominal and the degraded states. In the figure, the frequency range is limited to 150-1500 Hz because of the following factors. First, the low-frequency components below 150 Hz mainly correspond to the properties of the track substructure components (such as the subgrade, ballast and sleeper) rather than the crossing rails [39]. Second, the high-frequency components above 1500 Hz have much lower energy than the lower-frequency components and are hardly visible on the same scale (the colour bar). Figure 5.10(b) shows the SAWP, i.e., \bar{W}_{Nom}^2 of the nominal state and \bar{W}_{Deg}^2 of the degraded state. The SAWP is calculated using the values $\bar{W}_n^2[230,350]$ and $\bar{W}_n^2[460,650]$ divided by the constant $\bar{W}_{Nom}^2[230,350]$ at the wheel-crossing impact position.

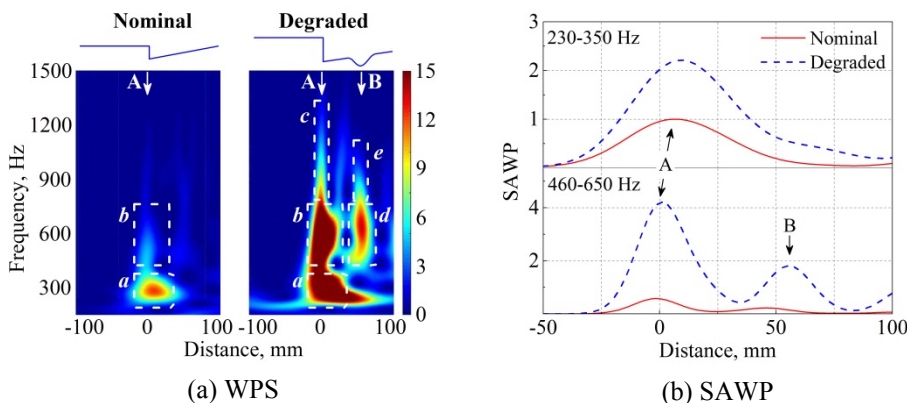


Figure 5.10: Comparison of the ABA at nominal and degraded states. The rectangles indicate the major characteristics. Arrows A and B indicate the location of degradation types 1 and 2.

In the nominal state, most of the vibration energy is localized around arrow A, which is induced by the intrinsic geometric discontinuity of the crossing and thus the wheel-rail impact on the crossing nose. At the arrow, two major characteristic frequencies appear at 230-350 and 460-650 Hz; see rectangles *a* and *b* in Figure 5.10(a).

In the degraded state, the vibration energy distributes at two regions, as denoted by arrows A and B. At arrow A, the major frequencies occur at 230-350 and 460-650 Hz. Because these characteristic frequencies take place in both nominal and degraded states, they should depend on the natural responses of the system rather than the wheel-rail contact geometry. The high-frequency components at arrow A (denoted as rectangle *c*) localize within a short duration such that both the train bogie and the track superstructure components are only minimally affected [40, 41]. Therefore, the high-frequency response is expected to be relevant to the local vibration of contact bodies. The uneven deformation at arrow A (degradation type 1) increases the energy at the two characteristic frequencies. For example, the values of $\bar{W}_{Deg}^2[230,350]$ and $\bar{W}_{Deg}^2[460,650]$ increase by 121% and 631%, compared to the values in the nominal state.

At arrow B, the value of $\bar{W}_{Deg}^2[460,650]$ reaches 1.8. The high vibration energy is related to local irregularity of the crossing nose (degradation type 2). The 460-650 Hz components occur at both degradation types 1 and 2 (arrows A and B), indicating that they are more related to the natural response of the system rather than to the wheel-rail contact geometry. The very-high-frequency components at rectangle *e* in Figure 5.10(a), analogous to those in rectangle *c*, should originate from the local vibration of contact bodies.

By comparing the gathered data in the nominal and degraded states, the following relation between the characteristics of ABA (Figure 5.10) and the measured degradation (Figures 5.7 and 5.8) can be extracted:

- Degradation type 1 (uneven deformation between the wing rail and the crossing nose). It exacerbates the wheel-rail impact and enlarges the energy at the characteristic frequencies of 230-350 and 460-650 Hz. The severity of the degradation can be evaluated by the values of $\bar{W}^2[230,350]$ and $\bar{W}^2[460,650]$ at the wheel-rail impact.
- Degradation type 2 (local irregularity in the longitudinal slope of the crossing nose). It increases the vibration energy at 460-650 Hz. Thus, the location of the irregularity can be determined by the spatial distribution of the 460-650 Hz components, while the severity can be evaluated by the value of $\bar{W}^2[460,650]$.

Figure 5.10(a) (rectangles *c* and *e*) shows that the high-frequency components at 650-1200 Hz become more pronounced in both degradation types. Because these components distribute with relatively short duration, they can be used to better locate the crossing degradation.

5.3.3 DETECTION ALGORITHM FOR MEASURED CROSSING DEGRADATION

By proper correlation of the gathered data from multiple sensors, an algorithm for the detection of crossing degradation is proposed. In the algorithm, the SAWP is calculated using the values $\bar{W}_n^2[230,350]$ and $\bar{W}_n^2[460,650]$ divided by the value $\bar{W}_{Nom}^2[230,350]$ at the wheel-rail impact position. The detection procedure is as follows:

Step 1: Detection of uneven deformation between the wing rail and the crossing nose (i.e., the first degradation type).

- If $\bar{W}^2[230,350] \geq 1$ and $\bar{W}^2[460,650] \geq 0.6$, then the crossing suffers from uneven deformation. Its severity increases with the increase of $\bar{W}^2[230,350]$ and $\bar{W}^2[460,650]$.
- Otherwise, the crossing does not exhibit significant uneven deformation.

Step 2: Detection of local irregularity of the crossing nose (i.e., the second degradation type).

- If there is more than one position with $\bar{W}^2[460,650] \geq 0.3$, then the crossing suffers from irregularity at the nose. Its severity increases with the increase in $\bar{W}^2[460,650]$.
- Otherwise, the crossing does not exhibit significant local irregularity at the nose.

5.4 CASE STUDY: TRIAL DETECTION AND VERIFICATION

In this section, the ABA measurement is performed on a crossing with unknown degradation status as a trial detection, and the capability of the method is verified using profile measurement and field observation.

5

5.4.1 TRACK SITE

Because the concerned crossing had degraded significantly, repair maintenance in terms of grinding and welding was performed to extend its service life and avoid sudden failure. The repair procedure was as follows: first, the crossing rails were ground to remove surface damage (e.g., cracks, uneven wear and plastic deformation); second, the hollow regions caused by grinding were filled by welding; finally, the crossing rails were ground again to the desired profiles. Figure 5.11 shows the repaired crossing profile. Because of the current incapability of operating a train-borne grinding machine at a crossing, the repair was performed manually. The repaired profile depends on the experience of the technicians and may differ significantly from the nominal profile; this is the unknown degradation status for the trial detection.



Figure 5.11: Repaired crossing profile with a magnified image of grinding marks

5.4.2 TRIAL EVALUATION

Figure 5.12(a) compares the WPS of the measured ABA, and Figure 5.12(b) compares the SAWP, i.e., \bar{W}_{Nom}^2 of the nominal state, \bar{W}_{Deg}^2 of the degraded state and \bar{W}_{Rep}^2 of the repaired state. In the nominal state, there is only one position with the value of $\bar{W}^2[460,650]$ exceeding 0.3; there are two positions in both the degraded and repaired states: the first peak is related to the intrinsic geometric discontinuity, while the second is related to the local irregularity of the crossing nose (i.e., degradation type 2). This information indicates that the repair did not completely remove the local irregularity of the crossing nose. The value of $\bar{W}_{Rep}^2[460,650]$ is 15% smaller than the value of $\bar{W}_{Deg}^2[460,650]$, indicating that the severity of the local irregularity was reduced.

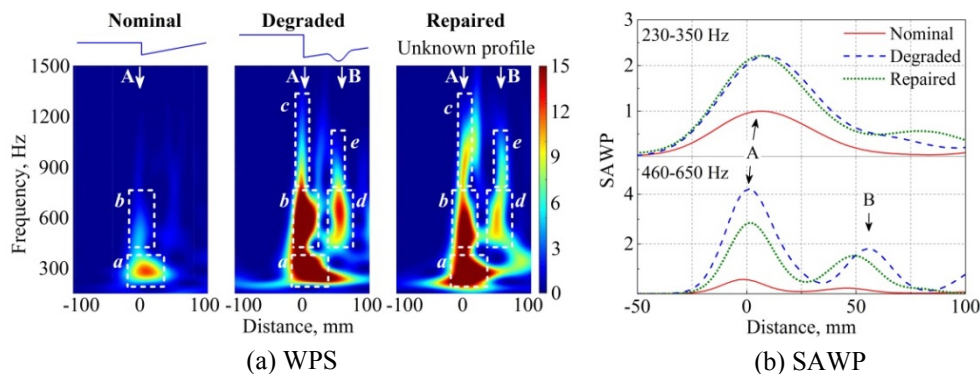


Figure 5.12: Comparison of ABA of nominal, degraded and repaired states. The rectangles indicate the major characteristics. Arrows A and B indicate the location of degradation types 1 and 2.

At arrow A, the value of $\bar{W}_{Rep}^2[460,650]$ decreased by 31% after repair, whereas the value of $\bar{W}_{Rep}^2[230,350]$ remained at a similar level as that in the degraded state. Because the energy concentration at arrow A corresponds to the severity of the uneven deformation between the wing rail and the crossing nose (i.e., degradation type 1), it is determined that the repair failed to compensate for the uneven deformation between the wing rail and the crossing nose. In summary, Figure 5.12 indicates that the repair reduced the severity of the local irregularity of the crossing nose (degradation type 2) but failed to compensate for the uneven deformation between the wing rail and the crossing nose (degradation type 1).

5.4.3 VERIFICATION

To examine the evaluation results, a 3D profile measurement was performed on the repaired crossing. Figure 5.13 compares the measured profile along W1 and N1. The height of the repaired wing rail was nearly restored to the nominal state, whereas the height of the repaired crossing nose became even lower than that in the degraded state. Consequently, the uneven deformation between the wing rail and the crossing nose was exacerbated by the repair. The local irregularity D_{N2} of the crossing nose (degradation type 2) still existed after the repair but was not as severe as the degraded state. Therefore, the evaluation results made by the ABA measurement are considered reliable.

In this chapter, a detection algorithm is developed and verified relying on in situ ABA and 3D profile measurements taken at a single track site. At the site, two crossings with three different health conditions were measured: the first measurement occurred on a degraded crossing, the second measurement was performed shortly after repair, and the third measurement was performed on a new crossing at the same site after the repaired crossing was replaced because of severe cracking.

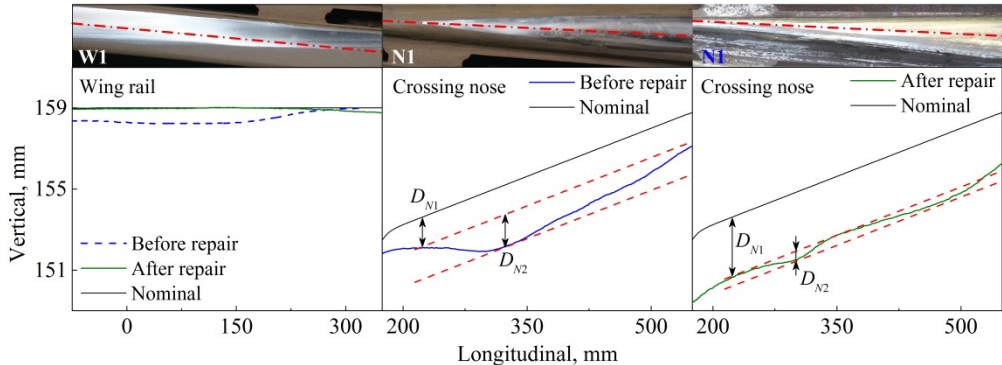


Figure 5.13: Change of the crossing profile due to repair. D_{N1} and D_{N2} indicate the height difference of the crossing nose.

The advantage of focusing on a single site is that the disturbance of non-uniform track conditions on the characteristic vibrations of ABA can be minimized. It would be highly beneficial to demonstrate the detection algorithm on additional crossings. However, access to additional track sites is strictly limited by the safety regulations of the Dutch railway network authority. In this study, we were allowed to perform measurements at only one site, and it required 1.5 years to collect information for three different health conditions. For this feasibility study, the experiment was satisfactorily conducted and provided new information that is helpful for developing a better maintenance strategy. Signal processing together with physical insight into the system provided reliable information for verifying the quality of maintenance actions.

5.5 DISCUSSION: EXTENDING ABA SYSTEM TO OTHER EXAMPLES

To extend the ABA system to other examples, the following aspects should be taken into account:

- The effect of non-identical wheel-rail trajectory on the characteristic frequencies of ABA. In the real-life implementation of the ABA system, it is impossible to keep the identical wheel-rail trajectory among measurements. On one hand, it is difficult to keep in-service trains with a controlled constant train speed; on the other, the wheel-rail trajectory is affected by the randomness of vehicle-track interaction (e.g., hunting oscillation). The effect of non-identical trajectory on the characteristic frequencies of ABA must be analysed. In the literature, it is found that the characteristic frequencies of ABA are related to the natural response of the vehicle-track system [38], so that the characteristic frequencies of ABA and thus the capability of the proposed detection algorithm are not greatly affected by non-identical wheel-rail trajectory.

- The effect of the crossing type on the characteristic frequencies of ABA. In this chapter, the proposed detection algorithm is demonstrated and verified on the crossing type of 54E1-1:9. Because the natural response of crossings may differ from one type to another, the characteristic frequencies of ABA on other crossing types should be extracted. To overcome the limitations on field track testing, computer-aided approaches (e.g., finite element simulation [24] and machine learning [42]) can be used for virtual testing. The ABA system can be more conveniently extended to various crossing types using more flexible and relatively faster numerical modelling rather than time-consuming and expensive in situ measurements.

Moreover, by the correct correlation of the gathered data from different sensors, the proposed detection method can be extended to other track components (e.g., switch and catenary). For example, it is possible to estimate the location and severity of the catenary degradation by collecting and correlating the data of the pantograph-catenary contact force [43] and the catenary irregularities [44] instead of ABA and crossing profiles. In addition to monitoring railway infrastructure, the proposed method can be extended to a broader range of applications, such as inspecting the defects of bearings [45].

5.6 SUMMARY

In this chapter, the capability of the ABA system to detect crossing degradation was investigated. For this purpose, in situ ABA and 3D profile measurements were conducted on both nominal and degraded crossings to extract characteristic vibrations related to the degradation. ABA measurements were then performed on a crossing with unknown degradation status condition as a trial detection, and the capability of the method was verified using 3D profile measurements and field observations. The following conclusions are drawn:

- The ABA system can identify two types of crossing degradation. The first type is uneven deformation between the wing rail and the crossing nose, and the second type is local irregularity in the longitudinal slope of the crossing nose.
- Deformation of the crossing nose that is more severe than that of the wing rail exacerbates wheel-rail impact during the facing motion of vehicles, increasing the energy concentrated at the characteristic frequencies of 230-350 and 460-650 Hz. The severity of the uneven deformation can be evaluated by the energy concentration at these frequencies.
- The presence of a local irregularity at the crossing nose increases the vibration energy at the characteristic frequencies of 460-650 Hz. The location of the irregularity can be determined by the spatial distribution of these frequencies, while the severity can be evaluated by the energy concentration at these frequencies.
- The ABA system can detect crossing degradation at measuring speeds as low as 26-28 km/h. Therefore, the capability of the method in large-scale networks is not restricted to the low operational speed often specified at crossings (40-80 km/h on the Dutch railway).

REFERENCES

5

- [1] B.A. Pålsson, J.C. Nielsen, *Wheel-rail interaction and damage in switches and crossings*, Vehicle System Dynamics **50**, 43-58 (2012).
- [2] ProRail, *Jaarverslag* (Utrecht, Netherland, 2015), pp. 127.
- [3] K. Giannakos, *Modeling the influence of short wavelength defects in a railway track on the dynamic behavior of the Non-Suspended Masses*, Mechanical Systems and Signal Processing **68**, 68-83 (2016).
- [4] R.S. Edwards, S. Dixon, X. Jian, *Characterisation of defects in the railhead using ultrasonic surface waves*, NDT & E International **39**, 468-475 (2006).
- [5] S.C. Her, S.T. Lin, *Non-destructive evaluation of depth of surface cracks using ultrasonic frequency analysis*, Sensors **14**, 17146-17158 (2014).
- [6] M. Papaelias, M. Lugg, *Detection and evaluation of rail surface defects using alternating current field measurement techniques*, Proceedings of the Institution of Mechanical Engineers, Part F: Journal of Rail and Rapid Transit **227**, 310-321 (2012).
- [7] L. Oukhellou, E. Come, L. Bouillaut, P. Aknin, *Combined use of sensor data and structural knowledge processed by Bayesian network: Application to a railway diagnosis aid scheme*, Transportation Research Part C: Emerging Technologies, **16**, 755-767 (2008).
- [8] K. Miya, *Recent advancement of electromagnetic nondestructive inspection technology in Japan*, IEEE Transactions on magnetics **38**, 321-326 (2002).
- [9] Q. Li, S. Ren, *A real-time visual inspection system for discrete surface defects of rail heads*, IEEE Transactions on Instrumentation and Measurement **61**, 2189-2199 (2012).
- [10] T. Xu, G. Wang, H. Wang, T. Yuan, Z. Zhong, *Gap Measurement of Point Machine Using Adaptive Wavelet Threshold and Mathematical Morphology*, Sensors **16**, 2006 (2016).
- [11] J. Wei, C. Liu, T. Ren, H. Liu, W. Zhou, *Online condition monitoring of a rail fastening system on high-speed railways based on wavelet packet analysis*, Sensors **17**, 318 (2017).
- [12] M. Macucci, S. Di Pascoli, P. Marconcini, B. Tellini, *Wireless sensor network for derailment detection in freight trains powered from vibrations*, IEEE International Workshop on Measurements & Networking, 1-6 (2015).
- [13] P. Westeon, C. Ling, C. Roberts, C. Goodman, P. Li, R. Goodall, *Monitoring vertical track irregularity from in-service railway vehicles*, Proceedings of the institution of mechanical engineers, Part F: Journal of Rail and Rapid Transit **221**, 75-88 (2007).
- [14] J. Rose, M. Avioli, W. Song, *Application and potential of guided wave rail inspection*, Insight **44**, 353-358 (2002).
- [15] S. Saponara, B. Neri, *Radar sensor signal acquisition and multidimensional FFT processing for surveillance applications in transport systems*, IEEE Transactions on Instrumentation and Measurement **66**, 604-615 (2017).
- [16] S. Saponara, B. Neri, *Design of compact and low-power X-band Radar for mobility surveillance applications*, Computers & Electrical Engineering **56**, 46-63 (2016).
- [17] J. Wilson, G. Tian, I. Mukriz, D. Almond, *PEC thermography for imaging multiple cracks from rolling contact fatigue*, NDT & E International **44**, 505-512 (2011).

[18] M. Clark, D. McCann, M. Forde, *Infrared thermographic investigation of railway track ballast*, NDT & E International **35**, 83-94 (2002).

[19] K. Bruzelius, D. Mba, *An initial investigation on the potential applicability of Acoustic Emission to rail track fault detection*, NDT & E International **37**, 507-516 (2004).

[20] N. Thakkar, J. Steel, R. Reuben, *Rail-wheel interaction monitoring using Acoustic Emission: A laboratory study of normal rolling signals with natural rail defects*, Mechanical Systems and Signal Processing **24**, 256-266 (2010).

[21] M. Clark, M. Gordon, M.C. Forde, *Issues over high-speed non-invasive monitoring of railway trackbed*, NDT & E International **37**, 131-139 (2004).

[22] I.L. Al-Qadi, W. Xie, R. Roberts, Z. Leng, *Data analysis techniques for GPR used for assessing railroad ballast in high radio-frequency environment*, Journal of Transportation Engineering **136**, 392-399 (2010).

[23] M. Molodova, Z. Li, A. Núñez, R. Dollevoet, *Automatic detection of squats in railway infrastructure*, IEEE Transactions on Intelligent Transportation Systems **15**, 1980-1990 (2014).

[24] M. Molodova, Z. Li, R. Dollevoet, *Axle box acceleration: Measurement and simulation for detection of short track defects*, Wear **271**, 349-356 (2011).

[25] M. Molodova, M. Oregui, A. Núñez, Z. Li, R. Dollevoet, *Health condition monitoring of insulated joints based on axle box acceleration measurements*, Engineering Structures **123**, 225-235 (2016).

[26] A. Massel, *Power spectrum analysis—modern tool in the study of rail surface corrugations*, NDT & E International **32**, 429-436 (1999).

[27] M. Boccilone, A. Caprioli, A. Cigada, A. Collina, *A measurement system for quick rail inspection and effective track maintenance strategy*, Mechanical Systems and Signal Processing **21**, 1242-1254 (2007).

[28] H. Tanaka, A. Shimizu, *Practical Application of Portable Trolley for the Continuous Measurement of Rail Surface Roughness for Rail Corrugation Maintenance*, Quarterly Report of RTRI **57**, 118-124 (2016).

[29] S. Alfi, F. Braghin, S. Bruni, *Numerical and experimental evaluation of extreme wheel-rail loads for improved wheelset design*, Vehicle System Dynamics **46**, 431-444 (2008).

[30] S. Kaewunruen, *Monitoring structural deterioration of railway turnout systems via dynamic wheel/rail interaction*, Case Studies in Nondestructive Testing and Evaluation **1**, 19-24 (2014).

[31] C.P. Ward, P. Weston, E. Stewart, H. Li, R.M. Goodall, C. Roberts, T. Mei, G. Charles, R. Dixon, *Condition monitoring opportunities using vehicle-based sensors*, Proceedings of the Institution of Mechanical Engineers, Part F: Journal of Rail and Rapid Transit **225**, 202-218 (2011).

[32] P. Salvador, V. Naranjo, R. Insa, P. Teixeira, *Axlebox accelerations: Their acquisition and time-frequency characterisation for railway track monitoring purposes*, Measurement **82**, 301-312 (2016).

[33] A. Ovanesova, L. Suarez, *Applications of wavelet transforms to damage detection in frame structures*, Engineering structures **26**, 39-49 (2004).

5

- [34] M. Vetterli, J. Kovacevic, *Wavelets and subband coding*, Prentice-Hall (1995).
- [35] A. Grinsted, J.C. Moore, S. Jevrejeva, *Application of the cross wavelet transform and wavelet coherence to geophysical time series*, *Nonlinear processes in geophysics* **11**, 561-566 (2004).
- [36] C. Torrence, G.P. Compo, *A practical guide to wavelet analysis*, *Bulletin of the American Meteorological society* **79**, 61-78 (1998).
- [37] Z. Wei, C. Shen, Z. Li, R. Dollevoet, *Wheel-rail impact at crossings: relating dynamic frictional contact to degradation*, *Journal of Computational and Nonlinear Dynamics* **12**, 041016 (2017).
- [38] M. Molodova, Z. Li, A. Nunez, R. Dollevoet, *Parameter study of the axle box acceleration at squats*, *Proceedings of the Institution of Mechanical Engineers, Part F: Journal of Rail and Rapid Transit* **229**, 841-851 (2014).
- [39] A.P. De Man, *DYNATRACK: A survey of dynamic railway track properties and their quality*, PhD dissertation, Delft University of Technology (2002).
- [40] J.C. Nielsen, A. Igeland, *Vertical dynamic interaction between train and track influence of wheel and track imperfections*, *Journal of Sound and Vibration* **187**, 825-839 (1995).
- [41] T. Wu, D. Thompson, *On the impact noise generation due to a wheel passing over rail joints*, *Journal of Sound and Vibration* **267**, 485-496 (2003).
- [42] G. Krummenacher, C.S. Ong, S. Koller, S. Kobayashi, J.M. Buhmann, *Wheel defect detection with machine learning*, *IEEE Transactions on Intelligent Transportation Systems* **99**, 1-12 (2017).
- [43] M. Carnevale, A. Collina, *Processing of collector acceleration data for condition-based monitoring of overhead lines*, *Proceedings of the Institution of Mechanical Engineers, Part F: Journal of Rail and Rapid Transit*, **230**, 472-485 (2016).
- [44] Z. Liu, H. Wang, R. Dollevoet, Y. Song, A. Núñez, J. Zhang, *Ensemble EMD-based automatic extraction of the catenary structure wavelength from the pantograph-catenary contact force*, *IEEE Transactions on Instrumentation and Measurement* **65**, 2272-2283 (2016).
- [45] G. Marichal, M. Artes, J. Garcia-Prada, *An intelligent system for faulty-bearing detection based on vibration spectra*, *Journal of Vibration and Control* **17**, 931-942 (2011).

6

CONCLUSIONS AND RECOMMENDATIONS

6.1 CONCLUSIONS

Chapters 2-5 analyse the dynamic wheel-rail interaction at railway crossings from different perspectives. In this chapter, these works are retrospected and the research questions in Chapter 1 are addressed.

Q1 *How does the wheel-rail contact behaviour evolve during the passage of vehicles over crossings? How does the contact behaviour relate to the degradation of crossing rails?*

Chapter 2 aims to address the research question Q1. In this chapter, an explicit FE model capable of presenting the dynamic wheel-rail interaction at crossings is developed. The simulated dynamic response, in terms of the major frequencies and energy distributions of ABA, is verified via in-situ ABA measurements. The wheel-rail contact parameters (i.e., contact force, contact position, contact patch, adhesion-slip state, pressure, shear traction and micro-slip) are elaborated during the passage of a wheelset. Thereafter, these parameters are used to predict the rail degradation due to plastic deformation and wear. From the above analysis, the following conclusions are drawn:

Characteristics of wheel-rail contact behaviour

- During the passage of a wheelset on the nominal crossing, the variations of the normal contact force and the tangential contact force are out-of-sync on both the wing rail and the crossing nose, owing to the complex wheel-rail contact geometry and the presence of two-point contact.
- The centreline of the wing rail is misaligned with the rolling direction of the wheelset. Meanwhile, the widening of the crossing nose also causes misalignment between the wheel-rail contact trajectory and the rolling direction of the wheelset. As a consequence, the value of lateral creepage raises during the impact.
- At the two-point contact stage, the decrease of the lateral contact force on the wing rail is slower than the longitudinal contact force, so that the vectors of shear traction and micro-slip on the wing rail almost point towards the lateral direction.

Degradation of crossing rails

- With nominal crossing geometry and facing motion of vehicles, the maxima of both plastic deformation and wear on the crossing nose occur during the two-point contact transition from the wing rail to the crossing nose rather than, as widely believed, at the moment of maximum normal contact force.
- On the crossing nose, the trajectories of the maximum plastic deformation and wear do not coincide with the centreline of the running band, and the lateral distance between them varies along the rolling direction.

Q2 *Whether and how does the wheel-rail contact behaviour differ between nominal and long-term serviced crossings? How to evaluate the performance of long-term serviced crossings under traffic loads?*

Chapter 3 aims to address the research question Q2. In this chapter, a method is proposed to evaluate the performance of long-term serviced crossings. In the method, the 3D profile and hardness of a long-term serviced crossing are measured and serve as the input for the FE

modelling of dynamic wheel-rail interaction. Thereafter, the simulated contact parameters (i.e., contact force, contact position, contact patch, adhesion-slip state, pressure, shear traction and micro-slip) are used to calculate the distributions of plastic deformation and wear. Finally, the performance of the long-term serviced crossing can be extracted by comparing the results between nominal and long-term serviced conditions. To demonstrate the method, a case study was conducted on a crossing which had serviced in the Dutch railway for a long-term, and the following conclusions are drawn from the case study:

Contact behaviour in the major traffic direction

- The long-term serviced crossing experienced a run-in process, manifested as the increase of the curvature radius of the crossing profile, the widening of the running band and the enlargement of the contact patch size.
- Despite the growth of the contact force on the long-term serviced crossing, the magnitudes of both pressure and surface shear traction decrease due to the run-in.
- The lateral displacement of the running band from wheel flange root towards wheel tread increases significantly on the long-term serviced crossing.
- On the long-term serviced crossing, the magnitudes of both plastic deformation and wear decrease compared to those on the nominal crossing, as a benefit of the run-in.

Contact behaviour in the minor traffic direction

- The curvature radius of the crossing profile reduces on the long-term serviced crossing, and the width of the running band shrinks especially around the region with the maximum contact force.
- The maxima of both pressure and surface shear traction increase on the long-term serviced crossing, which is induced by the combination of enlarged contact force and reduced contact patch size.
- The dynamic wheel-rail interaction exacerbates on the long-term serviced crossing, so that the magnitudes of both plastic deformation and wear increase compared with those on the nominal crossing.

Q3 *What is the characteristic dynamic response during vehicle-track interaction at crossings? Whether and how does the ABA relate to the nature of the track structure?*

Chapters 4 aims to address the research question Q3. In the chapter, the characteristics of ABA under various test parameters is studied by combining in-situ ABA measurements and roving-accelerometer hammer tests. These parameters include the train moving direction (facing and trailing directions with respect to the crossing), train speed, sensor position (leading and rear wheels of a bogie) and crossing natural response. From the above analysis, the following characteristics of ABA can be extracted:

- The correlation of ABA measurements with hammer tests indicates that the major frequency bands of the vertical ABA at 240-305 and 505-620 Hz are related to the natural frequencies of the crossing at 265, 490, 548 and 621 Hz. Therefore, the major frequency bands of the vertical ABA are not greatly affected by variations in train speed, moving direction or sensor position.

- The increase of the train speed enlarges the amplitude of the vertical ABA and the energy concentrated at the major characteristic frequency bands.
- The energy at the major frequency bands of the vertical ABA depends on the train moving direction. In particular, the facing motion of the train significantly enlarges the vibration energy at the first major frequency band of 240-305 Hz.
- The vertical ABA acquired from the leading wheel corresponds to larger amplitude and larger vibration energy compared with that from the rear wheel.
- The vibrations of crossing rails at the major frequency bands of the vertical ABA are not pure bending, because the vibrations of two wing rails are not synchronized. Instead, the vibrations of crossing rails are a combination of bending and torsion.
- The major frequency bands of the longitudinal ABA, i.e., 205-215 Hz and 500-540 Hz in the facing direction and at 200-210 Hz and 540-560 Hz in the trailing direction, are not strongly affected by the train moving direction.
- Variations in the train speed significantly affect the vibration energy at the major frequency bands of the longitudinal ABA rather than the major frequency bands themselves, similar to the vertical ABA.

Q4 *Whether the ABA system can be used for the condition monitoring of crossings? If feasible, which kind of defects can be identified?*

6

Chapter 5 aims to address the research question Q4. In this chapter, a method is proposed to monitoring the health condition of crossings. In the method, ABA signals and 3D crossing profiles are measured on a crossing over time, in order to develop the relationships between the characteristics of ABA and the measured degradation. To demonstrate the capability of the method, ABA measurements are performed on a crossing with unknown degradation status as a trial detection, and the prediction results are verified using 3D profile measurements. The following conclusions are drawn from Chapter 5:

- The ABA system demonstrates the capability in identifying two types of crossing degradation. The first type is the uneven deformation between wing rail and crossing nose, and the second type is the irregularity in the longitudinal slope of crossing nose.
- Severe deformation of crossing nose than wing rail exacerbates the wheel-rail interaction during the facing motion of vehicles, enlarging the energy at the frequency bands of ABA at 230-350 and 460-650 Hz. The severity of uneven deformation can be evaluated through the energy concentration at these characteristic frequency bands.
- The presence of local irregularity of crossing nose enlarges the vibration energy at the frequency bands of ABA at 460-650 Hz. The location of the irregularity can be determined by the spatial distribution of these characteristic frequency bands, while the severity can be evaluated by the energy concentration at these frequency bands.
- The ABA system can detect the preceding two types of degradation at measuring speeds as low as 26-28 km/h. Therefore, the capability of the method in large scale networks is not restricted to the low operational speed often specified at crossings (40-80 km/h on the Dutch railway).

6.2 RECOMMENDATIONS

The analysis in this dissertation provides a better understanding of the dynamic wheel-rail interaction at railway crossing, including characterizing the wheel-rail contact behaviour, evaluating the performance of crossings under traffic loads and monitoring the health condition of the structure. In future work, there are several possibilities to extend the presented work for more general and practical applications.

- **Measures to slow down the degradation of crossing rails**

The analysis in Chapter 2 illustrates that the maxima of both plastic deformation and wear appeared during two-point contact rather than at the region with the maximum normal contact force. Since the degradation of the crossing is attributed to the combined effect of the normal, longitudinal, and lateral contact forces, their non-proportionality should be taken into account [1]. This highlights the necessity for detailed analysis of stress and strain in future work, to develop an insightful understanding of the initiation and growth of crossing degradation.

In Chapter 3, a run-in process occurred on the long-term serviced crossing; it widened the running band, enlarged the contact patch size and eventually reduced the contact stresses in the material. These benefits of the run-in can be achieved by profile optimization for new crossings or maintenance grinding for existing crossings. The analysis indicates that the curvature radius of the crossing profile and the wheel-rail contact position are the two essential factors determining the shape and size of the contact patch. Therefore, the crossing profile can be optimized by adjusting these parameters.

In general, the service life of crossing rails is limited by accumulated plastic deformation, wear and RCF. High contact stresses in the material can induce RCF such as cracks and shelling, which will significantly speed up the failure of crossing rails. Proper wear is beneficial to suppress the propagation of surface-initiated cracks. The experimental and numerical approaches proposed in Chapters 2 and 3 demonstrate the capability of the proposed FE model in capturing the regions with high contact stresses and low wear rate. This information can be used to minimize the RCF defects by combining with other measures, such as the use of friction modifier [2] in certain regions.

- **Predicting the remaining life of crossing rails and optimizing maintenance strategy**

It happens frequently that the maintenance actions (e.g., grinding and welding) are prior performed on crossing rails with severe RCF defects (e.g., cracks, shelling and head checks). For crossings without severe RCF defects, often no maintenance actions are taken even though their profiles degrade significantly due to wear and plastic deformation.

In Chapters 2 and 3, the proposed numerical and experimental methods demonstrate the capability of presenting detailed information of wheel-rail interaction behaviour on both nominal and long-term serviced crossings. This information can be used to predict the rail degradation [3-5] and further to estimate the remaining life of crossings. As a benefit, proper maintenance strategy can be developed to reduce the maintenance cost while avoiding sudden failure of the structure.

- **Extending the ABA system to more real-life examples**

In Chapter 5, a detection algorithm of crossing degradation is developed and verified by conducting in situ ABA and 3D profile measurements. Two crossings with three different health conditions were measured: the first measurement took place on a degraded crossing; the second was performed on the same crossing shortly after it was renewed; the third measurement was performed on a new crossing at the same site, since the renewed crossing was replaced 5 months later due to severe cracks.

The advantage of focusing on one crossing site is that the influence of different track conditions on the signature tune of ABA can be minimized. On the other hand, it is indicated in Chapter 4 that the characteristic response of ABA is related to the natural response of crossings. Therefore, the influence of different crossing types (e.g., different crossing angles from 1:9 to 1:29) and track components (e.g., wooden sleeper and concrete sleeper) on the characteristic frequencies of ABA should be analysed in the future.

To optimize the performance of the ABA system for a variety of crossing types, the detection algorithm needs to be adjusted to account for the natural behaviour of the different crossings. The adjustment can be achieved by in situ ABA measurements, which is time-consuming and expensive. Alternatively, the signature tunes of crossings can also be extracted by numerical simulations [6], so that the capability of ABA system can be more easily extended to large-scale networks.

6

REFERENCES

- [1] Y. Liu, L. Liu, S. Mahadevan, *Analysis of subsurface crack propagation under rolling contact loading in railroad wheels using FEM*, Engineering Fracture Mechanics **74**, 2659-2674 (2007).
- [2] D.T. Eadie, D. Elvidge, K. Oldknow, R. Stock, P. Pointner, J. Kalousek, P. Klauser, *The effects of top of rail friction modifier on wear and rolling contact fatigue: Full-scale rail-wheel test rig evaluation, analysis and modelling*, Wear **265**, 1222-1230 (2008).
- [3] B. Dirks, R. Enblom, *Prediction model for wheel profile wear and rolling contact fatigue*, Wear **271**, 210-217 (2011).
- [4] S. Bogdański, P. Lewicki, *3D model of liquid entrapment mechanism for rolling contact fatigue cracks in rails*, Wear **265**, 1356-1362 (2008).
- [5] D. Fletcher, L. Smith, A. Kapoor, *Rail rolling contact fatigue dependence on friction, predicted using fracture mechanics with a three-dimensional boundary element model*, Engineering Fracture Mechanics **76**, 2612-2625 (2009).
- [6] M. Molodova, Z. Li, A. Núñez, R. Dollevoet, *Parameter study of the axle box acceleration at squats*, Proceedings of the Institution of Mechanical Engineers, Part F: Journal of Rail and Rapid Transit **229**, 841-851 (2014).

A

FRictional CONTACT OF COMPRESSION-SHIFT-ROLLING EVOLUTION

This chapter presents a three dimensional finite element approach capable of realistically simulating a wide range of contact types with partial slip. The approach is demonstrated by analysing the evolution of instationary contact from compression to shift till stationary rolling. It is systematically validated using classical solutions, i.e., Hertz theory for the frictionless normal problem, and Spence solution for frictional compression, Cattaneo solution for tangential shift and Kalker's CONTACT for frictional rolling. The effect of plastic deformation on the distributions of pressure, adhesion-slip regions, surface shear traction and micro-slip is investigated. It is shown that plastic deformation makes the normal contact solution dependent on the tangential contact solution. Plastic deformation partly damps out the structure vibrations and significantly diminishes the magnitude of micro-slip. The presented model can readily be extended to the start-off and braking of railway vehicles, to analyse the evolution of frictional contact and related damages.

This chapter is based on:

Wei Z, Li Z, Qian Z, Chen R, Dollevoet R. 3D FE modelling and validation of frictional contact with partial slip in compression–shift–rolling evolution. International Journal of Rail Transportation 4 (2016): 20-36.

A.1 INTRODUCTION

Partial slip, i.e., slip that only occurs in certain region of a contact patch, commonly exists in the contact process of compression [1, 2], shift [3, 4] and rolling [5-7]. In various engineering applications, partial slip is one of the main causes of surface failures. For instance, partial slip often causes fatigue and cracking, because it results in local saturation of friction and therefore high tangential stress [8]. In circumstances where friction hinders the operation of components, e.g., gears and bearings, surface failures can be avoided or delayed by means of lubrication. On the contrary, where friction contributes to the functioning of a system, such as tires and wheels, wear resulted from partial slip often determines the life of the rolling elements. Thus, understanding the behaviour of partial slip is essential for analysing frictional contact and related failures of solid bodies.

Classical analytical contact models, e.g., Cater [5], Cattaneo [6] and Mindlin [3, 4], are established on the linear elasticity and half-space assumptions, so they are only capable in simple situations. Semi-analytical methods extends the classical solutions to more general contact problems, such as the frictional contact between dissimilar materials [1, 2]. For scenarios where (semi-) analytical methods are not applicable, such as rough profiles and inelastic materials, numerical approach may provide alternative ways.

Many efforts have been made to establish numerical contact models to treat partial slip behaviour in frictional compression [9, 10], shift [11, 12] and rolling [7, 13]. Among them, the determination of adhesion-slip regions in frictional rolling can be quite complex due to the involvement of spin and creepage. A major advancement on rolling contact was proposed by Kalker [7], in which a boundary element method (BEM) is employed to determine the quantitative relationship between contact force and arbitrary creepage and spin. Kalker's theory was later extended from half-space to quasi-quarter-space [14, 15] to deal with conformal contact. The boundary element approach is reliable and accurate with the restriction of linear elasticity and half-space or quasi-quarter-space based contact geometry, yet it is inadequate for plasticity, dynamic interactions and complex geometry.

With the rapid development of computational power, the finite element (FE) method attracts more attention for more practical rolling contact problems. Nackenhorst et al. [13, 16] studied the stationary rolling of a deformable body (tire) on a rigid plane surface (road). In order to avoid the non-differentiability of Coulomb's friction law at the onset of slip motion, a regularization parameter is introduced to render smooth transition between adhesion and slip. Such regularization is applicable for finite deformation problems (e.g., tire-road contact), yet is so far not successful for infinitesimal deformation problems (e.g., wheel-rail contact) because of the difficulty in estimating the regularization parameter [17]. If the parameter is too large, the physical adhesion-slip motion can hardly be predicted. While if it is too small, convergence problems may occur. Recently, a transient FE approach has succeeded in dealing with the infinitesimal deformation problems [18, 19]. The main advantage of this approach is that the non-differentiability of Coulomb's law is avoided in a physical way, so that realistic solutions of adhesion-slip motions can be obtained. However, the capability of the approach to deal with a broader range of contact types is not yet explored. This chapter demonstrates such capability by simulating the frictional contact experiencing compression-shift-rolling evolution, especially when plastic deformation of contact bodies is involved. In practice, improper traction and braking control of railway vehicle may lead to damages such as wheel burns and squats [20]. The method presented is able to obtain precise contact solution during

instationary interactions, e.g., the start-off and braking process, and an further effort can be made for damage analysis under various engineering applications.

The structure of this chapter is as follows. In Section A.2, a finite element method is introduced and the process of compression-shift-rolling with partial slip is simulated. This includes the complete continuous instationary evolution process from compression by resting one solid body on another, to shift by pushing the solid body in the rolling direction so that the body starts to roll, until stationary frictional rolling sets in. Thus a wide range of contact types is involved with partial slip. The effect of plastic deformation on the distributions of pressure, adhesion-slip regions, shear traction and micro-slip is analysed. In Section A.3, the FE solution is validated systematically using classical contact solutions, namely Hertz theory for the frictionless normal problem, and Spence solution for frictional compression, Cattaneo solution for tangential shift and Kalker's computer program CONTACT for frictional rolling. The results are discussed in Section A.4, and the main conclusions are drawn in Section A.5.

A.2 DEMONSTRATION OF THE FE MODEL

The FE model is demonstrated by letting one solid body rolling over another, as depicted in Figure A.1. A three-dimensional moving Cartesian coordinate system is adopted, with the axes x , y , and z oriented in the longitudinal, lateral and vertical directions, respectively. The origin o is located at the centre of, and moved with, the contact patch. The rolling axis of the upper body is perpendicular to the longitudinal axis of the lower body, and the radii of the upper body in the xoz plane and of the lower body in the yoz plane are both 0.2 m. Two types of materials, i.e., a linear elastic material and a bilinear kinematic strain hardening elasto-plastic material, are adopted for the solid bodies. The instationary process of compression-shift-rolling is simulated twice, with only one type of material employed in each simulation. For both materials, the density, Young's modulus and Poisson's ratio are taken as 7800 kg/m^3 , 210 GPa and 0.3 . While for the elasto-plastic material, the yield stress and tangent modulus are 900 MPa and 21 GPa , respectively.

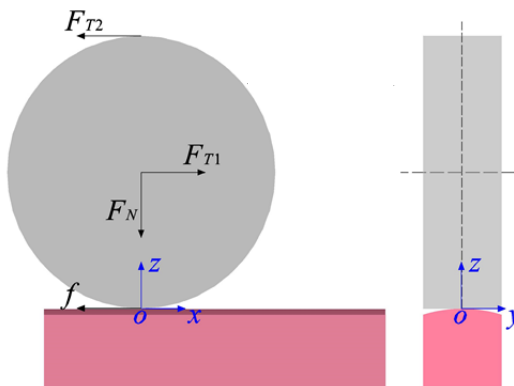


Figure A.1: Schematic diagram of the 3D model

In the FE model, all continua are meshed with 8-node solid elements, and the minimum element size in the contact patch is $0.5 \times 0.5 \text{ mm}$. Coulomb's friction law is employed and the frictional coefficient μ is 0.5.

The calculating procedure is shown in Figure A.2, nodal force and velocity are initially obtained using ANSYS/LS-DYNA, and then a Fortran code is employed to calculate the distributions of adhesion-slip regions and micro-slip. In the flow chart below, ε_N and ε_T are tolerances to identify the adhesion and slip regions.

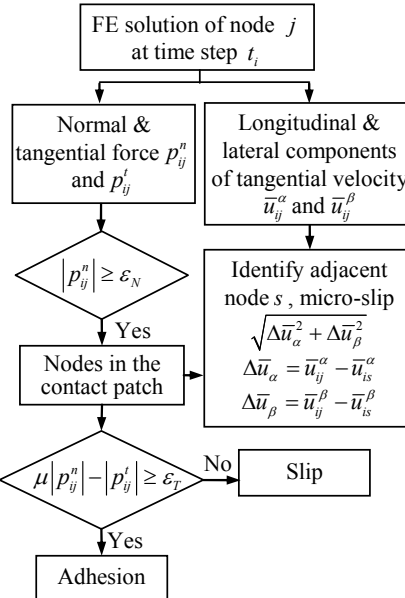


Figure A.2: Flow chart of the calculating procedure

Table A.1: Four stages during compression–shift–rolling evolution

Stage	Duration	$F_{T2} - F_{T1}$	Frictional force f
Compression	0 to t_F	0	0
Shift	t_F to $2t_F$	βF_N	$0 < f \leq \beta F_N$
Transition from shift to rolling	$2t_F$ to $3t_F$	βF_N	$\beta I F_N / (I + MR^2) < f \leq \beta F_N$
Stationary rolling	After $3t_F$	βF_N	Approximate $\beta I F_N / (I + MR^2)$

Figure A.3(a) shows the loading scenario of the FE model. Three loading curves are applied on the nodes of upper solid body: 1) a normal force F_N on the rolling axis, followed by 2) a longitudinal tangential force F_{T1} , with the maximum $2\beta F_N$, on the rolling axis (where β is a constant ratio and satisfies $0 < \beta < \mu$ to achieve partial slip behaviour in the contact patch), and 3) a longitudinal tangential force F_{T2} on the top of the body, with a maximum value of βF_N . Here, all loading paths are in the form of sinusoidal functions, and the durations of loading & unloading, namely t_F , are set to 50 ms. Thus, four stages, which are listed in Table A.1, are achieved sequentially. In the table, M , R and I are the mass, radius and moment of inertia of the upper body, and the values of M , R and I are 84.3 kg, 0.2 m and $1.7 \text{ kg}\cdot\text{m}^2$, respectively. For the sake of minimizing the undesired vibration, the lower body is supported continuously on a rigid foundation. Besides, the lateral displacement of the upper body is constrained such that its movement is restricted to the vertical and longitudinal direction.

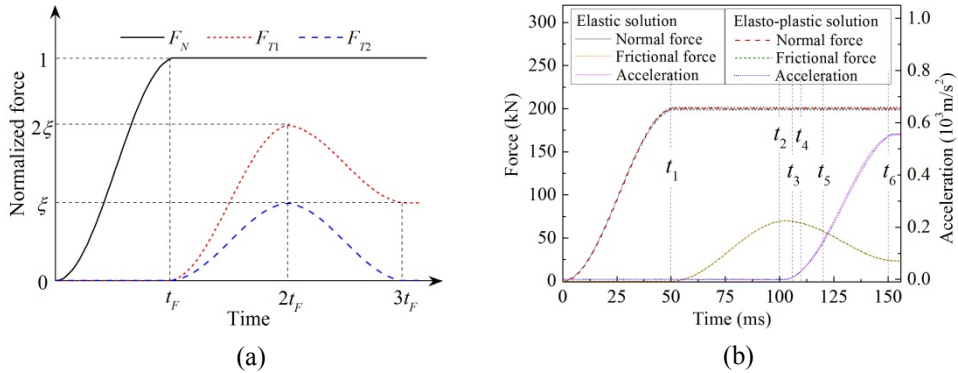


Figure A.3: Loads and response of the FE model. (a) Loading scenario on the upper body, (b) response of the elastic and elasto-plastic solutions.

The values of F_N and β are set to be 200 kN and 0.35, respectively. Here, a relatively large value of β is used to make the slip region in the contact patch clearly observed. To gain an insight into the evolution of the frictional contact, six instants are selected from the four stages, i.e., compression (0 to t_1 , $t_1 = t_F = 50$ ms), shift (t_1 to t_2 , $t_2 = 2t_F = 100$ ms), transition from shift to rolling (t_2 to t_6 , $t_3 = 106$ ms, $t_4 = 110$ ms, $t_5 = 120$ ms and $t_6 = 3t_F = 150$ ms) and stationary rolling (after t_6). The distributions of adhesion-slip regions, pressure, surface shear traction as well as micro-slip are elaborated from the local surface of the lower body. Figure A.3(b) compares the contact force and the translational acceleration of the upper body between the two solutions. As can be seen, once the external normal load F_N is fully applied, the normal contact force Q in both solutions fluctuates around 200 kN with slightly different amplitudes, of which the maximum value is 0.95% in the elastic solution and is 0.34% in the elasto-plastic solution. The fluctuation is from the vibration of the system caused by the loading and is a physical phenomenon. The results show that the plastic deformation of contact bodies absorbs energy and reduces such vibration. The time histories of frictional force f in both solutions are quite similar, the frictional force reaches its maximum value at t_2 , which is 70 kN, followed by a decline between t_2 and t_6 , and subsequently achieves the stationary value of 23 kN at t_6 with constant translational and rotational accelerations from then on.

Figure A.4 shows the distributions of adhesion and slip regions in the contact patch. The overall trends from the two solutions are quite similar. In the compression stage at t_1 , the contact patch is totally occupied by an adhesion region (Figure A.4(a)), following from the identical material and equal radii of the contact bodies. During the shift stage (from t_1 to t_2), the slip region, in the form of an annulus, initiates from the edge of the contact patch, and expands gradually towards the centre of the contact patch (see Figure A.4(b)) with increasing tangential loads. Immediately after t_2 , when the upper body starts to roll, the original circular adhesion region remains almost in the centre of the contact patch. Another adhesion region, in the shape of a crescent, appears at the leading edge of the contact patch, as shown in Figure A.4(c). Then, the leading adhesion region extends towards the centre of the contact patch until the two adhesion regions merge (Figure A.4(d)). At t_5 , the combined adhesion region occupies the majority of the contact patch (Figure A.4(e)). Stationary rolling of the upper body is obtained with the distribution of adhesion and slip regions being constant from t_6 on, as shown in Figure A.4(f).

A

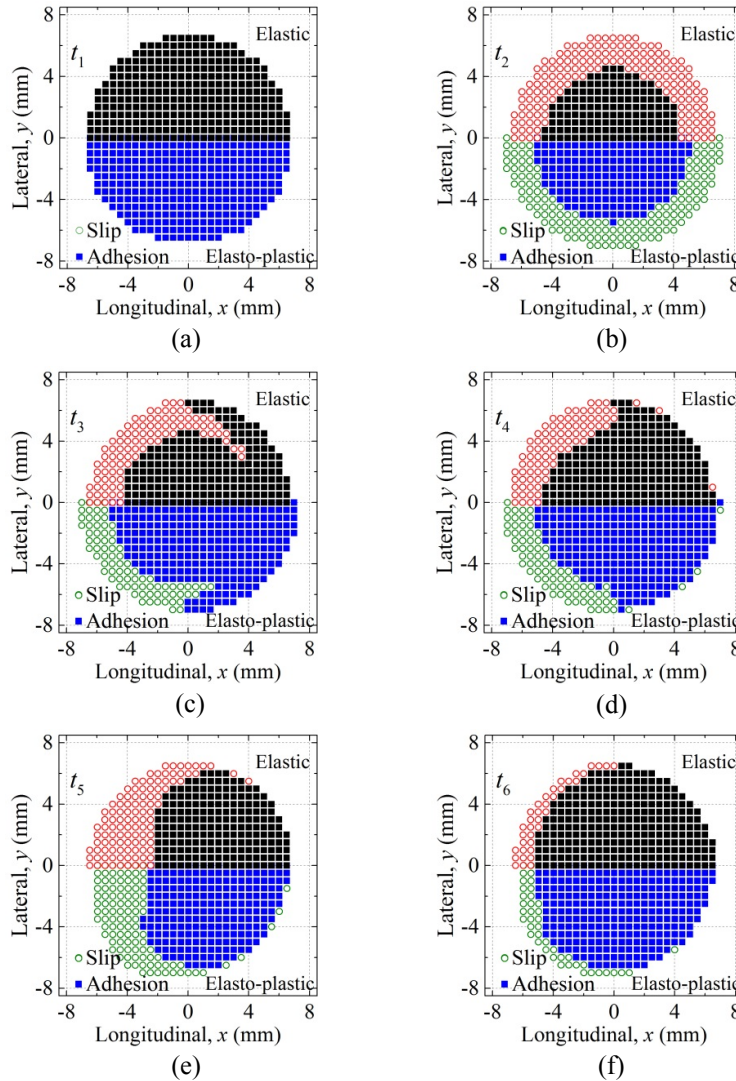


Figure A.4: Adhesion-slip region between the elastic and the elasto-plastic solution. The top half is for elastic solution, the bottom half for elasto-plastic solution.

In the elastic solution, the size of the contact patch is approximate 144 mm^2 throughout the instationary process, while in the elasto-plastic solution it varies from 150 to 165 mm^2 and is always larger than the elastic solution.

Figure A.5 shows the distributions of the surface shear traction along the longitudinal axis ($y=0$). The traction bound, which is the theoretical Hertz pressure multiplied by the friction coefficient, is included for comparison. For both solutions the values of surface shear traction are negligible at t_1 (Figure A.5(a)). When the tangential loads are exerted, the surface shear traction gradually increases from the edge of contact patch, with two peaks emerging at the

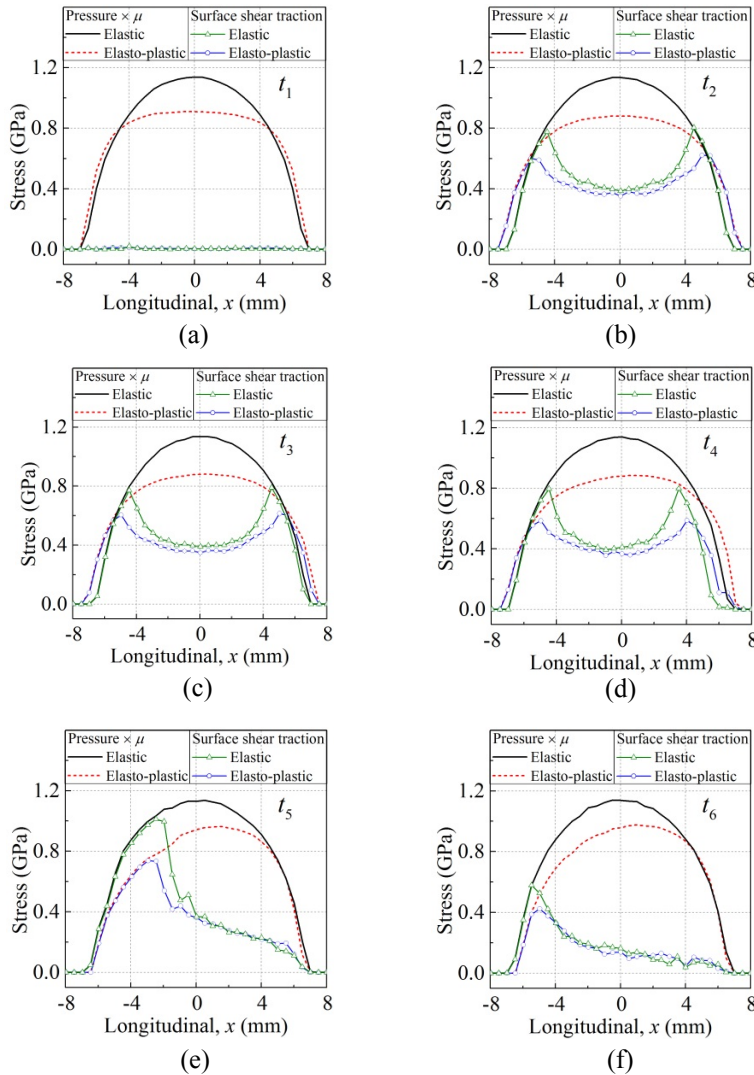


Figure A.5: Stress distributions between the elastic solution and the elasto-plastic solution along the axis ($y=0$).

junction of the adhesion and slip regions (Figure A.5(b)). Once the tangential loads start to decrease (see Figure A.3), the leading peak turns to move towards the centre of the contact patch, with its magnitude remaining at almost the same level, as shown in Figures A.5(c)–(d). Thereafter, the shear traction increases in the rear half of the contact patch whilst decreases in the leading half (compare Figure A.5(d) with A.5(e)). Stationary frictional rolling, as shown in Figure A.5(f), is eventually achieved and the surface shear traction distribution remains at the same level from t_6 on. As can be seen, the peaks of the pressure in the elastic solution are always higher than the corresponding values in the elasto-plastic solution among all the selected instants. The maximum pressure in the elastic solution remains around 2.27 GPa.

While the maximum pressure in the elasto-plastic solution fluctuates between 1.76 to 1.95 GPa. The difference between the two solutions is attributed to the plastic deformation, that is, plastic deformation enlarges the size of the contact patch, and the pressure decreases with an approximately constant normal load.

A

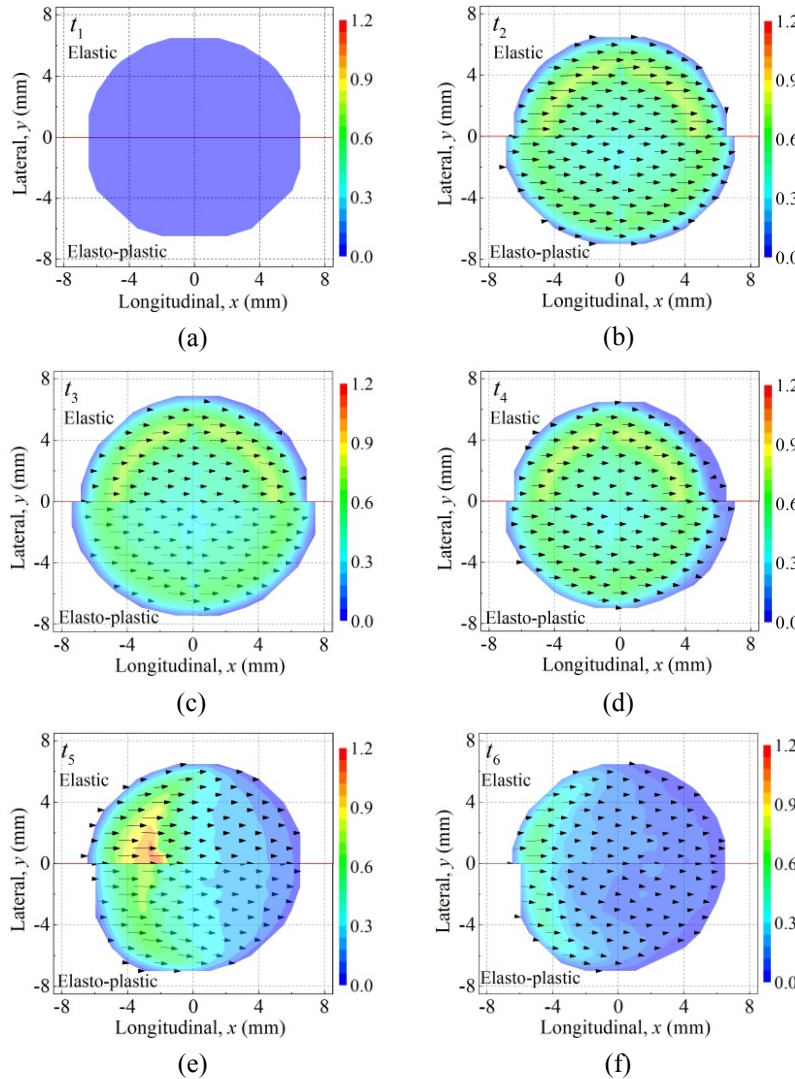


Figure A.6: Surface shear traction fields between the elastic and the elasto-plastic solution. The top half is for elastic solution, the bottom half for elasto-plastic solution.

Figure A.6 shows the fields of surface shear traction. There is no shear traction at t_1 . Except for t_1 , the direction of shear traction is approximately in accordance with the shift and the rolling direction of the upper body. The small lateral components are from the slight geometrical spin owing to the curvature of the contact surfaces, see Figure A.6(f).

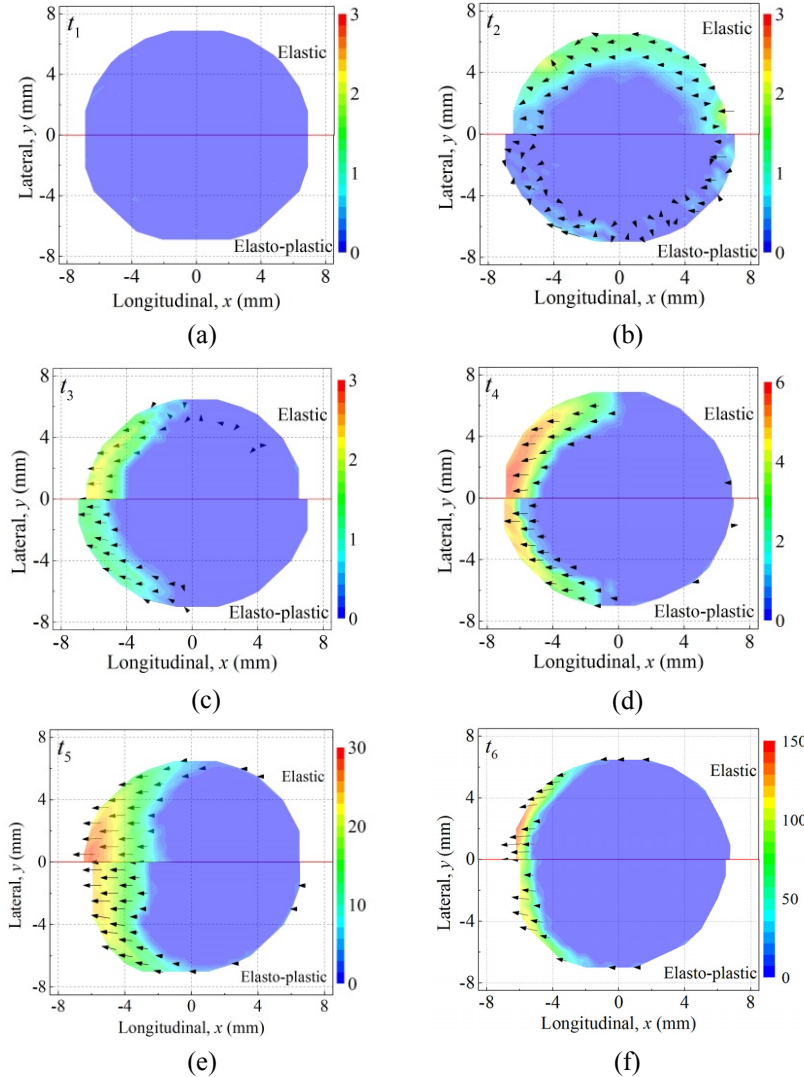


Figure A.7: Micro-slip fields between the elastic and the elasto-plastic solution. The top half is for elastic solution, the bottom half for elasto-plastic solution.

Figure A.7 shows the fields of micro-slip. For illustration purpose the translational velocity ψ of the upper body is included. There are no micro-slip vectors at t_1 due to the same reason for Figure A.6(a). The maximum micro-slip in the shift stage locates at the border of the contact patch (Figure A.7(b)). After t_2 the maximum micro-slip turns to occupy the trailing edge, as shown in Figures A.7(c)-(f). Except for t_1 , the maximum value of micro-slip in the elastic solution is always higher than that in the elasto-plastic solution. The results indicate that plastic deformation effectively suppresses the micro-slip.

The direction of micro-slip should theoretically be opposite to the surface shear traction. Comparing Figure A.7 with A.6, this is generally the case except for t_2 . As shown in Figure A.7(b), a few micro-slip vectors at t_2 are not towards the trail edge of the contact patch. The errors in the micro-slip vectors decrease gradually after t_2 . The decrease is caused by: 1) the transition from shift to stationary rolling. The tangential loads change from increasing to decreasing at the start of the transition at t_2 (see Figure A.3(b)), so there are more disturbances. Such disturbances gradually decrease once the upper bodies starts rolling, and 2) the increase in the magnitude of micro-slip. With larger magnitudes of the longitudinal components of micro-slip, the small errors become less visible.

A.3 VALIDATION OF THE FE MODEL

In this section, the elastic solution of the FE model is verified with classical half-space based contact models, i.e., Hertz theory for the frictionless normal solution, and Spence solution for frictional compression, Cattaneo solution for tangential shift and Kalker's computer program CONTACT for frictional rolling.

A.3.1 SPENCE COMPRESSION

A semi-analytical solution of axisymmetric frictional compression with partial slip was first presented by Spence [1, 2]. He showed that for two dissimilar elastic bodies, a slip region in the form of an annulus would initiate from the edge of the contact patch under a monotonically increasing normal force. The eigenvalue c_a , defined as $c_a=c/a$, where c is the radius of the adhesion region and a is the radius of the contact patch, is governed by three parameters, namely the friction coefficient, Young's modulus and Poisson's ratio. According to Spence's method, c_a is obtained from:

$$\mu = \frac{\gamma}{2c_a \kappa \left(\sqrt{1 - c_a^2} \right)} \ln \frac{1 + c_a}{1 - c_a} \quad (\text{A.1})$$

where κ is the complete elliptic integral of first kind and γ is the Dundurs parameter, given by:

$$\gamma = \left(\frac{1 - 2\nu_1}{2G_1} - \frac{1 - 2\nu_2}{2G_2} \right) \Bigg/ \left(\frac{1 - \nu_1}{G_1} - \frac{1 - \nu_2}{G_2} \right) \quad (\text{A.2})$$

where G_1 and G_2 are the shear modulus of the upper and lower bodies, respectively.

The value of surface shear traction in the annular region $c < r \leq a$ is calculated from the Hertz pressure multiplied by the friction coefficient, while in the circular region $r \leq c$ the value is calculated by equations (6) to (9) in [21].

The process of Spence compression is calculated numerically using CONTACT and the FE model with the same mesh size. To make the slip region clearly observable, the Young's modulus of the lower body E_2 is set to 10 GPa, 1/21 of E_1 (Young's modulus of the upper body). The maximum normal load F_N is set to 20 kN. Figure A.8(a) shows the stress distribution along the longitudinal axis ($y = 0$) when $\mu = 0.25$. Here, the value of μ is set to 0.25 instead of 0.5 because when $\mu = 0.5$ over 99% of the contact patch is occupied by adhesion and it is hard to identify the slip region. Table A.2 summarizes the maximum stress and the radius of the contact patch as well as their relative errors.

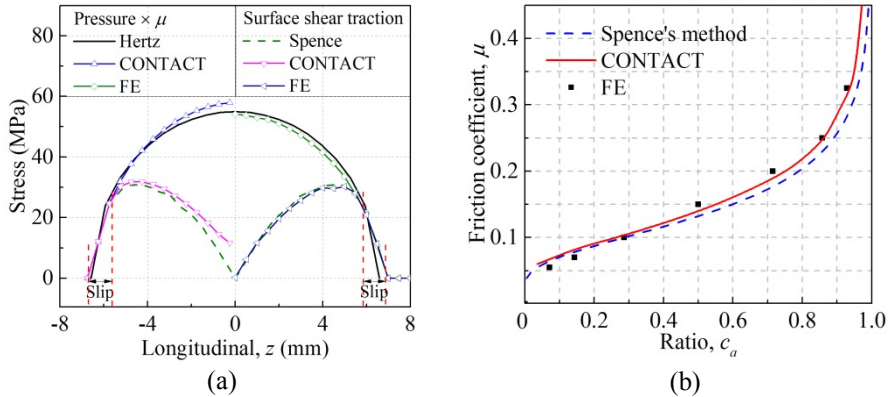


Figure A.8: Comparison of results for Spence compression. (a) Stress distributions along the axis ($y=0$) when $\mu=0.25$, (2) the relation between μ and c_a .

Table A.2: Comparison of solutions for Spence compression

Approach	Patch radius (mm)	Pressure (MPa)	Shear traction (MPa)
Hertz/Spence	6.59	219.99	30.78
CONTACT	6.25	231.72	31.81
FE	6.50	216.64	30.22
Diff. FE w.r.t Hertz/Spence	-1.4%	-1.5%	-1.8%
Diff. FE w.r.t CONTACT	3.8%	-6.9%	-5.2%

As can be seen, the radii of the contact patch obtained from the three approaches show a good agreement. The FE solution is 1.4% smaller than the Hertz solution and 3.8% larger than the CONTACT solution. The difference mainly comes from the discretization of contact bodies, because in the two numerical approaches the radius of the contact patch can only be a multiple of the element length. Due to the equal radii of the contact bodies, the contact patch is in the shape of circle during compression, and the diameter of the contact patch is equal to the length of 25 elements in the CONTACT solution and 26 elements in the FE solution. Comparing the FE solution with Spence's semi-analytical solution, the maximum pressure decreases by 1.5% and the maximum surface shear traction decreases by 1.8%. The differences are very small compared with the differences between the FE solution and CONTACT solution, as the maximum pressure and surface shear traction from the FE model are 6.9% and 5.2% lower than those from CONTACT. Theoretically, the value of surface shear traction at the centre of the contact patch should be zero, yet a non-zero result is obtained from CONTACT (see Figure A.8(a)). This is caused by the mesh.

Figure A.8(b) illustrates the relation between μ and c_a when μ varies from 0 to 0.45. The overall trends of the three solutions are in good agreement. The Spence solution is slightly below the trend. The FE solution is slightly smaller than the others when μ is below 0.1 while becomes slightly larger when μ is over 0.1. The difference is mainly caused by the mesh size. It can be up to 3.8% in an extreme case, which is a half of the element length divided by the radius of the contact patch. Once μ exceeds 0.325, the adhesion region would occupy over 92.3% of the whole contact patch, and no physical results can further be obtained from the FE model unless a smaller mesh size is adopted.

A.3.2 COMPRESSION TO CATTANEO SHIFT

For two elastically and geometrically similar bodies, the contact patch will be occupied by a sole adhesion region, if, and only if, a normal load is applied (see Figure A.4(a)) because of the identical displacement fields on the local contact areas. When a monotonically increasing tangential load is exerted on normally compressed bodies, shear traction, parallel to the contact patch, will occur. A slip region in the shape of an annulus will initiate and then grow from the edge of the contact patch (Figure A.4(b)). According to Johnson [6], the problem was first investigated by Cattaneo.

In Cattaneo's method, the value of surface shear traction in the annular region $c < r \leq a$ (where r is the distance to the centre of contact patch) is expressed in [22] as

$$\tau_1(r) = \frac{3\mu F_N}{2\pi a^2} \left[1 - \left(\frac{r}{a} \right)^2 \right]^{1/2} \quad (\text{A.3})$$

while in the circular region $r \leq c$, surface shear traction is given by the superposition of equations (A.3) and (A.4):

$$\tau_2(r) = -\frac{c}{a} \frac{3\mu F_N}{2\pi a^2} \left[1 - \left(\frac{r}{c} \right)^2 \right]^{1/2} \quad (\text{A.4})$$

To keep equilibrium of the forces in the FE model, two tangential forces F_{T1} and F_{T2} are exerted as shown in Figure A.3(a). The normalized radius of the adhesion region is then given by:

$$c_a = \left(1 - \frac{\xi}{\mu} \right)^{1/3} \quad (\text{A.5})$$

The process of shift is determined using Cattaneo's analytical method, CONTACT and the FE model. Figure A.9(a) shows the stress distribution along the longitudinal axis ($y=0$) when $\xi = 0.35$, and Table A.3 summarizes the maximum stress and radius of the contact patch. Generally, results in Figure A.9(a) show a good approximation. Among all the approaches, the FE model calculates the largest radius of the contact patch and the smallest peaks of pressure and surface shear traction. Yet, the maximum difference is small, where it is 4.9% in terms of the maximum shear traction between the FE solution and the analytical solution.

Table A.3: Comparison of solutions for Cattaneo shift

Approach	Patch radius (mm)	Pressure (GPa)	Shear traction (GPa)
Hertz/Cattaneo	6.38	2.34	0.85
CONTACT	6.25	2.33	0.84
FE	6.50	2.27	0.81
Diff. FE w.r.t Hertz/Cattaneo	1.8%	-3.1%	-4.9%
Diff. FE w.r.t CONTACT	3.8%	-2.6%	-3.7%

Figure A.9(b) gives the relation between ξ and c_a when ξ varies from 0 to 0.5. Although a slight fluctuation is observed in the FE solution, all the three results are still in good agreement.

The maximum difference between the FE solution and others is 2.7% when $\xi=0.23$. This is mainly due to the mesh.

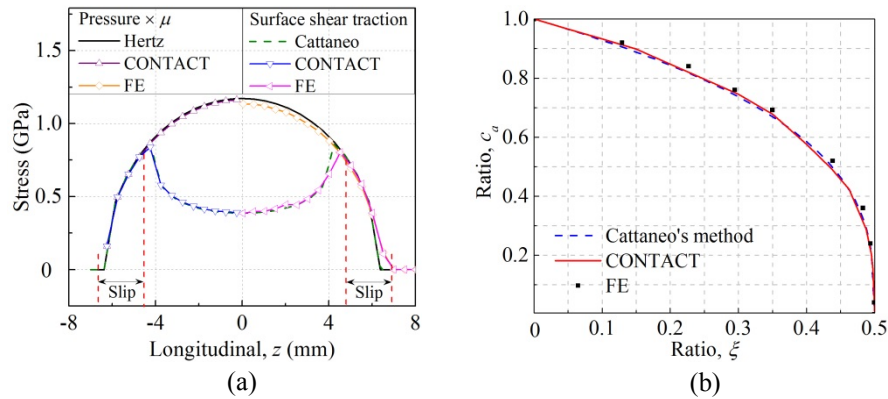


Figure A.9: Comparison of results for Cattaneo shift. (a) Stress distributions along the axis ($y = 0$) when $\xi = 0.35$, (2) the relation between ξ and c_a .

A.3.3 CATTANEO SHIFT TO STATIONARY ROLLING

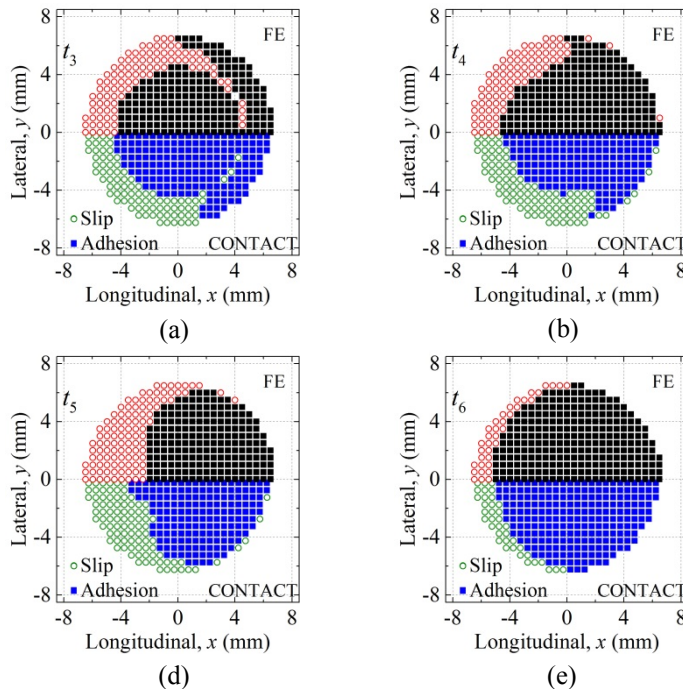


Figure A.10: Comparison of adhesion-slip region distributions between FE and CONTACT. The top half is from the FE model, the bottom half from CONTACT.

The transition from shift to stationary rolling in Section A.2, i.e., the evolution of frictional contact from t_2 to t_6 , is simulated by CONTACT. Figure A.10 compares the adhesion-slip regions, in which the results between the two solutions show a good approximation. The differences between the two solutions are 1) the size of the adhesion region versus the whole contact patch, the difference is 7.8% at t_4 and is maximum of 2.4% for all other instants, and 2) the shape of the adhesion regions, which can be easily observed in Figures A.10(b)-(c).

As for the stress distributions along the axis ($y=0$), good agreement is obtained between the two methods (see Figure A.11). The main differences are 1) the slightly higher values of the maximum pressure from CONTACT at all selected instants, and 2) the small fluctuations of surface shear traction for the FE solution, as shown in Figure A.11(d).

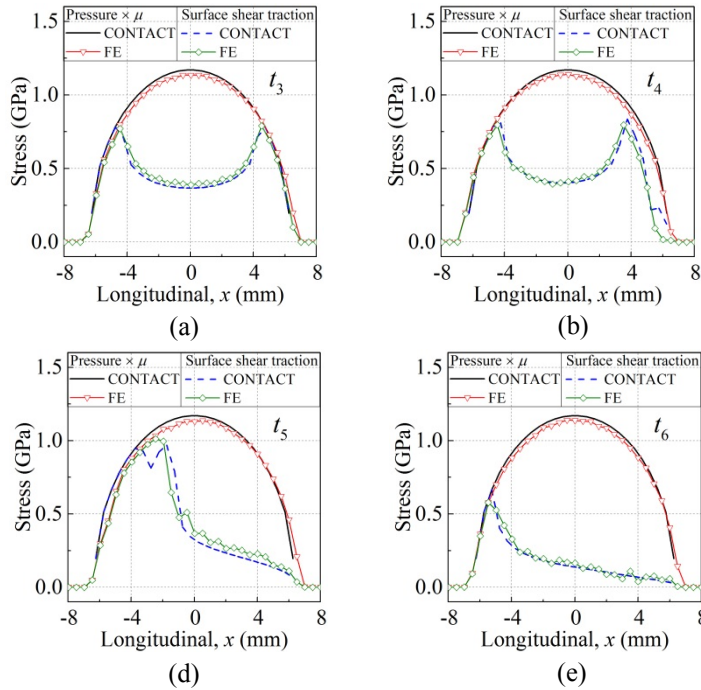


Figure A.11: Comparison of stress distributions along the axis ($y=0$) between FE and CONTACT.

The differences between the two methods observed in Figures A.10 and A.11 could come from the modelling of the instationary rolling. As shown in Figure A.3(b), the acceleration of the upper body changes significantly during the transition from the shift to stationary rolling, so the influence of inertia on the evolution of the adhesion-slip regions cannot be overlooked. Such inertia effect is physically accounted for in the FE modelling yet is neglected in CONTACT. Besides, the differences could also come from the deviation in the actual instants for the two solutions. Nominally the comparison is made for the same time instants t_3 , t_4 , t_5 and t_6 (see Figure A.3(b)). In CONTACT it is, however, difficult for the calculation to be timed precisely for these instants, because in CONTACT the rolling distance traversed per time step has to be comparable with the mesh size, otherwise divergence may occur.

A.4 DISCUSSION

In practical applications, frictional contact between solids can be more complex, since factors such as thermal-mechanical behaviour and complicated material constitutive models may be involved. This study employs simple but typical material models to show the validity of the FE model by comparison with classical solutions and to illustrate the capacity of the model. More realistic material models, linear or nonlinear, can readily be incorporated in the FE modelling.

Classical methods such as CONTACT are based on the statics assumption. However for contact in the dynamic process the classical solutions may lose their accuracy due to the involvement of inertia effect and structure vibration. Alternatively, this inherent behaviour of solids can be taken into account with the presented FE method. The FE model is also more universal for general loading scenarios and contact geometry.

The fluctuations in the FE solution, such as those in Figures A.3(b) and A.5(f), are mainly attributed to the high frequency vibration between the contact bodies. Such vibrations are physical and inherent when dealing with dynamic problems. In the elasto-plastic case the plastic deformation absorbs energy and can thus reduce such vibration. The vibration can, however, not be totally eliminated, as long as any change in loading is present. It is shown that such high frequency vibration can cause the change of micro-slip and thus result in fretting. This means that the model has the potential for fretting study.

Generally speaking, the mesh size and the dimension of the FE model are restricted by the computational resources. Proper balance is required between accuracy and efficiency. The mesh size of this chapter appears to be reasonable for the demonstration. To achieve higher accuracy of contact solutions, smaller mesh size is required.

For the scenario of dry friction, e.g., the absence or the starvation of lubrication, the method presented is directly applicable to calculating the precise contact solution, and then frictional work and plastic deformation of contact bodies can be obtained. While with the presence of lubrication, a third body layer may have to be included between the two contacting bodies, or a velocity dependent friction coefficient needs to be accounted for [23]. Regarding damages such as cracks and fracture, the contact solution obtained from the FE model also provides an reliable input for corresponding damage prediction models [24, 25].

A.5 SUMMARY

In this chapter a finite element model is presented to study the evolution of frictional contact during the instationary interactions. The FE solution is validated thoroughly with classical half-space based methods in the process from compression to shift and then to rolling. The effect of plastic deformation on the distributions of adhesion-slip regions, pressure, surface shear traction as well as micro-slip during instationary interactions is investigated. Results indicate that with the involvement of plastic deformation the normal contact solution becomes significantly dependent on the tangential contact solution. The structure vibrations are partly damped out and the magnitude of micro-slip is effectively diminished during the instationary interactions.

In comparison to existing half-space or quasi-quarter based contact models, the FE model is capable of treating instationary rolling without the assumption of linear elasticity and statics.

Thus, the FE model is more capable of analysing the evolution of wheel-rail frictional contact during the start-off and braking of railway vehicles, in order to minimize or delayed the failures of wheel and rail components.

REFERENCES

- [1] D.A. Spence, *The Hertz contact problem with finite friction*, Journal of Elasticity **5**, 297-319 (1975).
- [2] D.A. Spence, *Similarity considerations for contact between dissimilar elastic bodies*, in *IUTAM Symposium on Mechanics of Contact* (Delft, Netherland, 1975) pp. 67-76.
- [3] R.D. Mindlin, *Compliance of elastic bodies in contact*, Journal of Applied Mechanics **16**, 259-268 (1949).
- [4] R.D. Mindlin, H. Deresiewica, *Elastic spheres in contact under varying oblique forces*, Journal of Applied Mechanics **75**, 327-344 (1953).
- [5] F.W. Carter, *On the action of a locomotive driving wheel*, Proceedings of the Royal Society of London A-Mathematical, physical and engineering sciences **112**, 151-157 (1926).
- [6] K.L. Johnson, *Contact Mechanics* (Cambridge University Press, 1985).
- [7] J.J. Kalker, *Three-dimensional elastic bodies in rolling contact* (Kluwer Academic Publishers, 1990).
- [8] R. Dollevoet, Z. Li, O. Arias-Cuevas, *A method for the prediction of head checking initiation location and orientation under operational loading conditions*, Proceedings of the institution of mechanical engineers, Part F: Journal of Rail and Rapid Transit **224**, 369-374 (2010).
- [9] B. Storåkers, D. Elaguine, *Hertz contact at finite friction and arbitrary profiles*, Journal of the Mechanics and Physics of Solids **53**, 1422-1447 (2005).
- [10] D. Elaguine, M.A. Brudieu, B. Storåkers, *Hertzian fracture at unloading*, Journal of the Mechanics and Physics of Solids **54**, 2453-2473 (2006).
- [11] A.T. Kasarekar, F. Sadeghi, S. Tseregoounis, *Fretting fatigue of rough surfaces*, Wear **264**, 719-730 (2008).
- [12] V. Brizmer, Y. Zait, Y. Kligerman, I. Etsion, *The effect of contact conditions and material properties on elastic-plastic spherical contact*, Journal of Mechanics of Materials and Structures **1**, 865-879 (2006).
- [13] U. Nackenhorst, *The ALE-formulation of bodies in rolling contact: Theoretical foundations and finite element approach*, Computer Methods in Applied Mechanics and Engineering **193**, 4299-4322 (2004).
- [14] N. Burgelman, Z. Li, R. Dollevoet, *A new rolling contact method applied to conformal contact and the train-turnout interaction*, Wear **321**, 94-105 (2014).
- [15] Z. Li, *Wheel-rail rolling contact and its application to wear simulation*, PhD dissertation, Delft University of Technology (2002).

[16] M. Ziefle, U. Nackenhorst, *Numerical techniques for rolling rubber wheels: treatment of inelastic material properties and frictional contact*, Computational Mechanics **42**, 337-356 (2008).

[17] P. Wriggers, *Computational contact mechanics* (Springer, 2006).

[18] X. Zhao, Z. Li, *The solution of frictional wheel-rail rolling contact with a 3D transient finite element model: Validation and error analysis*, Wear **271**, 444-452 (2011).

[19] X. Zhao, Z. Li, *A three-dimensional finite element solution of frictional wheel-rail rolling contact in elasto-plasticity*, Proceedings of the institution of mechanical engineers, Part F: Journal of Engineering Tribology **229**, 86-100 (2014).

[20] Z. Li, X. Zhao, C. Esveld, R. Dollevoet, M. Molodova, *An investigation into the causes of squats—Correlation analysis and numerical modelling*, Wear **265**, 1349-1355 (2008).

[21] B. Paliwal, R. Tandon, T.E. Buchheit, J.M. Rodelas, *An Assessment of the effectiveness of the Hertzian indentation technique for determining the fracture toughness of brittle materials*, Journal of the American Ceramic Society **94**, 2153-2161 (2011).

[22] V.L. Popov, *Contact mechanics and friction: physical principles and applications* (Springer, 2010).

[23] X. Zhao, Z. Li, *Three dimensional finite element solution of wheel-rail rolling contact with velocity dependent friction*, in *9th International Conference on Contact Mechanics and Wear of Rail/Wheel Systems* (Chengdu, China, 2012).

[24] L. Gallego, D. Nelia, S. Deyber, *A fast and efficient contact algorithm for fretting problems applied to fretting modes I, II and III*, Wear **268**, 208-222 (2010).

[25] A.T. Kasarekar, N.W. Bolander, F. Sadeghi, S. Tseregounis, *Modeling of fretting wear evolution in rough circular contacts in partial slip*, International Journal of Mechanical Sciences **49**, 690-703 (2007).

ACKNOWLEDGEMENT

当开始写这些文字时，在荷兰的求学生涯也即将结束。回首过去的时光，有成功的喜悦，也有失败的彷徨。我是幸运的，在这条漫长而曲折的道路上迎来了黎明的曙光。在这里，我向陪伴我的家人，教育我的老师，帮助我的同学，以及关心我的朋友，表示诚挚的谢意。

To my colleagues and friends 致我的老师、同学和朋友们

The study in TU Delft is a challenging yet amazing journey in my life. In the past years, I am so lucky to study, work, live and play together with so many nice people. As the journey is approaching the end, it is my great pleasure to take this opportunity to thank all the people for their help and encouragement.

My sincere gratitude goes foremost to my supervisor, also my promotor, Prof. Zili Li for his patient guidance, kind encouragement and solid support. Prof. Li is very busy, he still spent quite much time on my PhD research and helped me a lot in my personal life. When I felt struggling and upset, he can always help and support me in time. The influence from Prof. Li would be precious wealth in the rest of my life.

I am very grateful to my promotor Prof. Rolf Dollevoet. Prof. Dollevoet arranged so many interesting academic and social activities, so that I can gain a comprehensive insight on both my study and personal development. This experience is beyond scientific research, helping me become a better person.

In addition to my supervisors, I would like to express my great appreciation to Alfredo Núñez and Anthonie Boogaard, who played key roles in my PhD study. Alfredo, thank you very much for your continuous enthusiasm and tireless help. Alfredo spent a lot of energy on conceiving the research ideas and correcting my papers. I am also grateful for Alfredo's prompt response, efficient work and constructive suggestions. Anthonie is always ready to give me the help when I am in difficult situations. It is unforgettable moment that we stayed together for fruitful discussions, field measurements and coffee break. It is my honour to work together with you.

I am grateful to China Scholarship Council for its financial support. I thank my former supervisor Prof. Shunhua Zhou for encouraging me to continue my study abroad. I thank all the help and assistance from Franca Post when I just arrived in Delft.

Many thanks to Jacqueline Barnhoorn, whose daily help makes my life in Delft easier and happier. Many thanks to a lot of friends and colleagues in my section. They are Nico Burgelman, Shaoguang Li, Maider Oregui, Zhen Yang, Yuwei Ma, Maria Molodova, Xiangming Liu, Jingang Wang, Haoyu Wang, Dongya Ren, Zhiwei Qian, Chang Wan,

Xiangyun Deng, Ling Chang, Siamak Hajizadeh, Lizuo Xin, Chen Shen, Jan Willem, Jurjen Hendriks, Jan Moraal, Meysam Naeimi, Hongrui Wang, Pan Zhang, Ali Jamshidi, Yunlong Guo and Omid Hajizad. It is wonderful experience to meet and work with you. I would like to thank Greg Lambert, Ruud van Bezooijen and Ivan Shevtsov for their cooperation on field experiments.

My gratitude also goes to the Chinese visiting scholars, Yu Zhou, Rong Chen, Hongqin Liang, Pingrui Zhao, Xiubo Liu, Xianmai Chen, Li Wang, Song Liu, Lei Xu and Wenqiang Liu for your help and assistance. I am so lucky that I have a lot of friends here, Tao Lu, Yang Qu, Mingjuan Zhao, Kai Li, Shulan Shu, Kai Zhang, Li Zhu, Xiaowei Ouyang, Cui Wei, Lin Xiao, Leilei Miao, Cancan Sun, Donja Valkhoff, Edwin den Besten, Gerben Valkhoff, Bjarne den Besten, Ye Zhang, Guangming Chen, Wuyuan Zhang, Jia Xu, Jun Wu, Yueling Liu, Changgong Zhang, Qi Wang, Wenjuan Lyu and Hong Zhang. You have made my life colourful and interesting. I would like to keep you all in my memory. I also thank my former house-mates Tao Zou, Yu Sun, Xiaoyan Wei, Jialun Liu, Likun Ma and Lin Liu. It is sweet time that we live together and play together.

致我的家人 To my family

在过往的求学岁月，我的妻子周琰一直默默地陪伴在我身边。感谢你与我一起分享阳光，分担风雨，使我的学习、生活没有了后顾之忧！感谢我的父母和岳父母，你们的支持和理解让我有勇气追逐自己的梦想，让我充满了前进的动力！

CURRICULUM VITÆ

Zilong Wei

05-03-1988 Born in Laiwu, Shandong, China

EDUCATION

1999-2006	Secondary School Chenyi Middle School, Laiwu, China (1999-2003) Shandong Laiwu No.1 High School, Laiwu, China (2003-2006)
2006-2010	B.Sc. Communications and Transportation China University of Mining and Technology, Xuzhou, China
2010-2012	M.Sc. Highway and Railway Engineering Tongji University, Shanghai, China
2012-2018	Ph.D. Railway Engineering Delft University of Technology, Delft, Netherlands

LIST OF PUBLICATIONS

1. Z. Wei, A. Boogaard, A. Núñez, Z. Li, and R. Dollevoet. *An integrated approach for characterizing the dynamic behavior of the wheel-rail interaction at crossings*. IEEE Transactions on Instrumentation and Measurement, to be published. DOI: 10.1109/TIM.2018.2816800
2. Z. Wei, A. Núñez, A. Boogaard, R. Dollevoet and Z. Li. *Method for evaluating the performance of railway crossing rails after long-term service*. Tribology International **123** (2018): 337-348.
3. Z. Wei, A. Núñez, Z. Li and R. Dollevoet. *Evaluating degradation at railway crossings using axle box acceleration measurements*. Sensors **17** (2017): 2236.
4. Z. Wei, C. Shen, Z. Li and R. Dollevoet. *Wheel-rail impact at crossings: relating dynamic frictional contact to degradation*. Journal of Computational and Nonlinear Dynamics **12** (2017): 041016.
5. Z. Wei, Z. Li Z. Qian, R. Chen and R. Dollevoet. *3D FE modelling and validation of frictional contact with partial slip in compression-shift-rolling evolution*. International Journal of Rail Transportation **4** (2016): 20-36.